ABSTRACT

We observed the effect of radiation pressure on the angular sensing and
control system of the Laser Interferometer Gravitational-Wave Observa-
tory (LIGO) interferometer's core optics at LIGO Hanford Observatory.
This is the first measurement of this effect in a complete gravitational
wave interferometer. Only one of the two angular modes survives with
feedback control, since the other mode is suppressed when the control
gain is sufficiently large. We developed a mathematical model to under-
stand the physics of the system. The model indicates that the current
system has substantial margin for higher laser power; angular instabil-
ity due to radiation pressure won't occur until laser power reaches about
eight times the power used in the initial LIGO configuration. This analy-
sis was based on the degrees of freedom associated with differential motion
between the mirrors in the interferometer's two arms. A more complete
analysis including the common mode degrees of freedom will be left for
future work.

A study of angular instability due to radiation pressure in LIGO gravitational wave detector

by

Eiichi Hirose

DISSERTATION

Submitted in partial fulfillment of the requirements for the

degree of Doctor of Philosophy in Physics

in the Graduate School of Syracuse University

Syracuse University

Syracuse, New York

December 2008

Approved ⎯⎯⎯⎯⎯⎯⎯⎯⎯⎯⎯⎯

Prof. Peter R. Saulson

Date ⎯⎯⎯⎯⎯⎯⎯⎯⎯⎯⎯⎯

Committee Approval Page

Contents

List of Figures

List of Tables

ACKNOWLEDGMENTS

Adhikari initiated the angular instability project which was the start of this thesis, and helped me continuously. Finally, I would like to thank friends here in Syracuse. Eric West, Mike Defeo, Dave Quint, Michele Fontanini, Luca Giome, Creighton Thomas, and Alphonso Magri. I have a lot of fine memories with these guys. They kept me sane with the good times we had (mostly beer and stupid jokes). I appreciate their attitude and honesty toward me.

Chapter 1

Introduction

1.1 LIGO gravitational wave detectors

There are three LIGO (Laser Interferometer Gravitational-Wave Observatory) detectors in the United States: a 4km interferometer in Livingston Parish, LA (L1), and two interferometers whose length are 4km (H1) and 2km (H2) near Hanford, WA. Each LIGO detector is a Michelson interferometer with a pair of Fabry-Perot cavities and a recycling cavity.
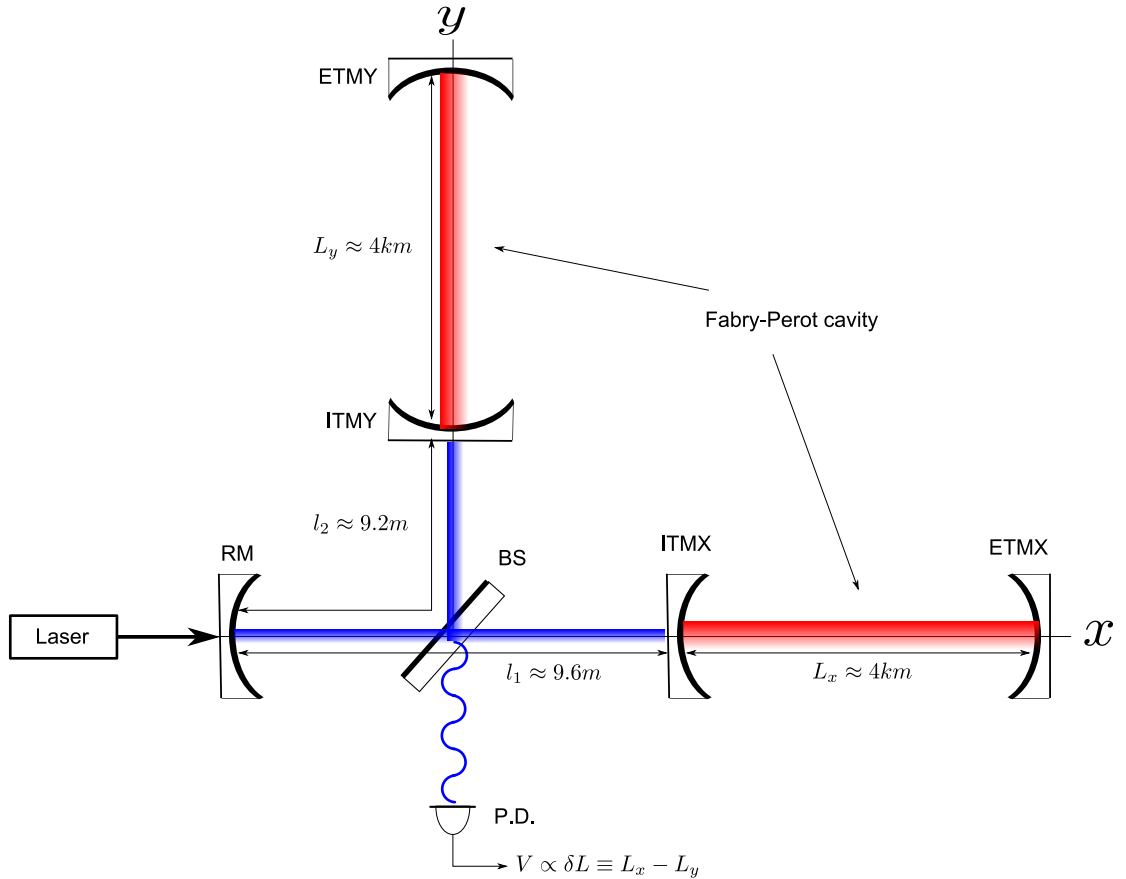
Figure 1.1: A Schematic of LIGO detector. There are two Fabry-Perot cavities (red) whose arm length is about 4 km, and a recycling cavity (blue) to recycle reflected light from the arms. Test masses (their conventional names are listed in the sketch) are hung by wire from a suspension system and the interferometer is put in a vacuum envelope. The detector is tuned to make dark fringes at the anti-symmetric port where photodetectors (P.D.) sense phase changes from the destructive pattern caused by differential arm length change.

It has been built to detect gravitational waves from space although the detection

has not been successful yet as of December 2008. The fifth science run (S5) finished in the fall 2007 and the two 4 km long detectors are being upgraded at this moment for an upcoming science run - roughly a factor of two better in sensitivity than S5. Meanwhile the 2 km long detector has been running so as not to miss chances for possible detection. Besides LIGO, worldwide efforts have been going on such as VIRGO (French/Italian), GEO (English/German), and TAMA (Japanese) etc, and they are actively collabolating to the same goal. Strain sensitivity reached order of $\frac{\Delta L}{L} \sim 10^{-21}$ during S5 [9, 10]. Figure 1.2 shows the sensitivity curve of LIGO Hanford Observatory during the S5 run.
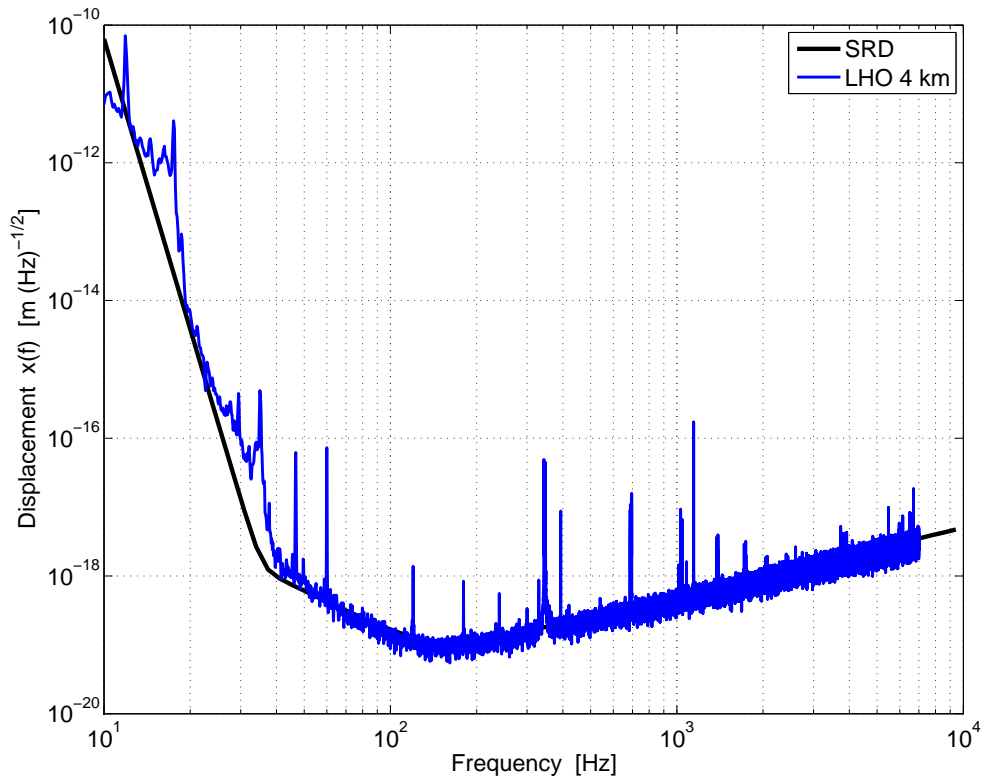
Figure 1.2: Sensitivity curve of LIGO Hanford 4-km detector from May 2007, which is the spectra of calibrated signal of gravitational wave channel. SRD is the design sensitivity. Best sensitivity is near 100 Hz. y-axis is displacement in $m/\sqrt{Hz}$ which comes from a fact that the displacement is measured as power spectrum on photodetectors at the antisymmetric port.

Gravitational waves are wave solutions of Einstein's field equations and they were predicted a couple of years after his theory General Relativity was published in 1915. General relativity is a mathematical model of *spacetime* where gravity is the curvature of spacetime. In the theory, spacetime is completely described by a metric on a spacetime manifold [1, 2, 3, 4, 5]. Although the theory successfully passed several tests in the past, its validity in the strong field limit has not been well tested [12, 13, 14].
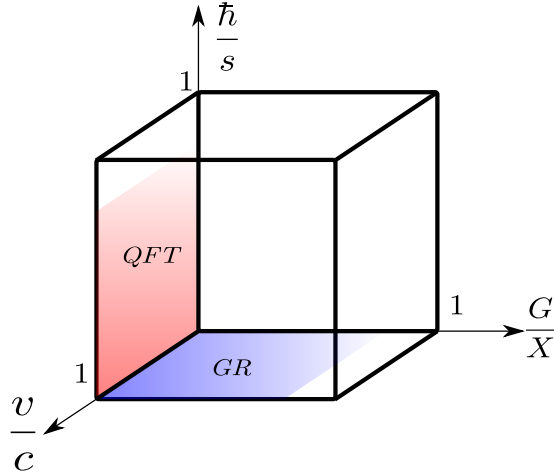
Figure 1.3: General relativity in a parameter space.

In 1899, Max Planck, using gravitational constant G, Planck constant $\hbar$, and speed of light c, constructed fundamental units $l_p = \sqrt{\frac{\hbar G}{c^3}} \approx 1.62 \times 10^{-35}m$, $t_p = \sqrt{\frac{\hbar G}{c^5}} \approx 5.4 \times 10^{-44}s$, and $m_p = \sqrt{\frac{\hbar c}{G}} \approx 2 \times 10^{-8}kg \approx 1.2 \times 10^{-19}GeV$. Suppose a system is characterized by length l, time t, and mass m, and we construct some quantities such as velocity $v = \frac{l}{t}$, action $s = \frac{ml^2}{t}$, and $X = \frac{l^3}{mt^2}$ [57]. Then, we can view physics we know in a cube characterized by three axes $(G/X, v/c, \hbar/S)$. We know general relativity works well on the $(G/X, v/c)$ plane away from the region close to the very end of G/X axis where gravity is very strong (i.e., $G \sim X$). Likewise, the $(v/c, \hbar/s)$ plane is mostly covered by quantum field theory (QFT) except in the region close to the very end of the $\hbar/s$ axis. We do not yet (and may never) know a valid theory to

describe physics in the other region of the cube.

In 1974, Hulse and Taylor discovered that the orbital period of PSR B1913+16 changes at a rate predicted by general relativity, due to its emission of gravitational waves. Since then, the direct detection of gravitational waves has been desired, especially so that we can explore the physics.

In the LIGO detectors, the light from the Fabry-Perot cavities are tuned to make destructive interference at a beamsplitter such that a photodetector at the anti-symmetric port does not get any light without any disturbances. Once a gravitational wave arrives with detectable amplitude, it will disturb the destructive interference, and the photodetector at the dark port senses a power change. The dark port condition minimizes some technical noise and allows the concept of "recycling". Since the most laser light power go back to the upstream (the input laser direction), by placing another high reflective mirror called recycling mirror, the light power in the Fabry-Perot cavities can be increased. The more power in the cavity makes the shot noise in the sensitivity curve smaller by a factor of the inverse square root of the power. Each test mass is suspended by wires from a seismic isolation system to realize nearly free fall motion and minimize local seismic disturbances. Arm cavities are put in vacuum to minimize thermal noise and noise from index of refraction fluctuations. A pre-stabilized solid state Nd:YAG laser, whose wavelength is 1064 nm, is injected and it bounces back and forth in the Fabry-Perot cavities roughly 100 times to enhance sensitivity of the detector. In order to hold high power in the cavities, fused silica (SiO2) is used and the surface is polished and coated for more uniformity and less losses. There are a lot of control loops to keep the operating condition: two cavities and recycling cavity on resonance, dark fringe at antisymmetric port, stabilization of the laser frequency, and alignment of mirrors to the laser beam etc. Specification of the detector is summarized in table 1.1.

There are four length degrees of freedom (DOF) in the LIGO defined by the five

Laser / wavelength / input power	Nd:YAG / 1064 nm / 10W
Core optics	Suspended
Suspension	Seismic isolation stack
Input test masses: ITM's	
Power reflectivity	96.995 %
Power transmission	3.00 %
Radius of curvature	14571 m
Diameter/thickness	0.25 m / 0.10 m
Index of refraction	1.44968
End test masses: ETM's	
Power reflectivity	99.9935 %
Power transmission	0.0015 %
Radius of curvature	7400 m
Diameter/thickness	0.25 m / 0.10 m
Recycling mirror: RM	
Power reflectivity	97.5 %
Power transmission	2.44 %
Radius of curvature	99998.33 m
Diameter/thickness	0.25 m /0.10 m
Beam splitter: BS	
Power reflectivity	49.9625 %
Power transmission	49.9625 %
Radius of curvature	∞
Diameter/thickness	0.25 m / 0.04 m
Arm cavity length	4 km
Recycling cavity length	9.38 m
Michelson asymmetry	0.210 m
Resonant sideband frequency	23.97 MHz
Non-resonant sideband frequency	35.96 MHz

Table 1.1: Initial LIGO's specification copied from [34].

core optics (See figure 1.1. ITMX, ETMX, ITMY, ETMY, RM). The DOFs are two Fabry-Perot arm cavity lengths L_1, L_2 and two Michelson lengths l_1,l_2. In order to achieve the design sensitivity, these lengths must be controlled within order of 10^{-13} m. Besides that, each mirror has two orientation degrees of freedom pitch and yaw[1], so it makes total angular degrees of freedom 10. The LIGO detectors control the angular orientation by a feedback control system called ASC (angular sensing and

---

[1]The pitch angle is defined as the orientation to the x-y plane, while the yaw angle is defined by rotation on the x-y plane.

control) system within 10^{-8} radian rms about the optical axis and the laser beam is centered on the mirrors within 1 mm [34] to satisfy the design sensitivity. In order for the ASC system to have high gain but not to spoil the sensitivity, the coupling between angle and length has been reduced to order of 10^{-4} m rad^{-1} [9].

1.2 Overview of this work

This thesis mainly consists of two parts. The first part is about calibration of the detector, which is written in chapter 2. The second part is about angular instability, which is written in chapter 4. Chapter 3 is devoted to preparation for chapter 4, explaining the concept of angular sensing and control.

All contents in chapter 2 are from V3 calibration runs for S5. We briefly describe response of a Fabry-Perot cavity and a full interferometer; each turns out to be a simple cavity pole function up to some frequency where some corrections are needed. In addition, the response of the detector is also affected by the pendulum suspension of the test masses. Filter banks and electronics in various control loops will also modify the response. The response of gravitational wave detector is the result of the complicated system, and calibration is the job to find the relation between the output from the detector and displacement ΔL(or strain $\frac{\Delta L}{L}$). The calibration takes place in the frequency domain. For various reasons (from data analysys for searches of gravitational waves to false signal hunting, etc), time series of gravitational wave strain $h(t)$ is often preferred. The process to make the time series is called $h(t)$ generation. Instead of doing the inverse-Fourier transform of the frequency domain strain data, we make use of digital filters to generate the $h(t)$ directly from output of gravitational wave channel.

The chapter 4 is about angular instability. Roughly above 100 Hz, the detector's performance is limited by shot noise. It is known that shot noise is inversely proportional to the square root of laser power. This is why future detectors are geared more toward higher power operation. The need for high sensitivity of the detector will make radiation pressure from the laser beam noticeable. Not only the longitudinal effect from the radiation pressure, but also the mirrors will experience torque when the beam spot is off center. Once the torque exceeds the sum of restoring torque from the wire and actuators attached to the surface of the mirror, the mirrors cannot

be controlled any more. D. Sigg and J. Sidles studied the phonomena theoretically and predicted two different modes in a tilted optical resonator system. Recently we experimentally confirmed for the very first time that the phenomenon exists in the LIGO detector. We also developed a mathematical model to understand the physics. According to the model, the LIGO detector will be stable until the cavity laser power reaches about eight times higher than that of iLIGO if the same ASC system is employed. Although the model treats only one arm, we believe that the method will be very useful for the future detector design, and that the model can be extended to more complete interferometer models.

Chapter 2

Interferometric Gravitational Wave Detectors

2.1 Response of detector

2.1.1 Phase shift caused by a gravitational wave

It is known that there are two independent polarizations in gravitational waves, $+$ and $\times$ (see Appendix A). Although it is unlikely, suppose a $+$ polarized gravitational wave arrives perpendicular to our detector and the transverse components are perfectly along two arm cavities of our detector. (Discussion for more general case can be found, for example, in [24, 25].)
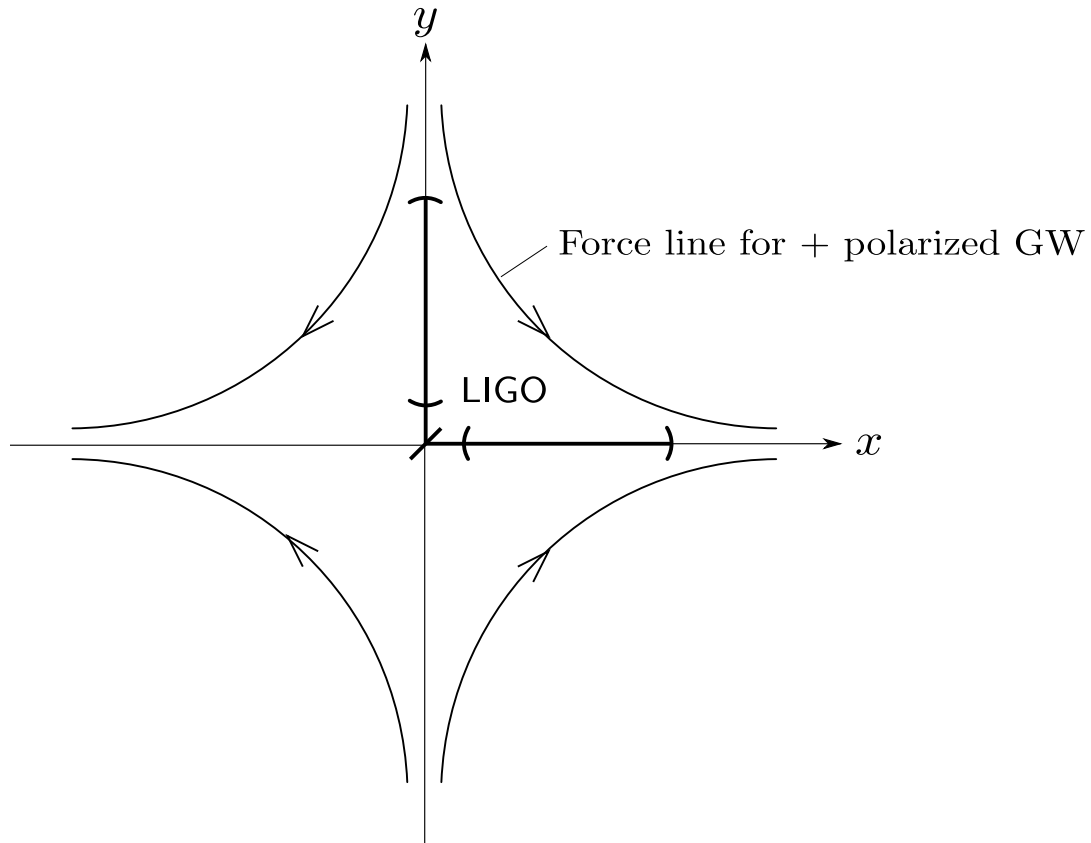
Figure 2.1: $+$ polarized GW and LIGO. An ideal situation that a $+$ polarized gravitational wave passes through the LIGO detector. Here, we assume the gravitational wave propagates along the z-axis (perpendicular to the paper), and the transverse directions are along LIGO's two arms.

Proper distance is given by

$$dτ^2 = g_{μν}dx^μdx^ν, \tag{2.1.1}$$

where $g_{μν}$ is the Minkowski metric plus small perturbation, i.e., $g_{μν} = η_{μν} + h_{μν}$. In the TT gauge, it will be given by as follows.

$$g_{μν} = \begin{pmatrix} -1 & 0 & 0 & 0 \\ 0 & 1+h & 0 & 0 \\ 0 & 0 & 1-h & 0 \\ 0 & 0 & 0 & 1 \end{pmatrix} \tag{2.1.2}$$

with

$$h = h_{xx}e^{-i(Ωt-kz)}, \tag{2.1.3}$$

where $Ω$, k are the angular frequency and the wave number of the gravitational wave, respectively. We assume that $h_{xx} ≪ 1$. Now, we calculate a phase shift of a light whose angular frequency is $ω$ when the light takes one round trip in the Fabry-Perot cavity in the x-arm.

$$Φ_{rt}^x(t_0) = \int_{t_0}^{t_0+t(2L)} ωdt \tag{2.1.4}$$

Since $dτ = 0$ for light, the integration can be performed as follows.

$$\begin{aligned} Φ_{rt}^x(t_0) &= \frac{ω}{c}\int_0^L dx\left\{\sqrt{1+h_{xx}e^{-i(Ωt_0+kx)}} + \sqrt{1+h_{xx}e^{-i(Ωt_0+k(2L-x))}}\right\} &(2.1.5) \\ &≈ 2\frac{ωL}{c} + \frac{ωLh_{xx}}{c}\frac{sinΦ_Ω}{Φ_Ω}e^{-i(ωt_0+Φ_Ω)} &(2.1.6) \end{aligned}$$

where $Φ_Ω = kL = \frac{ΩL}{c}$. The last line tells us that the light gets extra phase shift in

the presence of gravitational wave, i.e.,

$$\Delta\Phi_{rt}^x = \frac{\omega L h_{xx}}{c}\frac{sin\Phi_\Omega}{\Phi_\Omega}e^{-i\Phi_\Omega} \tag{2.1.7}$$

Assuming the frequency of the gravitational wave is not so high, i.e., $\Phi_\Omega \ll 1$,

$$\Delta\Phi_{rt}^x = \frac{\omega h_{xx}L}{c} = \frac{\omega\Delta L}{c}, \tag{2.1.8}$$

where $\Delta L = h_{xx}L$. We can express the phase shift during light propagation in one round trip in terms of the small arm length change $h_{xx}L$. Therefore,

$$\Delta\Phi_{rt} = \frac{2\pi}{\lambda}\Delta L \tag{2.1.9}$$

We can calculate Φ_{rt}^y in the same way, and it will be

$$\Delta\Phi_{rt}^y = \frac{\omega h_{yy}L}{c} = -\frac{\omega h_{xx}L}{c} = -\frac{\omega\Delta L}{c} \tag{2.1.10}$$

Assuming $L_x \approx L_y \approx L$, therefore, the phase difference between two arms for one round trip will be

$$\Delta\Phi_d \equiv \Delta\Phi_{rt}^x - \Delta\Phi_{rt}^y = \frac{4\pi}{\lambda}\Delta L. \tag{2.1.11}$$

The phase difference will go up if light bounces back and forth between two mirrors, as it does in a Fabry-Perot cavity. It is known the rate of increase is characterized by the *finesse* $\mathcal{F}$.

$$N = \frac{2\mathcal{F}}{\pi} \qquad (2.1.12)$$

The finesse is defined using reflectivity coefficients of the resonator as follows.

$$\mathcal{F} = \frac{\pi\sqrt{r_1 r_2}}{1 - r_1 r_2}. \qquad (2.1.13)$$

Therefore, within the Fabry-Perot cavity, the overall phase difference between two arms is given by

$$\Phi_d^{FP} = N\Delta\Phi_d = \frac{8\mathcal{F}}{\lambda}\Delta L. \qquad (2.1.14)$$

As discussed later, high finesse is an advantage in detecting gravitational waves since the phase difference is proportional to arm length difference. [1]

2.1.2 Pound-Drever-Hall technique

The purpose of this subsection is to introduce the powerful Pound-Drever-Hall technique [66]. In the previous sebsection, we learned gravitational waves make a phase shift in a Fabry-Perot cavity. Here, we will learn how to extract the information using a technique called the Pound-Drever-Hall technique. An extension of this technique is also used in alignment sensing, which will be discribed in chapter 3.

---

[1]In reality, gravitational waves also produce phase shift in Michelson arms l_1 and l_2 (See figure 1.1), i.e.,

$$\delta L_{meas} = \left(1 + \frac{2l}{\mathcal{F}L}\right)\delta L_{GW}, \qquad (2.1.15)$$

where δL_{meas} is measured length difference and δL_{GW} is arm length difference caused by gravitational waves. Since the seceond term is order of $\sim 10^{-5}$ in LIGO, we can ignore the coupling from Michelson arm length.

For locking a cavity on resonance, we calculate the reflected light from a Fabry-Perot cavity. The cavity has two mirrors separated by distance L (input mirror an end mirror), whose reflection and transmission coefficients are r_1, t_1 and r_2, t_2 respectively. The electric field E_{circ} circulating inside the cavity can be expressed in terms of the incident field E_{in} as

$$E_{circ} = t_1 E_{in} + P_{rt} E_{circ}. \tag{2.1.16}$$

P_{rt} is round trip operator in the cavity, is simply the phase shift due to propagation between the mirrors and amplitude change by reflection. Namely,

$$P_{rt} = (-r_1)e^{-ikL}(-r_2)e^{-ikL} \tag{2.1.17}$$

$$= r_1 r_2 e^{-2ikL}. \tag{2.1.18}$$
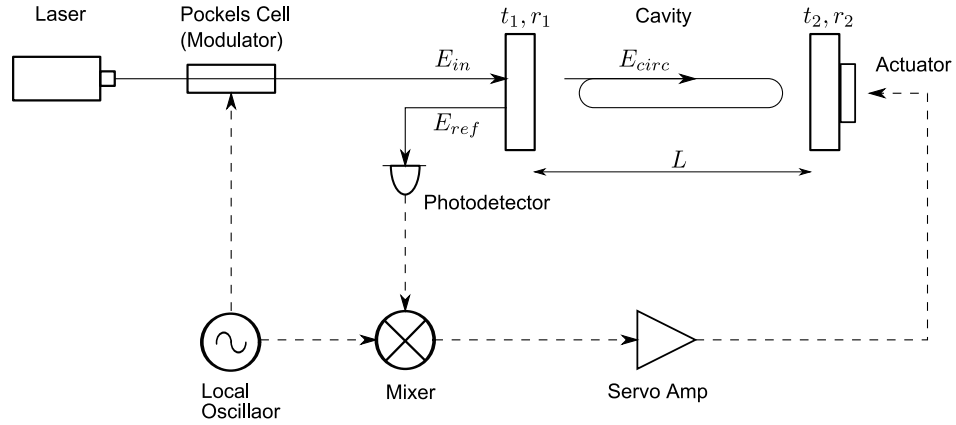
Figure 2.2: A layout to lock a cavity to a laser. Light that has been phase modulated by a Pockels Cell goes into a cavity. Demodulating the reflected light at mixer yields an error signal that can tell you which way to push the actuator to hold the cavity on resonance with the laser's wavelength.

Therefore, the electric field inside the cavity is given by

$$E_{circ} \quad = \quad t_1(1 - P_{rt})^{-1}E_{in} \tag{2.1.19}$$

$$= \quad \frac{t_1}{1 - r_1 r_2 e^{-2ikL}}E_{in}. \tag{2.1.20}$$

The electric field reflected from the cavity is

$$E_{ref} \quad = \quad r_1 E_{in} + t_1 P_{rt} r_2 P_{rt} E_{circ} \tag{2.1.21}$$

$$= \quad r_1 - \frac{r_2 t_1^2 e^{-2ikL}}{1 - r_1 r_2 e^{-2ikL}} \tag{2.1.22}$$

$$= \quad \frac{r_1 - r_2(r_1^2 + r_2^2)e^{-2ikL}}{1 - r_1 r_2 e^{-2ikL}}. \tag{2.1.23}$$

The resonant condition is simply the condition in which the electric field inside the cavity becomes maximum.

$$e^{-2ikL} = 1 \iff kL = n\pi \iff L \quad = \quad n\frac{\lambda}{2} \tag{2.1.24}$$

Here, λ is the wavelength of laser, and n is an integer.

Next, prepare a phase modulated electric field.

$$E_{in} = E_0 e^{i(\omega t + \beta sin\Omega t)} \tag{2.1.25}$$

With the Jacobi-Anger formula,

$$e^{i\beta sin\Omega t} = \sum_{n=-\infty}^{\infty} J_n(\beta)e^{in\Omega t}, \tag{2.1.26}$$

we can rewrite E_{in} as follows.

$$E_{in} \approx E_0 \left[J_0(\beta)e^{i\omega t} + J_1(\beta)e^{i(\omega+\Omega)t} - J_1(\beta)e^{i(\omega-\Omega)t} \right] \quad (2.1.27)$$

We need to know the ratio of the reflected field to this input field. We already derived it for the carrier,

$$O(\omega) = \frac{E_{ref}}{E_{in}} = \frac{r_1 - r_2(r_1^2 + r_2^2)e^{-2ikL}}{1 - r_1 r_2 e^{-2ikL}}. \quad (2.1.28)$$

For sidebands, we can still use this equation just by changing the frequency. Therefore,

$$E_{ref} = E_0 e^{i\omega t} \left[O(\omega)J_0(\beta) + O(\omega+\Omega)J_1(\beta)e^{i\Omega t} - O(\omega-\Omega)J_1(\beta)e^{-i\Omega t} \right]. \quad (2.1.29)$$

Since what photodetectors sense is not electric field but power, we need to calculate power.[2]

$$P_{ref} = |E_{ref}|^2 = (E_{ref})(E_{ref})^* \quad (2.1.30)$$

After some calculation, we get

$$\begin{aligned} P_{ref}/|E_0|^2 &= |O(\omega)|^2 J_0^2 + |O(\omega+\Omega)|^2 J_1^2 + |O(\omega-\Omega)|^2 J_1^2 \quad (2.1.31) \\ &+ 2Re\left\{O(\omega)O^*(\omega+\Omega) - O^*(\omega)O(\omega-\Omega)\right\} J_0 J_1 cos\Omega t \\ &- 2Im\left\{O(\omega)O^*(\omega+\Omega) - O^*(\omega)O(\omega-\Omega)\right\} J_0 J_1 sin\Omega t \\ &+ 2\Omega terms. \end{aligned}$$

That is, the reflected power consists of terms at DC, at Ω, and at 2Ω. Demodulation

---

[2]We do not care some factor in the expression for convenience.

is done by multiplying $sin\Omega t$ or $cos\Omega t$ and averaging over one period. The former case is called in-phase (I-phase) and the latter case is called quadrature phase (Q-phase). When the carrier is resonant in the cavity, only the quadrature phase ($sin\Omega t$) survives in a reflected field. The demodulated signal called *error signal*.

$$P_{demod} = 2J_0J_1|E_0|^2 Im\left\{O(\omega)O^*(\omega+\Omega) - O^*(\omega)O(\omega-\Omega)\right\} \qquad (2.1.32)$$

Figure 2.3 shows above expression as a function of displacement from resonance. The linear signal around the origin allows us to judge which way the mirror is offset so that we can use the signal to keep the cavity on resonance by feedback control.
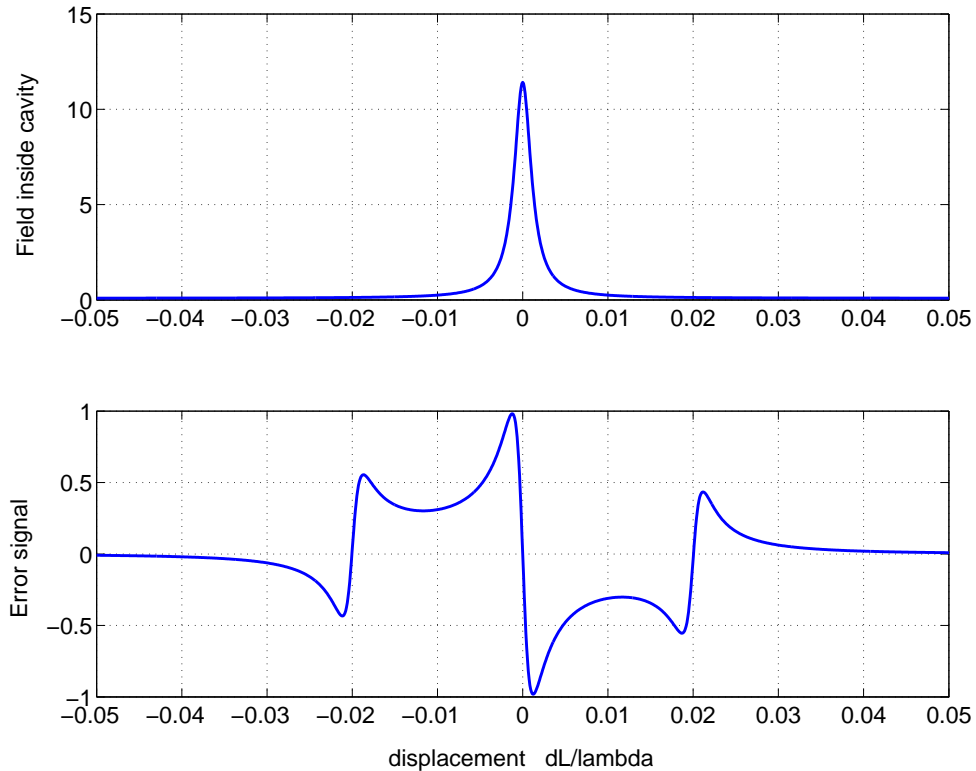
Figure 2.3: Pound-Drever-Hall error signal. The parameters from table 1.1 are used for the calculation except the modulation frequency. Four percent of FSR is used here.

Notice that the quadrature-phase of the error signal is nothing but the imaginary part of $e^{-i\Omega t}$ term, and the in-phase is the real part of it. Thus, when we write the electric field at output port as

$$E_{out} = E^{CR} + E^{SB+} + E^{SB-}, \tag{2.1.33}$$

the demodulated signal becomes

$$S = E^{CR*}E^{SB-} + E^{SB+*}E^{CR}. \tag{2.1.34}$$

And, in-phase and quadrature-phase is given by real part and imaginary part of it, respectively. This view is very useful when we consider wave front sensing in the next chapter.

This technique is implemented in the LIGO interferometer's length sensing and control (LSC) system [28, 42]. Although the optical configuration is more complicated, the basic scheme is the same. Each LIGO interferometer needs to control the length of its two arm cavities and two Michelson arms, and suitable detection ports for each degree of freedom have been chosen. For example, the anti-symmetric port is used to sense differential arm cavity length dL.

$$S_{AS} \propto dL + \frac{\pi}{\mathcal{F}}dl \approx dL \tag{2.1.35}$$

where $\mathcal{F}$ is *finesse* of arm cavity.[3]

---

[3]At the anti-symmetric port, sideband is used as the reference. In order to do it, asymmetry in Michelson length called Schnupp asymmetry ($l_1 \neq l_2$) is introduced to allow sideband to exist there. Otherwise, Pound-Drever-Hall technique could not be used since sideband is also tuned to be resonant in recycling cavity.

2.1.3   Response of detector

We now know that a gravitational wave causes a phase change in a Fabry-Perot cavity and it is related to arm length change. In gravitational wave detector, the output of the detector is the time series of the arm length difference. The time series is constructed through calibration, which will be discussed shortly, using photodetector signals tuned to be sensitive to the phase shift in the two resonant arms. Here, we derive the response of the photodetector signal to the presence of gravitational wave.

A electromagnetic field (the laser light with frequency ω), will be modulated by the presence of gravitational wave of frequency Ω. Thus, the frequency spectrum of the light consists of a carrier ω and two sidebands $\omega \pm \Omega$ (up to the first sidebands). The sidebands are sometimes called *audio* sidebands as opposed to *RF* sidebands used in servo controls. Or, more explicitly, the electromagnetic field can be written as

$$E(t) = \left(E_0 + E_1 e^{-i\Omega t} + E_2 e^{i\Omega t} \right) e^{-i\omega t}. \tag{2.1.36}$$

In the previous subsection, we saw that gravitational wave produces phase shift during one round trip acting on carrier light. This can be understood as energy transfer from carrier to sidebands [26, 27, 24]. So, the round trip operator X can be written as

$$E' = \begin{pmatrix} 1 & 0 & 0 \\ -\frac{i}{2}\Delta\Phi_{rt} & e^{-2i\Omega L/c} & 0 \\ -\frac{i}{2}\Delta\Phi_{rt}^* & 0 & e^{2i\Omega L/c} \end{pmatrix} \begin{pmatrix} E_0 \\ E_1 \\ E_2 \end{pmatrix} \tag{2.1.37}$$

$$E' = XE, \tag{2.1.38}$$

where we assume that L has been chosen so that $e^{-2i\omega L/c+2i\eta}$ is set to unity for resonant condition. (η is the Gouy phase shift which will be discussed in chapter 3.) Since X is analog to the phase shift e^{-2ikL} in (2.1.18), we can calculate the electric field inside the cavity and that reflected from the cavity using (2.1.20) and (2.1.23), respectively.

Therefore, the operators to calculate the cavity field and the reflected field will be

$$X_{circ} \;=\; t_1 \left(I - r_1 r_2 X\right)^{-1} \tag{2.1.39}$$

$$X_{ref} \;=\; \left[r_1 - r_2 \left(r_1^2 + t_1^2\right) X\right]\left(I - r_1 r_2 X\right)^{-1} \tag{2.1.40}$$

where I is the identity matrix. By straightforward calculation, we will have the following matrices.

$$X_{circ} = t_1 \begin{pmatrix} \dfrac{1}{1-r_1 r_2} & 0 & 0 \\[2ex] \dfrac{\frac{i}{2}r_1 r_2 \Delta\Phi_{rt}}{(1-r_1 r_2)\left(1-r_1 r_2 e^{-i\frac{2\Omega L}{c}}\right)} & \dfrac{1}{\left(1-r_1 r_2 e^{-i\frac{2\Omega L}{c}}\right)} & 0 \\[3ex] \dfrac{\frac{i}{2}r_1 r_2 \Delta\Phi_{rt}^*}{(1-r_1 r_2)\left(1-r_1 r_2 e^{i\frac{2\Omega L}{c}}\right)} & 0 & \dfrac{1}{\left(1-r_1 r_2 e^{i\frac{2\Omega L}{c}}\right)} \end{pmatrix} \tag{2.1.41}$$

$$X_{ref} = \begin{pmatrix} \dfrac{r_1 - r_2\left(t_1^2 r_1^2\right)}{1-r_1 r_2} & 0 & 0 \\[2ex] \dfrac{\frac{i}{2}r_2 t_1^2 \Delta\Phi_{rt}}{(1-r_1 r_2)\left(1-r_1 r_2 e^{-i\frac{2\Omega L}{c}}\right)} & \dfrac{r_1 - r_2\left(t_1^2 + r_1^2\right)e^{-i\frac{2\Omega L}{c}}}{1-r_1 r_2 e^{-i\frac{2\Omega L}{c}}} & 0 \\[3ex] \dfrac{\frac{i}{2}r_2 t_1^2 \Delta\Phi_{rt}^*}{(1-r_1 r_2)\left(1-r_1 r_2 e^{i\frac{2\Omega L}{c}}\right)} & 0 & \dfrac{r_1 - r_2\left(t_1^2 + r_1^2\right)e^{i\frac{2\Omega L}{c}}}{1-r_1 r_2 e^{i\frac{2\Omega L}{c}}} \end{pmatrix} \tag{2.1.42}$$

If gravitational wave frequency is much smaller than the free spectral range (i.e., $\Omega \ll \frac{c}{2L} \equiv \mathcal{FSR}$), the (1,0) component and (2,0) component of the reflected field operator $X_{ref,10}$ and $X_{ref,20}$ will be simplified as

$$X_{ref,10} \;=\; \dfrac{\frac{i}{2}r_2 t_1^2 \Delta\Phi_{rt}}{(1 - r_1 r_2)^2}\dfrac{1}{1 + i\frac{\Omega}{\omega_c}} \tag{2.1.43}$$

$$X_{ref,20} \;=\; \dfrac{\frac{i}{2}r_2 t_1^2 \Delta\Phi_{rt}^*}{(1 - r_1 r_2)^2}\dfrac{1}{1 - i\frac{\Omega}{\omega_c}}, \tag{2.1.44}$$

where ω_c is the cavity pole defined as follows

$$\omega_c = \frac{c}{2L} \frac{1 - r_1 r_2}{r_1 r_2}. \tag{2.1.45}$$

Now, when the incident field is purely a carrier $E = (E, 0, 0)^T$, the reflected field up to the first sidebands will be immediately,

$$
\begin{aligned}
\frac{E_{ref}}{E} &= (X_{ref,00} + X_{ref,10} + X_{ref,20}) \tag{2.1.46}\\
&\approx \frac{r_1 - r_2 \left(t_1^2 + r_1^2\right)}{1 - r_1 r_2} + \frac{i}{2} \frac{r_2 t_1^2}{(1 - r_1 r_2)^2} \left[\frac{\Delta\Phi_{rt} e^{i\Omega t}}{1 + i\frac{\Omega}{\omega_c}} + \frac{\Delta\Phi_{rt}^* e^{-i\Omega t}}{1 - i\frac{\Omega}{\omega_c}} \right] \tag{2.1.47}
\end{aligned}
$$

For the other arm, we can calculate in the same way. The field at anti-symmetric port E_{AS} will be [4]

$$E_{AS} \approx r_6 t_6 \left(X_{ref}^x - X_{ref}^y \right) E_{RC}. \tag{2.1.48}$$

E_{RC} is the field in the recycling cavity and t_6, r_6 are the transmission and the reflection coefficient of the beamsplitter. LIGO employed Pound-Drever-Hall technique where input laser light is modulated by some frequency, say ω_m. Therefore, under influence of gravitational waves, there are nine frequencies, (if we only consider the first sidebands), namely, ω, $\omega \pm \omega_m$, $\omega \pm \Omega$, $(\omega + \Omega) \pm \omega_m$, and $(\omega - \Omega) \pm \omega_m$. The last four terms are relevant for the demodulation signal. We can calculate the demodulation signal in the same way as we showed in the previous subsection, but we here use a fact that the demodulated signal is proportional to imaginary part of the cavity field [25]. Therefore, From (2.1.41), the cavity field up to the first sidebands is given by

---

[4]Phase shift in Michelson arm is ignored here. More complete formalism will be discussed in chapter 3 where Michelson length is also taken into account.

$$\frac{E_{circ,audio}}{t_1 E} = X_{circ,00} + X_{circ,10} + X_{circ,20} \tag{2.1.49}$$

$$= \frac{1}{1 - r_1 r_2} - \frac{i}{2} \frac{r_1 r_2}{1 - r_1 r_2} \left[\frac{\Delta\Phi_{rt} e^{i\Omega t}}{1 - r_1 r_2 e^{-i\frac{2\Omega L}{c}}} + \frac{\Delta\Phi_{rt}^* e^{-i\Omega t}}{1 - r_1 r_2 e^{i\frac{2\Omega L}{c}}} \right] \tag{2.1.50}$$

$$\approx \frac{1}{1 - r_1 r_2} - \frac{i}{2} \frac{r_1 r_2}{(1 - r_1 r_2)^2} \left[\frac{\Delta\Phi_{rt} e^{i\Omega t}}{1 + i\frac{\Omega}{\omega_c}} + \frac{\Delta\Phi_{rt}^* e^{-i\Omega t}}{1 - i\frac{\Omega}{\omega_c}} \right] \tag{2.1.51}$$

$$\approx \frac{1}{1 - r_1 r_2} - i \frac{r_1 r_2}{(1 - r_1 r_2)^2} Re \left[\frac{\Delta\Phi_{rt} e^{i\Omega t}}{1 + i\frac{\Omega}{\omega_c}} \right] \tag{2.1.52}$$

Since the second term of (2.1.52) is the imaginary part of the cavity field modulated by a gravitational wave, the demodulated signal V_{AS} will be

$$V_{AS} \propto \frac{1}{\sqrt{1 + \left(\frac{\Omega}{\omega_c}\right)^2}}. \tag{2.1.53}$$

This is the response of the detector to a gravitational wave under assumptions already made. For high frequencies above the free spectral range, though, it is known that some correction from the cavity pole function is necessary [24, 25]. The demodulated signal is proportional to differential arm length and it allows us to model the detector as a one DOF($= \Delta L$) control system.
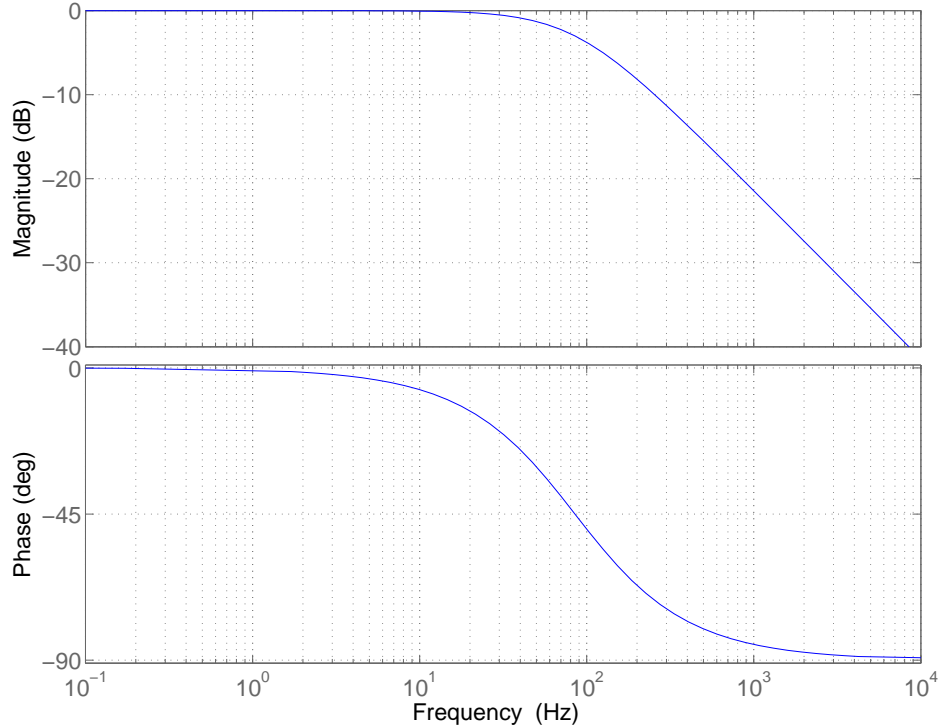
Figure 2.4: Normalized cavity pole function.

2.2 Calibration

This section summarizes calibration of differential arm (DARM) length in LIGO. The gravitational wave channel at anti-symmetric (AS) port is the most sensitive to differential arm length $\Delta L = L_x - L_y$ of the detector. It is at the anti-symmetric port that gravitational waves will appear if gravitational waves pass through detector. We described that the cavity response is expressed by a cavity pole function in the previous section. If test masses were attached in spacetime and the cavity were automatically resonant, we would not need this section. In reality, however, test masses are hung from a suspension system, and a lot of control servos work to keep cavities on resonance. Therefore, the output from the gravitational wave channel is the result of the complicated system. The job of calibration is to get response of the gravitational wave channel to gravitational waves. A fancy way of saying it is that calibration is the

filter definition of the detector in the sense that it modifies the gravitational wave's original spectral profile. The result of calibration is the response function $R(f)$, which is a mathematical model of detector response. Calibration runs take place to build the model every few months to update the model and make corrections if they are needed. The response function $R(f)$ is made of a sensing function C that is a cavity pole function, an actuation function A that gives test masses' response to control signal, and digital servo filters D in the DARM control loop. The measurement is only for A and C, not D. Since digital filter is well defined and will not change by definition.

In LIGO's current length sensing and control (LSC) scheme, we only control the end test masses (ETMX, ETMY) to keep the cavities resonant. For calibration purposes, what we need is the relation between signals at the AS port, called DARM_ERR, and the differential arm length ΔL. Calibration in LIGO provides a mathematical model (called DARM model) in every calibration run. The main focus in calibration, therefore, is to understand the cause of discrepancy between the model and measurement. In the following, the DARM model and one of the conventional calibration techniques is introduced.

2.2.1   DARM model

The detector has been modeled as a one-degree-of-freedom feedback control system. The model consists of three functions: sensing function C which describes interferometer's response to differential arm motion, servo filters D which describe several digital filter banks, and the actuation function A which describes actuators to control the end test masses. A and C contain some electronics and their Bode plots are given in the Appendix B.

AS_Q is quadrature phase (as oppose to in-phase) of demodulated signal of photodetectors at the AS port. DARM_ERR, currently usually called "the gravitational wave channel", is nearly equivalent to AS_Q, but more insensitive to change of optical gain. $x(t)$ in figure 2.5 is the difference in two arm length ΔL due to either gravitational wave signal or noise. The goal of calibration is to produce $x(t)$ (or strain $h(t)$ normal-
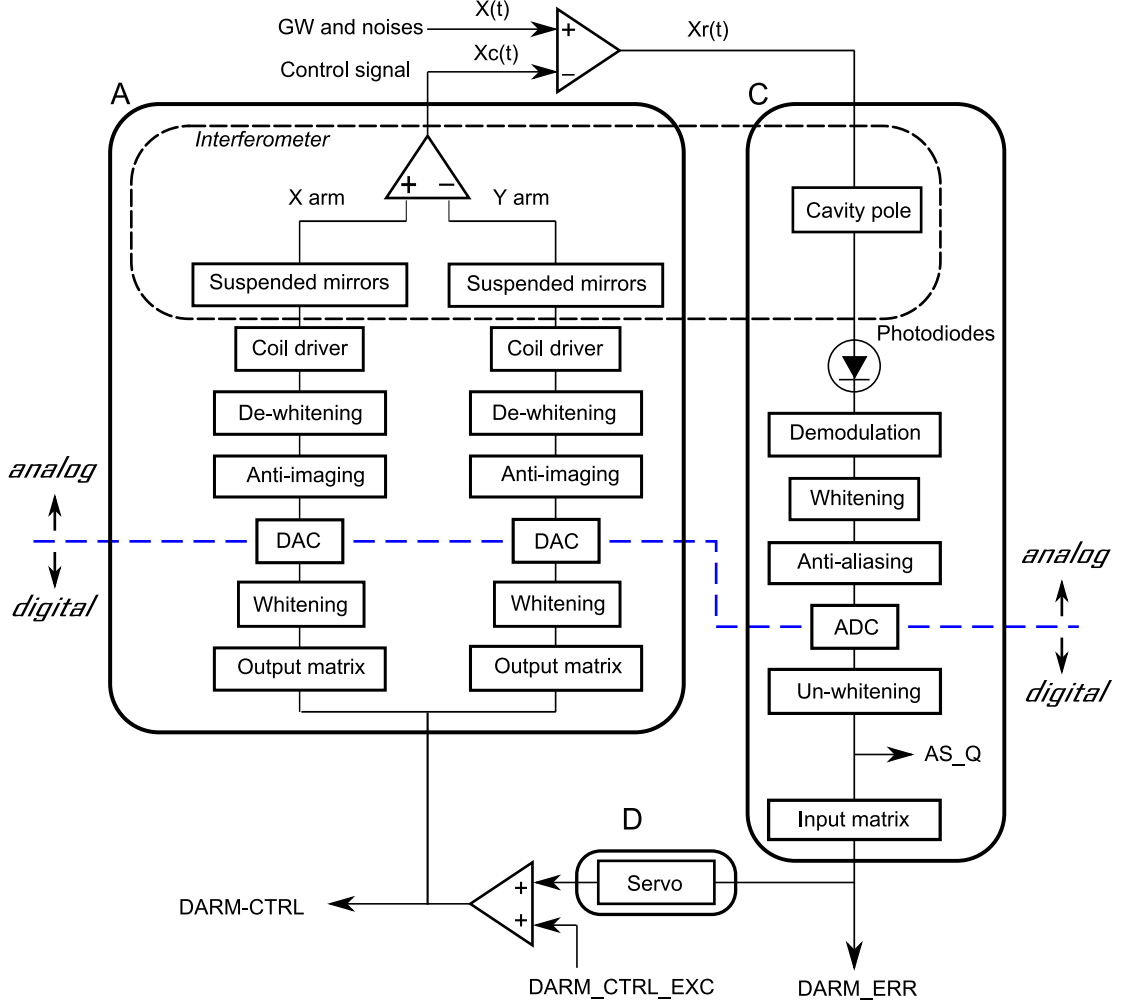
Figure 2.5: DARM model. A, C, D are the actuation function, the sensing function, and the digital filters respectively. Cavity senses Gravitational waves (GW) and noise as fluctuation and the information is fed back to end mirrors to keep cavity in resonant. DARM_ERR, DARM_CTRL, and DARM_CTRL_EXC are channel names in LIGO.

ized by cavity arm length $L = \frac{L_x + L_y}{2}$, i.e., $\frac{\Delta L}{L}$) from the gravitational wave channel (DARM_ERR, or AS_Q). The function that associates them is called the response function $R(f)$ in frequency domain.

$$
\begin{aligned}
x(f) &= R(f)d(f), & (2.2.1) \\
h(f) &\equiv \frac{x(f)}{L} = \frac{\Delta L}{L} = R'(f)d(f). & (2.2.2)
\end{aligned}
$$

27
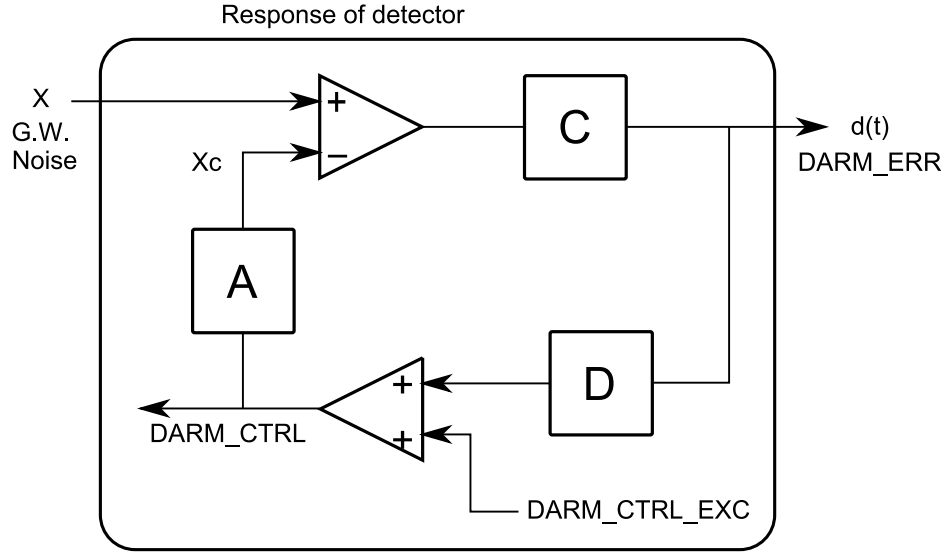
Figure 2.6: Block diagram of DARM model

$d(f)$ is DARM_ERR, and $R' = \frac{R}{L}$. Since the model is a one DOF feedback control system, the response function is simply the inverse of the closed loop transfer function of the system

$$R = \frac{1+G}{C},\tag{2.2.3}$$

where G is the open loop transfer function of DARM control loop.

$$G = CDA\tag{2.2.4}$$

Although the response function is given by (2.2.3), we know it is dominated by the sensing function in the high frequency region - roughly above 100 Hz because the open loop transfer function G is small. In the low frequency region, R is approximately the product of the actuation function and the servo function. Namely,

$$f \lesssim 100Hz \Longrightarrow R \quad \sim \quad AD \tag{2.2.5}$$

$$f \gtrsim 100Hz \Longrightarrow R \quad \sim \quad \frac{1}{C} \tag{2.2.6}$$

The next plot shows an overlay of Bode plots for R, $\frac{1}{C}$, and AD respectively.
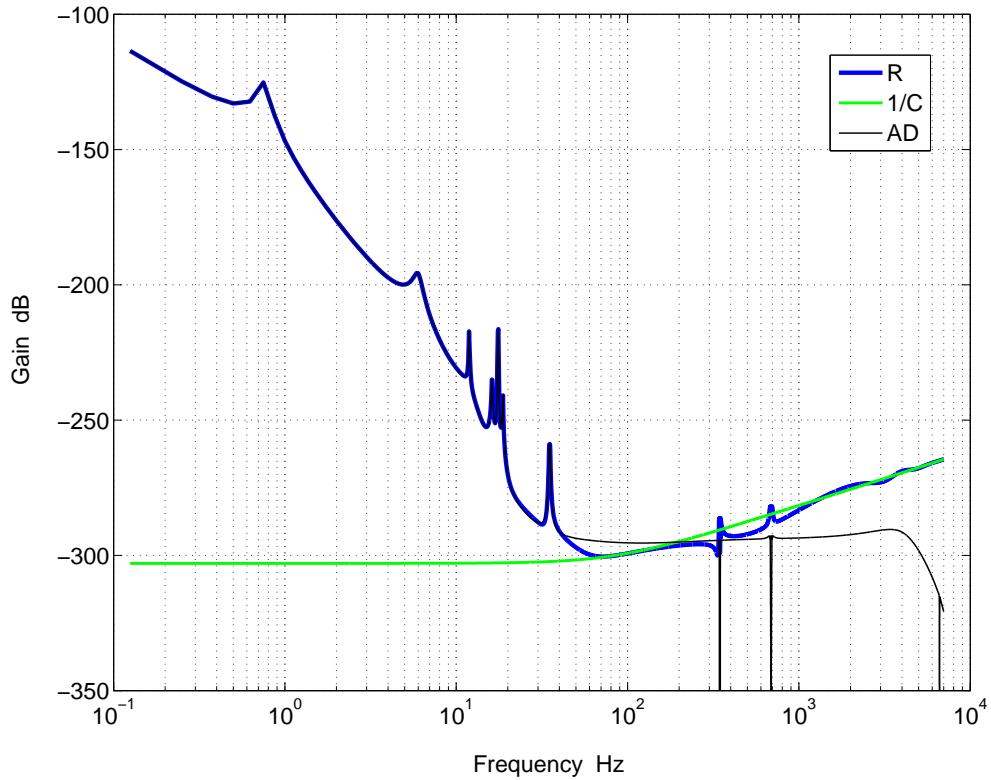
Figure 2.7: Response function. Low frequency part is governed by product of actuation and servo, while high frequency part is dominated by the inverse of sensing function.

The sensing function

The sensing function is modeled as a simple cavity pole transfer function. Cavity pole frequency is usually measured in both arms and the average is used in the model. The following is the brief description of cavity pole frequency measurement. It is known

that cavity buildup or decay follows exponential power law.

$$n = n_0 e^{-\gamma t} \tag{2.2.7}$$

where n is number of photons in cavity, t is time, and γ is decay rate, which is inverse of storage time τ_c. Therefore, the cavity pole frequency is given by

$$f_c = \frac{2\pi}{\tau_c} \tag{2.2.8}$$

Having a single arm locked (either x-arm, or y-arm), we unlock the arm cavity to record one of photodetector signals at AS port. Since number of photons is proportional to intensity of the field, we can use the DC output from photodetector to fit the exponential curve. We do the measurement a couple of times in each arm, then take the average of the two arms. The cavity pole frequency is about 90Hz according to the measurement.

The electronics in the DARM model is straightforward since we know both analog and digital components by design. The electronics around ADC (analog to digital converter) are designed to compensate each other so that their net overall gain becomes unity. The optical gain fluctuates over time, so time-varying coefficient has been introduced to absorb the fluctuation. We skip the description here, but the detail can be found in [51, 52], for example. It makes the channel DARM_ERR more stable than AS_Q in the sense that it does not see the effect of the overall loop gain change much.

The actuation function

The actuation is essentially modeled as a pendulum, but the part has two streams simply because there are two arms to make differential arm length. Similarly to the sensing part, the electronics around the DAC (digital to analog converter) are designed to have unity overall gain. The suspended mirrors are modeled as a simple second order transfer function with the pendulum's natural frequency ($\sim$0.76 Hz) and the Q value.

$$f = \frac{\omega_n^2}{s^2 + \frac{\omega_n}{Q}s + \omega_n^2} \tag{2.2.9}$$

Besides the pendulum, the model contains the output matrix, anti-imaging filters, the suspension's digital notch filters, some high frequency correction due to a test mass internal mode called drumhead mode etc. The pendulum function needs a correction which defines conversion factor between physical unit meter and digital signal unit counts and the calibration is called "DC calibration". The overall actuation is modeled as

$$A = c_x d_x f_x k_x n_x - c_y d_y f_y k_y n_y, \tag{2.2.10}$$

where f_x, f_y are pendulum transfer functions, c_x, c_y are DC calibration values, k_x, k_y are output matrix which is the feedback gain to each end test mass, n_x, n_y are notch filters built in digital suspension control loops, and d contains the others listed the above.

The servo function

The servo function is a direct copy from the complex of digital filter banks in DARM (differential arm length) control loop.
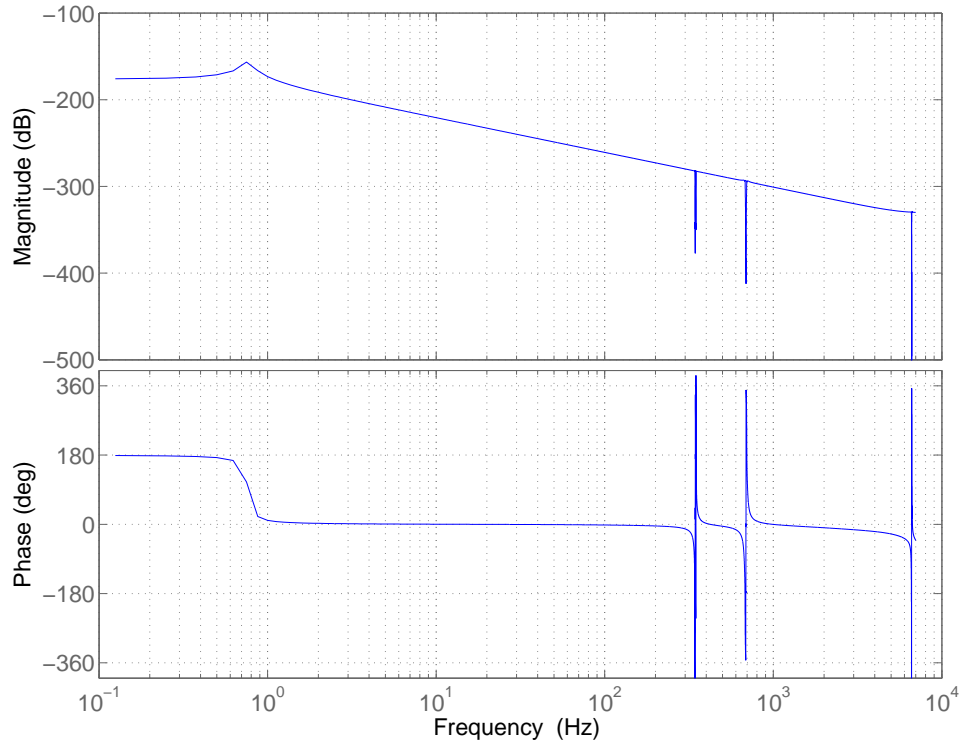
Figure 2.8: Bode plot of the actuation transfer function. The profile just looks like a product of pendulum and some notch filters although it is, in fact, a more complicated function.

The open loop transfer function

The open loop gain of the DARM control loop is measured in the following way. We inject an excitation signal into DARM loop and take ratio of two signals from points located in just upstream and downstream of the excitation point.

The response function

In this way, we build the response function - a mathematical model which is the inverse of detector response in frequency domain. The validity of the mathematical
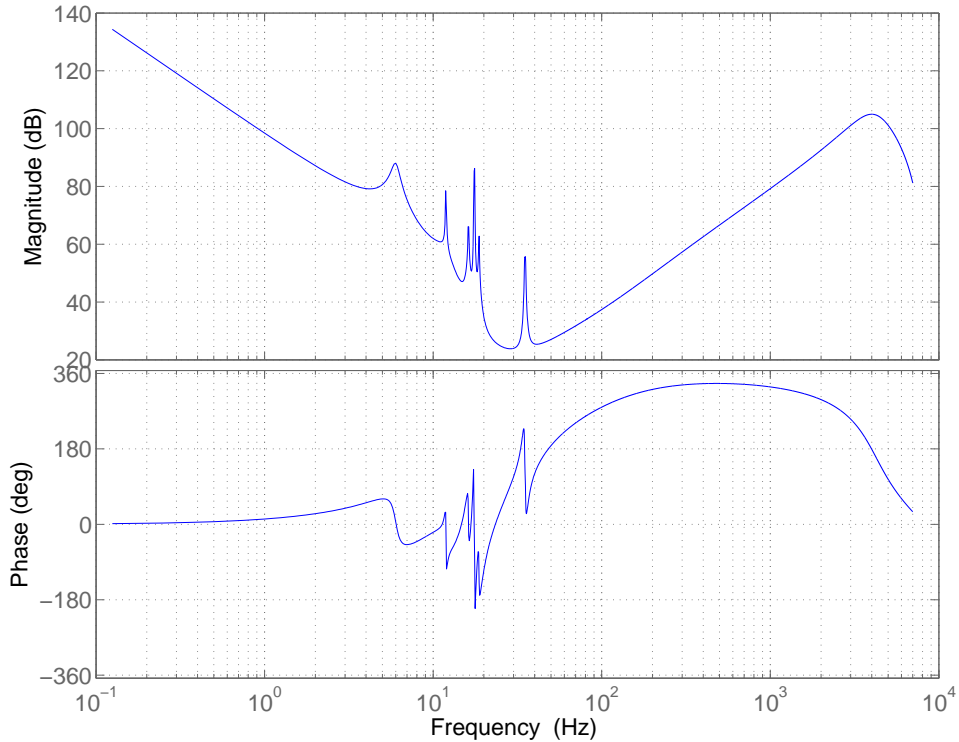
Figure 2.9: Bode plot of the servo transfer function.

model is described in [51], so here we briefly introduce the concept.[5] As we mentioned, the servo function D is known by digital filter definition. The measurement of the open loop transfer function $G = CDA$ should be reliable. So, the choice is whether we believe the sensing part is described by the cavity pole function, or the actuation part is modeled by the actuation function. In either way, the response function can be defined by (2.2.3).

Once we get the response function in frequency domain, we could produce time series of displacement $x(t)$ by using the inverse-Fourier transform. Another way of producing the $x(t)$ time series is to make use of digital filtering techniques. The method produces $h(t)$ directly from the gravitational wave signal and it will be described

---

[5]The calibration committee members have been working hard to make the calibration as accurate as possible. It is a very hard task.
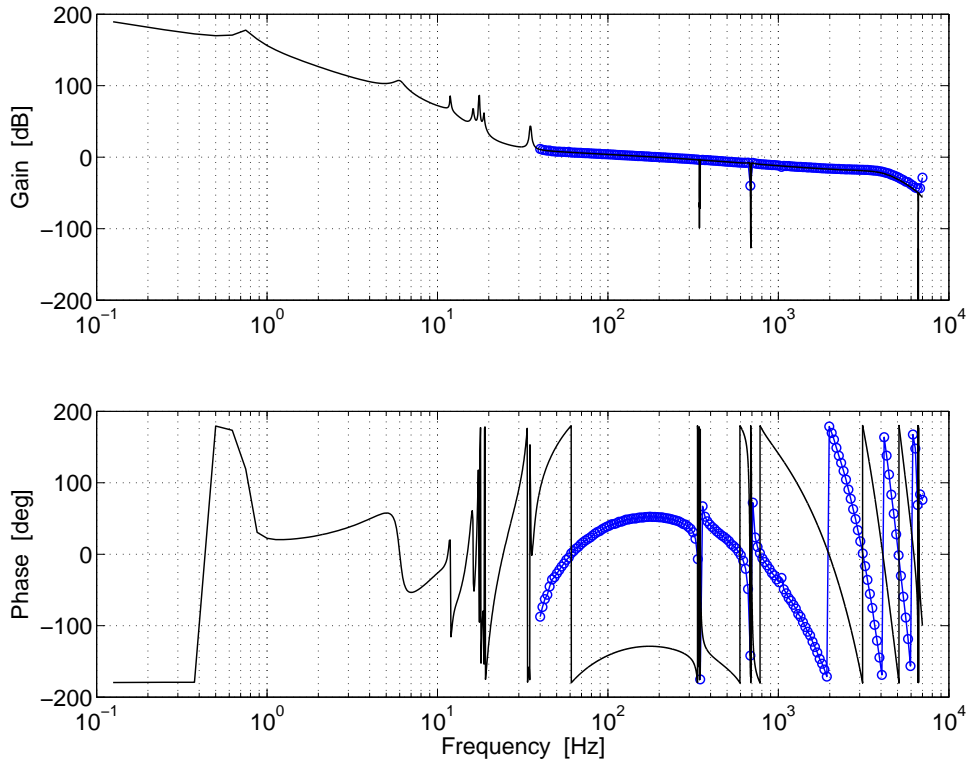
Figure 2.10: Bode plot of DARM open loop transfer function. Black is the model, and blue is the measurement.

later in this chapter. One important thing is that the method relies on the frequency domain calibration since $h(t)$ production does not have a separate calibration process.

2.2.2 DC calibration

The goal of DC calibration is to determine the relation between the excitation to each test mass (in digital unit called 'counts') and physical displacement in meters, by applying slow excitation to test masses. Slow excitation means that excitation is slow enough that the amplitude of test mass motion to the excitation can be considered a constant. Since each test mass is hung from suspension system, the amplitude should, in reality, depend on frequency of excitation, or should follow the

frequency response of the suspention system. Therefore, the frequency dependece will be taken into account afterwards. The basic idea is that we calibrate the input test masses first to AS_Q, and propagate the relation to end test masses by the *single arm lock* technique described later.

ITM DC calibration

ITM DC calibration takes place using the Michelson configuration: a Michelson interferometer is made by using part of the full interferometer, which is comprised of two input test masses (ITMX, ITMY) and the beamsplitter (BS) for our purpose. The excitation signal is injected into the length control path of one of the ITM's, and the photodetector output AS_Q at the anti-symmetric port is recorded. The input test masses are controlled to hold the Michelson interference on a dark fringe.
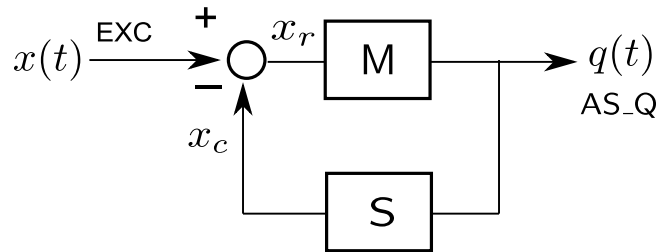
Figure 2.11: Block diagram of Michelson configuration. M stands for Michelson interferometer and S does for servo control transfer function. Michelson interferometer consists of beam splitter (BS), input test mass (ITM). In the configuration, servo controls the ITM's to keep AS_Q dark.

For following discussion, we define some variables: counts in excitation channel, displacement due to the excitation, residual displacement, and AS_Q as ε, x, x_r and q respectively. We do not distinguish the above variables from their Laplace transformed (frequency domain) variables here. From the block diagram, we can see that the relation between the excitation x and AS_Q signal's output q is given by

$$q = \frac{M}{1+G}x, \tag{2.2.11}$$

where G is the open loop gain (i.e., $G = MS$). We assume the excitation is large enough so that we can ignore other noise such as seismic, thermal, and shot noise during the measurement. Therefore,

$$
\begin{aligned}
\frac{\Delta x}{\Delta \varepsilon} &= \frac{\Delta q}{\Delta \varepsilon} \times \frac{1+G}{M} \tag{2.2.12} \\
&= \frac{\Delta q}{\Delta \varepsilon} \times (1+G) \times \frac{x_r}{q} \tag{2.2.13}
\end{aligned}
$$

The three transfer functions making up the product in the last line are exactly what we measure in the ITM DC calibration. They are called the ITM sweep, Michelson open loop gain, and freeswing kick, respectively. Let's take a look at them one by one in the following.

ITM sweep   The term $\frac{\Delta q}{\Delta \varepsilon}$ is obtained by injecting the excitation signal $\Delta \varepsilon$ in the Michelson's length control path through either x-arm or the y-arm and take the transfer function. The plot shows the Bode plot of the transfer function for both x-arm(blue) and y-arm(green).

Michelson open loop gain   The open loop transfer function is obtained by usual technique injecting excitation signal in Michelson control path and take ratio of two signals, just upstream and downstream of the excitation point.

Free swing kick   This measurement is the core of ITM DC calibration in the sense that it gives the relation between q and displacement of mirror x. We first align the mirrors to make Michelson configuration and cut off the feedback control loop so that two test masses(ITMX and ITMY) can move freely. Then, we excite one of the test masses by gently applying injection signal and making sure that the interference pat-
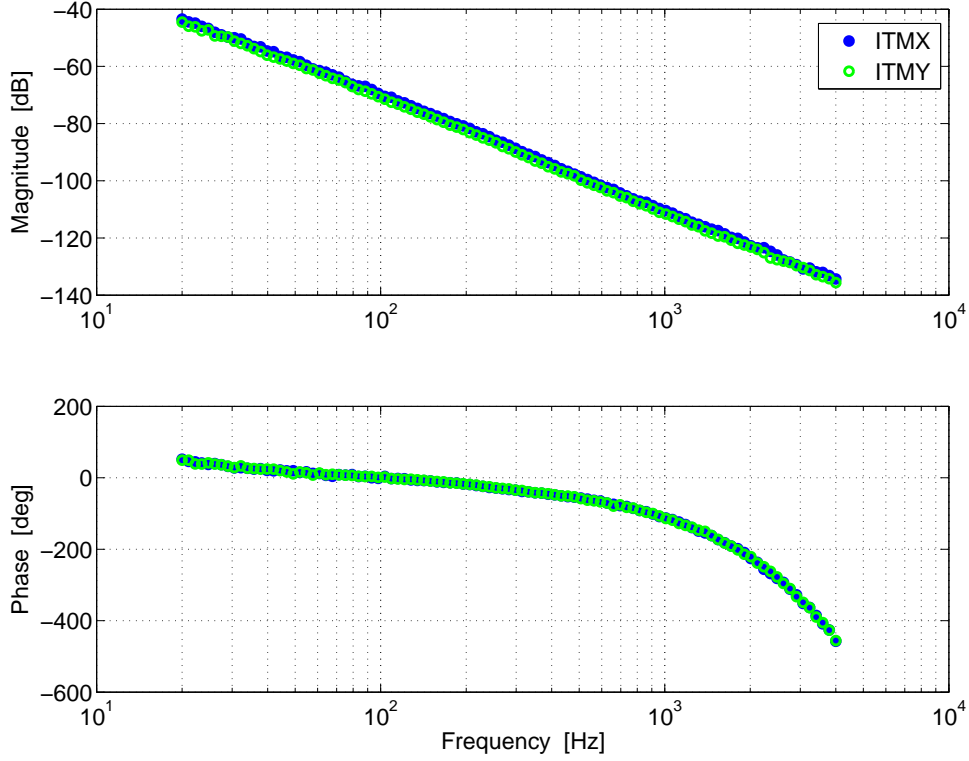
Figure 2.12: Bode diagram of ITM sweep.

tern 'blinks'. The plot shows time series of q when one of the test masses is 'kicked'. The peak-to-peak range of ADC counts corresponds to the following quantity: Since we know wavelength of laser beam, 1064 nm, peak-to-peak amplitude can be associated with the following quantity to figure out conversion factor between x_r in meters and q in counts.

$$A_{p-p} = \frac{\lambda}{2\pi} \tag{2.2.14}$$

With all three the transfer functions, we get roughly $0.5 \sim 1$ nm per count for $\Delta x/\Delta\varepsilon$. So far, we ignored the frequency dependence of the amplitude response, assuming excitation is very slow. In order to make the correction, we simply divide our DC calibration result by input test masses transfer function, which is characterised by a
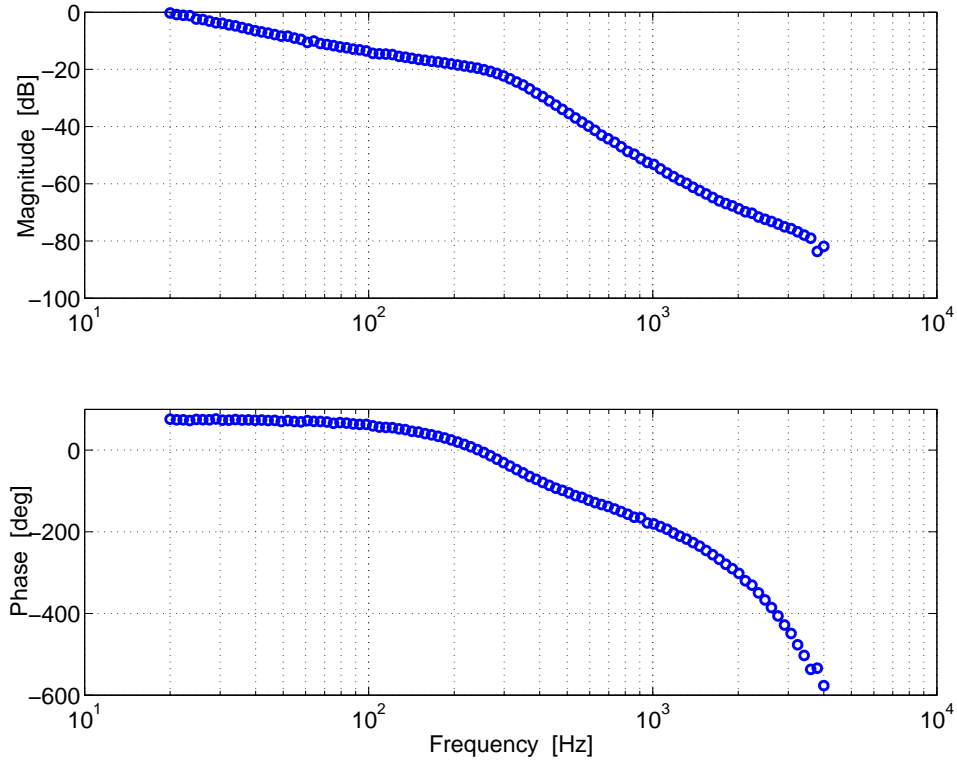
Figure 2.13: Bode diagram of MICH open loog transfer function.

simple pendulum.

$$\frac{\Delta x}{\Delta \varepsilon} \mid_{corr} = \frac{\Delta q}{\Delta \varepsilon} \left(1 + G \right) \frac{x_r}{q} / \frac{\omega_p^2}{s^2 + \frac{\omega_p}{Q} s + \omega_p^2} \qquad (2.2.15)$$

The denominator is pendulum transfer function in which ω_p, Q are pendulum natural frequency and Q value respectively.

ETM DC calibration

End test masses (ETMX, ETMY) could be calibrated in the same way as the ITM DC calibration using an asymmetric Michelson technique, where, instead of using two input test masses, the pair of ITMX and ETMY, or the pair of ITMY and ETMX
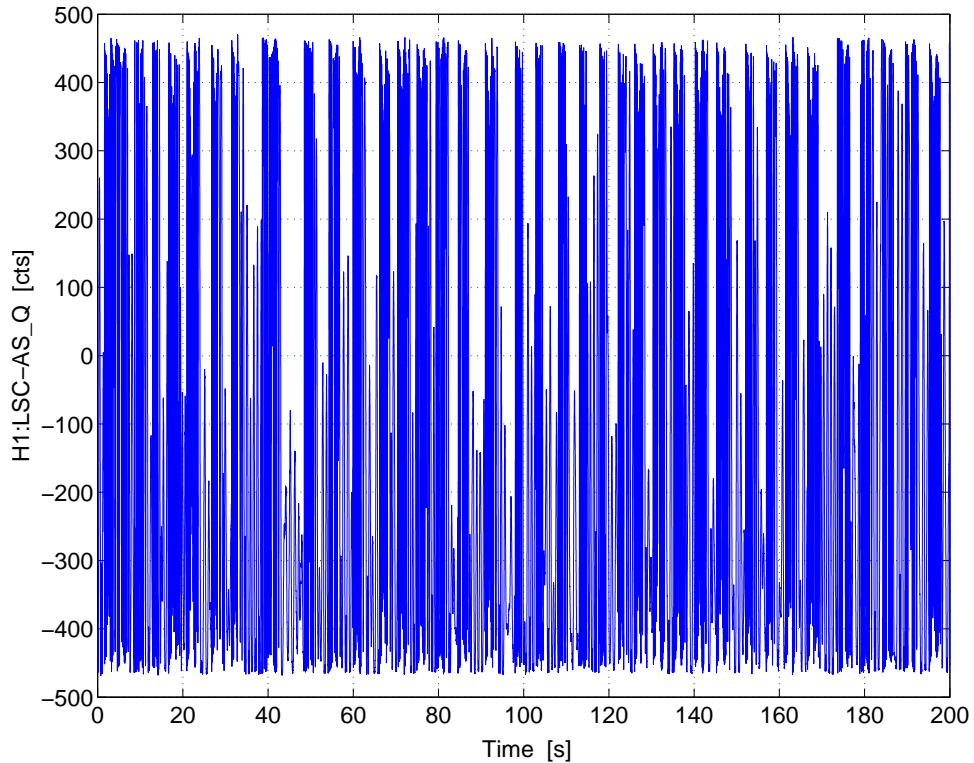
Figure 2.14: Time series of AS_Q in freeswing kick measurement

is used. We here introduce a different method - *single arm lock*. The basic idea is to propagate an excitation from an input test mass to an end test mass with a single arm being locked. Namely, as we excite the input test mass, the end test mass will follow the movement of the input test mass to keep the arm locked. The in-phase signal called AS_I is used for the measurement since AS_Q is insensitive to this configuration.[6]

Single arm lock measurement Since the ETM is controlled to keep a cavity resonant, the ETM tries to match the ITM's motion when the ITM is dithered. We use this fact to propagate displacement from the ITM to the ETM, exciting the ITM very slowly so that we can ignore the pendulum. Figure 2.16 shows the Bode plot

---

[6]AS_Q is tuned to be sensitive to differential arm length (both arm cavity's length change ΔL and Michelson arm length change Δl). For the single arm lock configuration, AS_I is more sensitive.
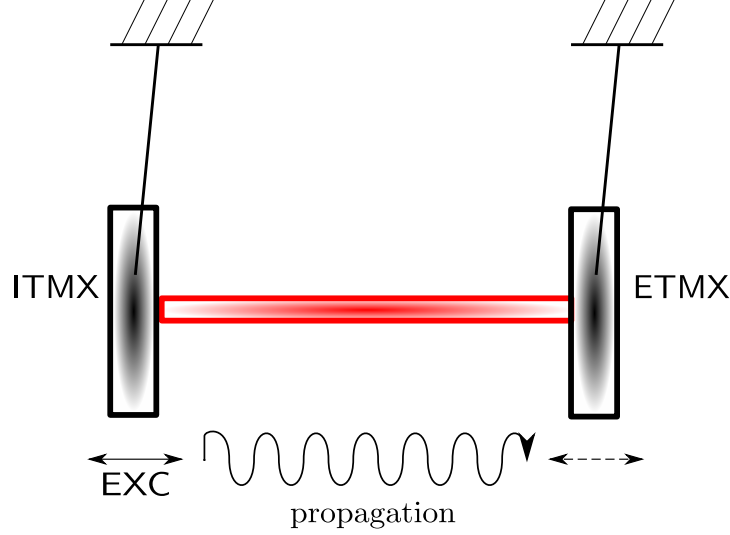
Figure 2.15: Sketch of single arm lock measurement

of AS_I signals to ITM's excitation and to ETM's excitation. The figure shows that the AS_I output response to ITM excitation, and to ETM excitation are very similar. This backs up the concept of 'propagation'. As we considered in ITM DC calibration, however, we need to take into account of pendulum motion. Let's denote the excitation of ITM, ETM as ε, δ and AS_I signal as i. Considering difference of pendulum normal frequency ω_0^{ITM}, ω_0^{ETM} between two masses, the excitation propagated from the input test mass to the end test mass is given by

$$\frac{\delta}{\varepsilon}\left(\frac{\omega_0^{ITM}}{\omega_0^{ETM}}\right)^2 = \left(\frac{i}{\varepsilon}\right)\left(\frac{\delta}{i}\right)\left(\frac{\omega_0^{ITM}}{\omega_0^{ETM}}\right)^2, \qquad (2.2.16)$$

where i/ε, i/δ are transfer functions measured as shown in figure 2.16. Combining (2.2.15) and (2.2.16), we get relation between AS_Q signal q and displacement of end test masses x.

$$\begin{aligned}
\frac{\Delta x}{\Delta \delta} &= \frac{\Delta x}{\Delta \varepsilon}|corr \times \left(\frac{\varepsilon}{i}\right) \times \left(\frac{i}{\delta}\right) \times \left(\frac{\omega_0^{ETM}}{\omega_0^{ITM}}\right)^2 \\
&= \frac{\Delta q}{\Delta \varepsilon}(1+G)\frac{x_r}{q} / \frac{\omega_p^2}{s^2 + \frac{\omega_p}{Q}s + \omega_p^2} \times \left(\frac{\varepsilon}{i}\right) \times \left(\frac{i}{\delta}\right) \times \left(\frac{\omega_0^{ETM}}{\omega_0^{ITM}}\right)^2 \quad (2.2.17)
\end{aligned}$$

After all this work, this relation lets us know how much we must move the end mirrors to keep Fabry-Perot cavities in resonance. It means, equivalently, we know how much differential arm length ΔL is in terms of ADC counts.
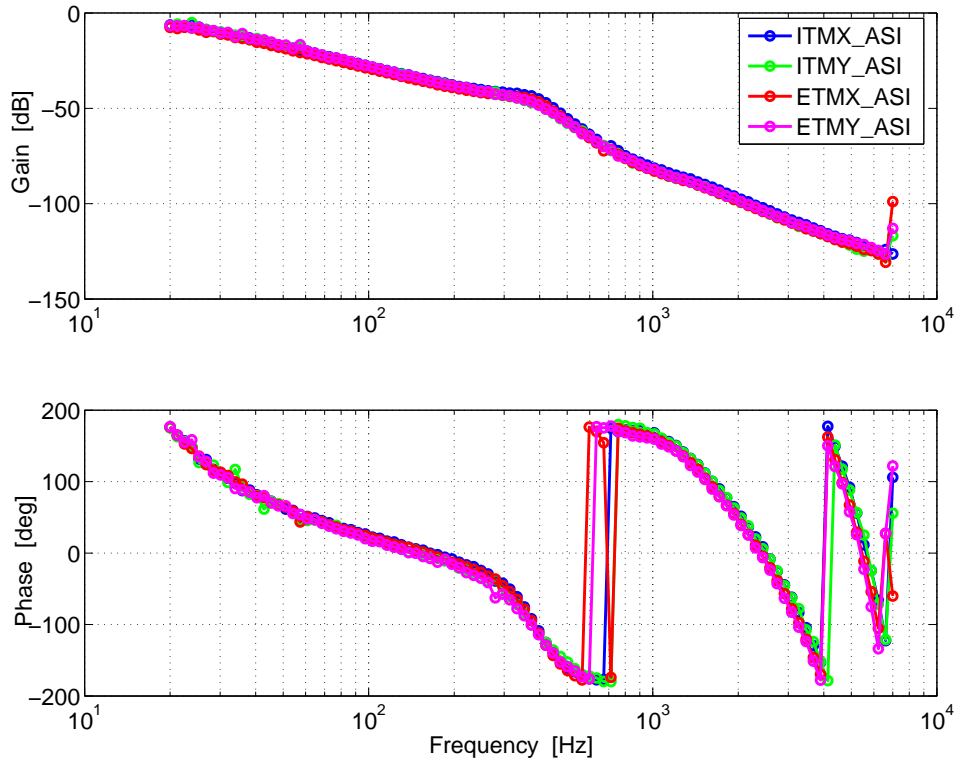
Figure 2.16: Bode plot of AS_I measurement

2.3   Generation of $h(t)$

As described in the previous section, the response function $R(f)$ (transfer function from photodetector output $d(f)$ in gravitational wave channel to differential arm strain $h(f)$) is determined in the frequency domain calibration. Strain in the time domain can be generated by inverse-Fourier-transforming $h(f)$. LIGO has developed rather a different method using digital filters, which is called $h(t)$ generation [50]. The process is sometimes called time domain calibration, but it is somewhat of a misnomer in the sense that there is no calibration *per se* in the $h(t)$ generation process. What we do in reality is to design digital filters to mimic time series of strain $h(t)$ based on the frequency domain calibration.

2.3.1   Z-transform

Generation of $h(t)$ is based on the frequency domain calibration described in the previous section. In the frequency domain, we have

$$R(i\omega) = \frac{H(i\omega)}{Q(i\omega)}. \tag{2.3.1}$$

R, Q, H are response function, Fourier transformed signal in gravitational channel, and Fourier transformed strain respectively. In principle, we could generate $h(t)$ by inverse Fourier transform once we have strain in Fourier domain $H(i\omega)$. Mainly for convenience, LIGO decided to use an alternative method similar to convolution in the continuous world.

$$h(t) = \int_{-\infty}^{\infty} r(\tau)q(t-\tau)d\tau. \tag{2.3.2}$$

The equivalent in the digital world can be given using an IIR filter,

$$h(n) = Q(z)\sum_{k=0}^{N} b(k)q(n-k) + H(z)\sum_{k=1}^{M} a(k)h(n-k) \qquad (2.3.3)$$

$$R(z) = \frac{H(z)}{Q(z)} = \frac{\sum_{k=0}^{N} b(k)z^{-k}}{1 - \sum_{k=1}^{M} a(k)z^{-k}} \qquad (2.3.4)$$

or using an FIR filter,

$$h(n) = \sum_{k=0}^{m-1} b'(k)q(n-k) \qquad (2.3.5)$$

$$R(z) = \frac{H(z)}{Q(z)} = \sum_{k=0}^{N} b'(k)z^{-k}. \qquad (2.3.6)$$

The z-transform [54][55] has been used in the above expressions. In general, the z-transform is defined as follows.

$$X(z) = \sum_{n=-\infty}^{\infty} x(n)z^{-n} \qquad (2.3.7)$$

where $x(n)$ is digital time series and z is a complex number defined by $z = re^{i\omega} \subset C$. If we apply the z-transform to $y(n) = x(n-1)$,

$$Y(z) = \sum_{n=\infty}^{\infty} y(n)z^{-n} = \sum_{n=\infty}^{\infty} x(n-1)z^{-n} \qquad (2.3.8)$$

$$= \sum_{n=\infty}^{\infty} x(k)z^{-(k+1)} = \sum_{n=\infty}^{\infty} x(k)z^{-k}z^{-1} \qquad (2.3.9)$$

$$\therefore Y(z) = z^{-1}\sum_{n=-\infty}^{\infty} x(k)z^{-k} = z^{-1}X(z). \qquad (2.3.10)$$

Therefore, we can identify time delay with multiplication of z^{-1} in z-domain.

43
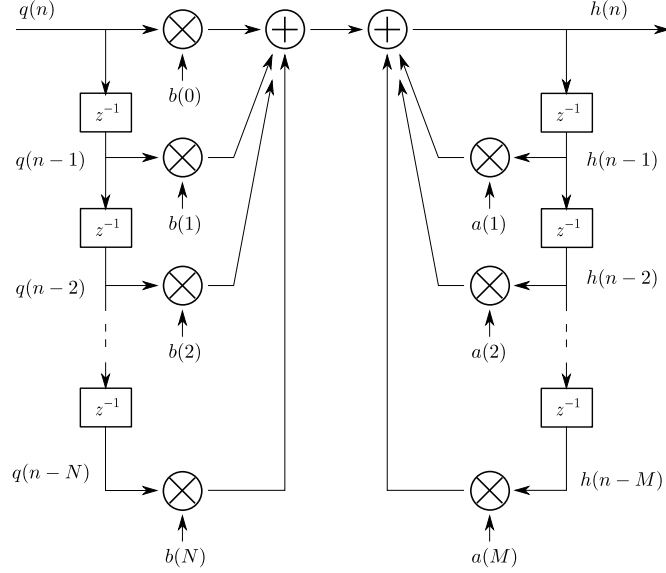
Figure 2.17: IIR filter structure. $h(n)$ is generated using $q(k)$ and $h(k)(k < n)$. If all $a(k)s$ are zero, the structure will be the same as FIR filter, and $h(n)$ is made only from $q(k)s$.

Once we have response function in the z-domain, the time series $h(n)$ is given immediately. Therefore, the goal here is to define either $a(k)s$ and $b(k)s$ for the IIR filter, or $b(k)s$ for the FIR filter. In S5 V3, we employed FIR filters to replace all the transfer functions in the DARM model, A, C, and D.

2.3.2 Bilinear transform and unit impulse response

We define IIR filters as intermediate products toward FIR filters - final products to generate $h(t)$. (We could have IIR filters as our final products. The choice of the two filter types is essentially a matter of taste although each has some pros and cons [58].) The *bilinear transform* method is used to approximate the response function $R(i\omega)$ with $R(z)$. We make corrections, usually adding some delays, to minimize the difference between the original frequency response and the new frequency response. The correction is necessary since the bilinear transform is just an approximation to the z-transfrom. Then, with the coefficients obtained in IIR filter design, using unit impulse response, we design FIR filters. We use a commercial code MATLAB [60]

in the filter design process. The following is a brief overview of the filter design procedure.

Bilinear transform

In order to do the z-transform, we use the bilinear transform by the following substitution.

$$s = \frac{2}{t_s} \left(\frac{1 - z^{-1}}{1 + z^{-1}} \right) \tag{2.3.11}$$

where t_s is the IIR filter's sampling period, or inverse of sampling rate $1/f_s$. We either use the same sampling rate of gravitational wave channel 16384 Hz or use a somewhat higher sampling rate (This is called upsampling), $f_s = p_{up} \times f_g$, where f_g is 16384 Hz in iLIGO, sampling rate of gravitational wave channel and the factor p_{up} is usually 4 to 8. After the insertion, rewriting the new transfer function in the z-domain, the IIR digital filter coefficients $b(k)'s$ and $a(k)'s$ are easily acquired by inspection. The bilinear transform maps the whole s-plane to z-plane, and it conveniently maps entire left-half s-plane into the interior of the unit circle around the origin in the z-plane.
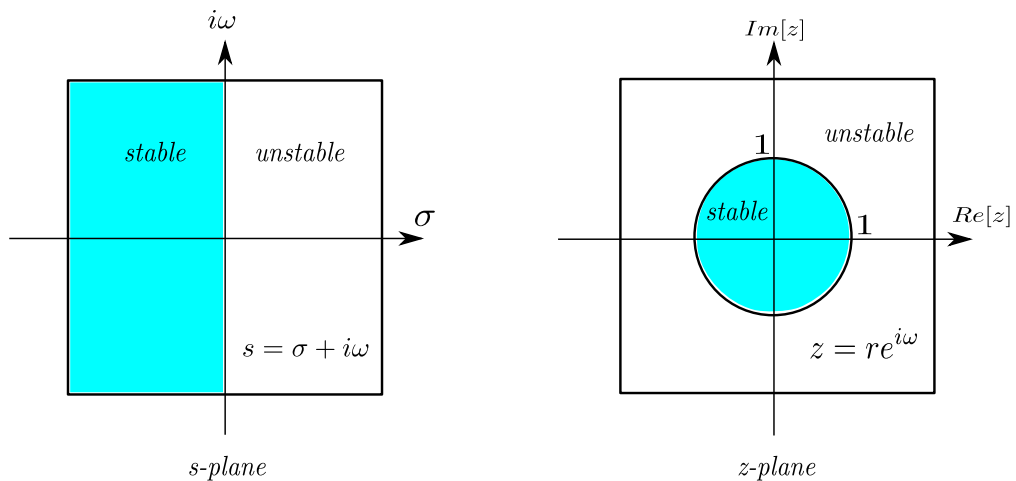
Figure 2.18: Bilinear transform. It maps the s-plane into the z-plane. The entire left half plane in the s domain (The stable region for pole locations in a linear system) is transformed into the interior of the unit circle in the z domain.

When we design digital filters, stability is one of the most important things to be

satisfied. Figure 2.19 shows the impulse response (will be described shortly) of the IIR filter for the sensing function. The red curve does not converge while the blue curve does. In general, we need the converging behavior like the blue one here in IIR filter design. The red one will introduce an oscillatory behavior and it hardly matches up with the original sensing function in the frequency domain when we compare the frequency response of the two. We will explain how we obtained the blue one in the description of filter design of the sensing function.
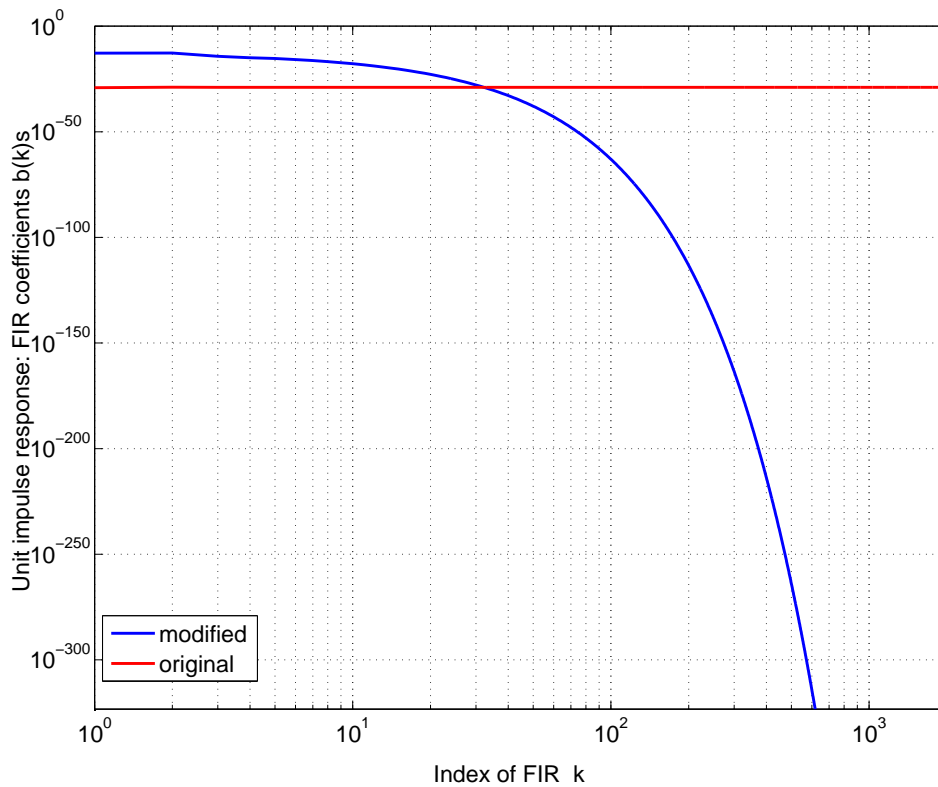
Figure 2.19: Unit impulse response of sensing FIR filter. Red is the absolute value of the impulse response of IIR filter calculated by bilinear transform of the inverse of the original sensing function, while red is the modified one. We cannot use the red one for two reasons: The frequency response is more different from the original sensing function, and the filter introduces oscillatory behavior.

Unit impulse response

Since our calibration model is linear-time-invariant (LTI), we can use unit impulse response to get all digital filters $b(k)'s$ in FIR filter. Unit impulse is the response to input time series where $x(n) = 1$ for $n = 1$, otherwise $x(n) = 0$. The feature *time-invariant* is characterized in such a way that for a system which results in $y(n)$ to some input $x(n)$, the time shift caused in the input $x(n+k)$ will result in $y(n+k)$ (k is some integer). If q in (2.3.5) is the unit impulse, output series is made of FIR coefficients $b(k)'s$.
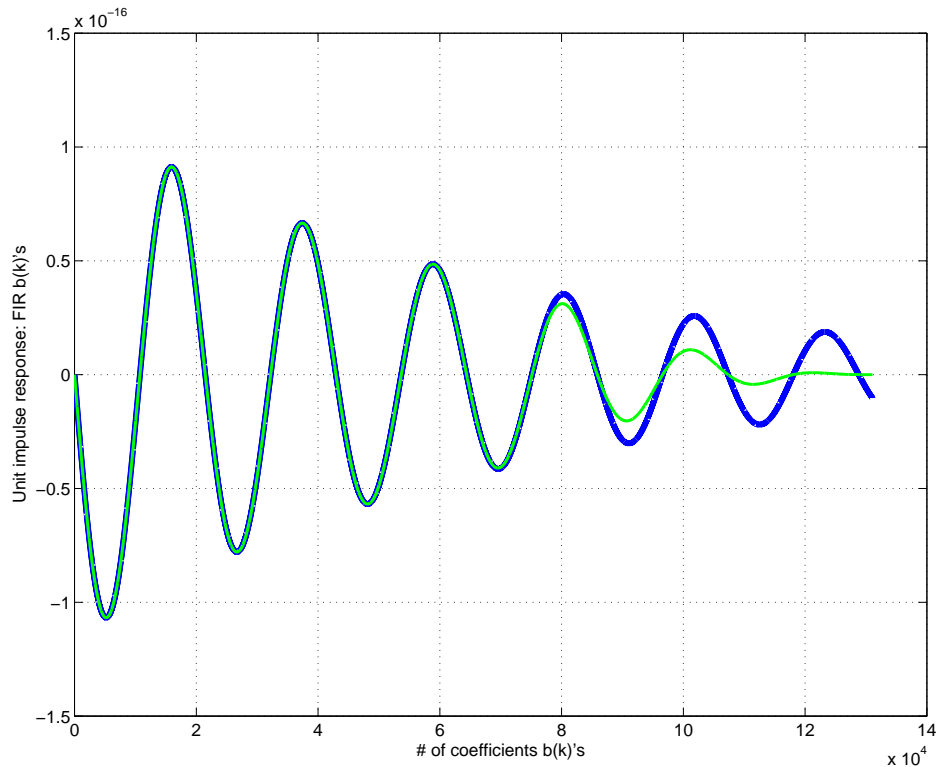
Figure 2.20: Unit impulse response of actuation FIR filter. Curve contains 16384×8 points which are identical to the FIR coefficients $b(k)'s$. Green curve is Hann-windowed filter while blue is not windowed. The duration time is typically several seconds, which is chosen after some trial and error process.

For example, figure 2.20 shows the impulse response of a FIR filter for actuation

function. The plot is made of 16384×8 points, and each of them is exactly the filter coefficient of the FIR filter. The duration, 8 seconds, is chosen after some trial and error process. Green curve shows Hann-windowed response while the blue curve is not windowed at all. The Hann window is defined as follows. We use the right half of the window whose value goes from one to zero in order for filter coefficients to reach zero faster.

$$hann(n) = 0.5 \left(1 - cos \left(2\pi \frac{n}{N} \right) \right), 0 \leq n \leq N$$

The response itself (the whole set of coefficients) is exactly what we need, i,e., the $b(k)'s$

2.3.3 Filter design

In the following, we explain how we designed filters for each function to construct $h(t)$. The way is *ad hoc* - filters were designed through some trial and error method. We design filters for A, D, and C separately and check whether the frequency response reproduces the official function defined in the frequency domain calibration. In order to have good agreement with the official functions, we usually adjust upsampling factor, extra time delay, and length of filters (number of filter coefficients) etc. The *ad hoc* method was allowed since $h(t)$ is historically generated several months after the data is acquired. However, for much smaller latency, we will need to come up with a more automatic way where a designer is not needed any more. Some effort toward this direction is being made by X. Seimens [55].

Actuation

Besides the pendulum transfer function, the actuation function contains some other functions such as suspension digital notch filters, high frequency correction for the test mass's drumhead mode, anti-imaging filters etc as we mentioned earlier. In the digital filter design, we z-transform the pendulum transfer function for both arms.

Suspension filters are already digital by definition (LIGO employs digital control system). All other functions are replaced by an extra delay. Namely, the actuation function is given by

$$A = (d_{x,sys} f_x n_x - d_{y,sys} f_y n_y) , \qquad (2.3.12)$$

where f_x, f_y are digitized pendulum functions, and n_x, n_y are digital suspension filter implemented in digital control system. d_{sys} is a delay function which absorbs all the other functions that originally existed in frequency domain model. The output matrix is already absorbed in the pendulum functions. As mentioned in the calibration section, the pendulum is modeled as a second-order transfer function.

$$f = \frac{\omega_n^2}{s^2 + \frac{\omega_n}{Q} s + \omega_n^2} \qquad (2.3.13)$$

Inserting $s = \frac{2}{t_s} \frac{1-z^{-1}}{1+z^{-1}}$ into the above, we will get

$$f_{bl} = \frac{\frac{\omega_n^2}{a^2 + \omega_n a + \omega_n^2} \left(1 + 2z^{-1} + z^{-2}\right)}{1 + \frac{2(\omega_n^2 - a^2)}{a^2 + \omega_n a + \omega_n^2} z^{-1} + \frac{a^2 - \omega_n a + \omega_n^2}{a^2 + \omega_n a + \omega_n^2} z^{-2}}, \qquad (2.3.14)$$

where $a = \frac{2}{t_s}$. By inspection, we have the IIR filter coefficients as follows.

$$\begin{aligned}
b(0) &= \frac{\omega_n^2}{a^2 + \omega_n a + \omega_n^2} \\
b(1) &= \frac{2\omega_n^2}{a^2 + \omega_n a + \omega_n^2} \\
b(2) &= \frac{\omega_n^2}{a^2 + \omega_n a + \omega_n^2} \\
a(1) &= -\frac{2\left(\omega_n^2 - a^2\right)}{a^2 + \omega_n a + \omega_n^2} \\
a(2) &= -\frac{a^2 - \omega_n a + \omega_n^2}{a^2 + \omega_n a + \omega_n^2}
\end{aligned}$$

Notch filters are digital filters defeined as follows.

$$n = \prod_k n_k \tag{2.3.15}$$

$$n_k = \frac{1 + b_k(1)z^{-1} + b_k(2)z^{-2}}{1 - a_k(1)z^{-1} - a_k(2)z^{-2}}, \tag{2.3.16}$$

where the a's and b's here are not related to the actuation function's coefficients.[7] Each function's s-domain expression will be

$$n_k\left(s\right) = \frac{s^2 + \frac{\omega_k}{Q_1}s + \omega_k^2}{s^2 + \frac{\omega_k}{Q_2}s + \omega_k^2} \tag{2.3.17}$$

The bilinear transform is not a complete z-transform but rather an approximation, so some corrections are needed. In addition, other functions in the frequency model can be absorbed in the delay function together when we design the delay function. As said, this is completely *ad hoc* since we do not know if this works or not a *priori*. Nevertheless, our typical delay function in actuation is

---

[7]We are abusing $a(k)'s$ and $b(k)'s$ in this section, but hope there is no confusion judging from the context.

$$d_{sys} = b(0) + b(1)z^{-1}. \tag{2.3.18}$$

Designing both for the x-arm and y-arm, putting everything together, we make an actuation function by (2.3.12). If we chose an IIR filter as our $h(t)$ product, the expression would be our goal. In order to have the unit impulse response of the actuation function, we use a unit impulse response as a cascade. Suppose we already have the filter coefficients for a function y_1 and a function y_2, and denote the each function as $y_1 = y_1(X)$ and $y_2 = y_2(X)$, where X is some input time series. Now, we want to know the response of the function $y_1 y_2$ to the unit impulse $x(n)$. If we denote y_1's response to a unit impulse $x(n)$ as $y_1 [x(n)]$, then we can use the $y_1 [x(n)]$ as the input for impulse response of $y_1 y_2$, i.e.,

$$y_1 y_2 [x(n)] = y_2 (y_1 [x(n)]) \tag{2.3.19}$$

Using this method, we obtain FIR filter coefficients for actuation function.

Sensing function

The sensing function is a cavity pole function scaled by optical gain, as described above. Without the optical gain scaling, the normalized sensing function is

$$C(i\omega) = \frac{1}{1 + i\frac{\omega}{\omega_c}} = \frac{\omega_c}{s + \omega_c}, \tag{2.3.20}$$

where $\omega_c = 2\pi f_c$. Now we perform a bilinear transform simply by substituting (2.3.11),

$$C(z) = \frac{1 + z^{-1}}{\left(1 + \frac{1}{t_s \omega_c}\right) + \left(1 - \frac{1}{t_s \omega_c}\right) z^{-1}}. \tag{2.3.21}$$

Since the response function has a form $R = \frac{1+G}{C}$, the inverse of the sensing function will be used in the response function. Therefore, the zero in the above expression turns into a pole in the z-plane, which will be trouble since $z = -1$ gives an oscillatory impulse response (see figure 2.19) - not stable. So, in order to avoid the instability, we place a zero at very high frequency (80 kHz for V3) by which the original cavity pole function is not affected.
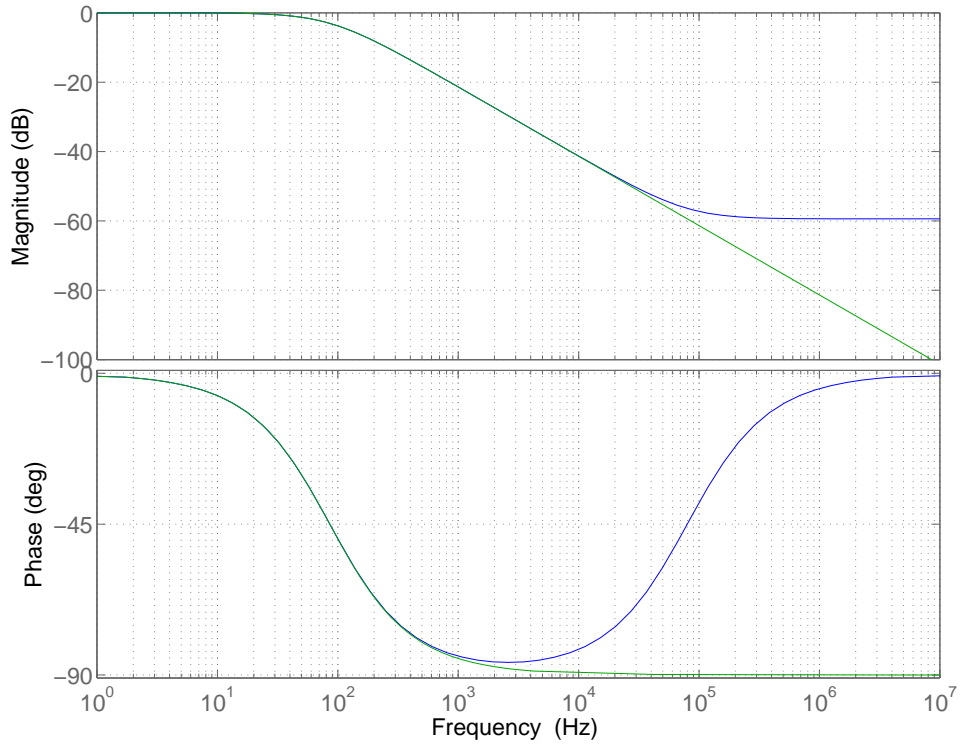
Figure 2.21: Modified sensing function. Blue is the modified sensing function while green is the original. In order to kill the oscillatory behavior in a z-transformed sensing function, a zero is placed at 80 kHz. The inverse of the modified sensing function is stable.

The procedure to design a sensing FIR filter is very similar to the actuation filter design. One difference, though, is that we use an upsampling factor when we digitize the original cavity pole function. A bilinear transform is used to obtain the IIR filter coefficients, and delay functions are introduced. Then using unit impulse response with some appropriate duration time T ($\sim$ 15 ms), we get the FIR filter coefficients.

Servo function

As mentioned, servo filters are digital from the beginning. There is no need to modify them, except for one point. One of the filter banks contain a double pole at $z = 1$ which causes instability. Therefore, we replace the filter bank with one which has coefficients very close to the original one but does not have pole at $z = 1$. The procedure followed is similar to the other two functions.

Response function

Once we have the above functions (sensing C, actuation A, and servo D), the response function R can be calculated by $R = \frac{1+ADC}{C}$. Below is shown the comparison between the official response function R and the FIR response function R_{fir} in magnitude and phase. The relative difference is defined by $\frac{R_{fir}-R}{R}$, and the phase difference is just $\angle R_{fir} - \angle R$

The relative difference in magnitude is at most 3 %, which is very reasonable given the fact that the original response function has several percent systematic error plus a few percent statistical error. The phase discrepancy is also within acceptable levels. A thorough comparison can be found in [53].

Implementation

Now we have all the FIR filter coefficients to generate $h(t)$. There are a couple of ways to apply this filter to a data stream. We here introduce one of the most straightforward ways. Modifying figure 2.6, we get the diagram in figure 2.24. We split the DARM loop path into two, one is going backward from the DARM_ERR, the other one is the same as original. The split makes sense since the sensing function
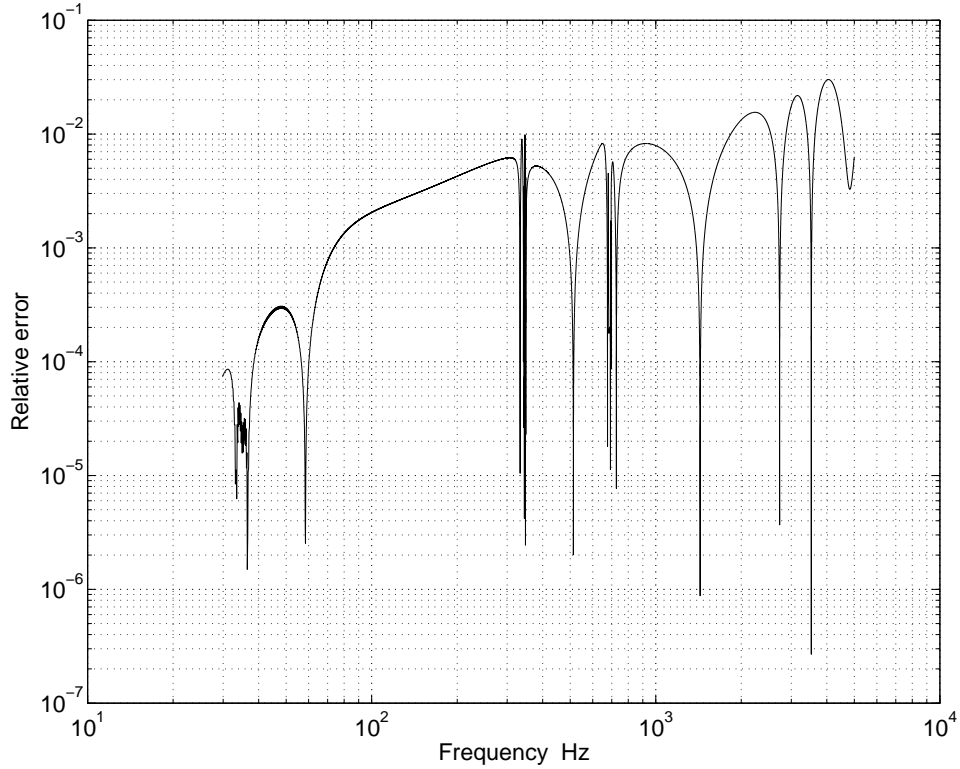
Figure 2.22: Relative difference of response function between the official function and the FIR filter.

needs to be upsampled in frequency by the FIR filter definition, while the servo and actuation function do not need the upsampling. The upsampling procedure is to place extra zeros between the original samples at 16384 Hz and smooth with a lowpass filter at a frequency lower than the Nyquist frequency. Details can be found in [54]. For validation of our h(t) production, see [53, 56].
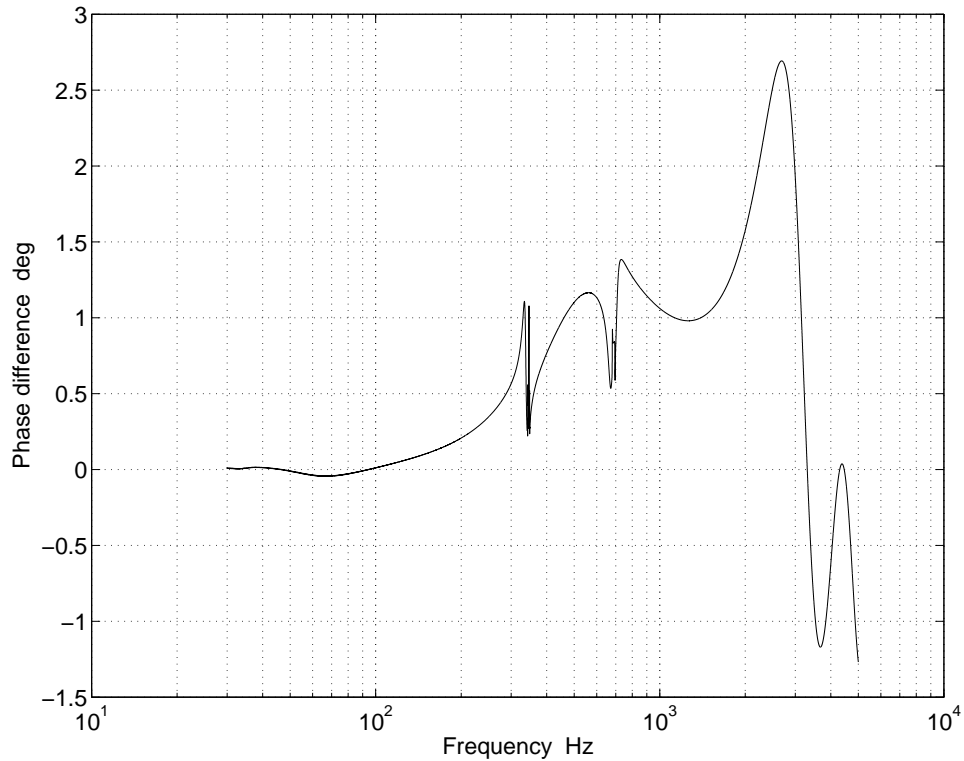
Figure 2.23: Phase difference of the response function between the official function and the FIR filter.
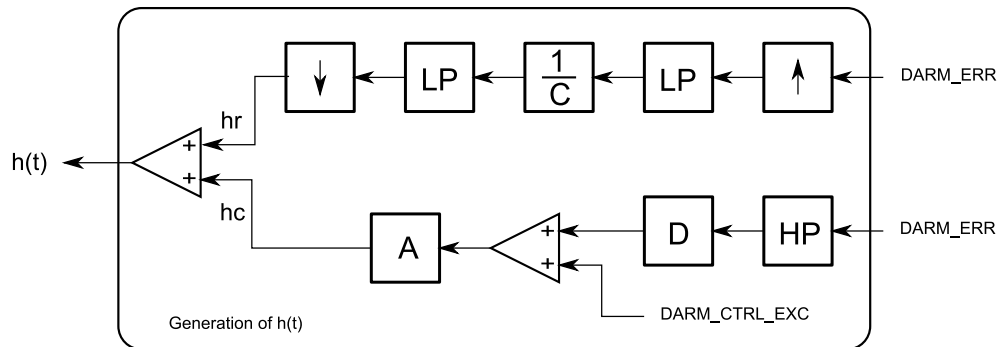
Figure 2.24: Generation of $h(t)$. $A, D, \frac{1}{C}$ are all FIR digitized filters for actuation, digital servo, and inverse of sensing described in the document. $\uparrow$ and $\downarrow$ are upsampling and downsampling, which are needed since the sensing function is designed with upsampled sampling rate. LP and HP are lowpass and highpass filters respectively. Overall multiplication to set the low frequency optical gain adjustment is omitted from the diagram.

55

Chapter 3

Alignment Sensing

3.1 Gaussian Beam

3.1.1 Hermite-Gaussian modes

Laser beams produced in most cavities are approximately described very well using Hermite-Gaussian functions [22, 23].

$$E(x, y, z, t) = e^{i\omega t} E(x, y, z) \tag{3.1.1}$$

$$E(x, y, z) = \sum_{m,n} a_{mn} U_{mn}(x, y, z) \tag{3.1.2}$$

where U_{mn} is the product of two Hermite-Gaussian functions

$$U_{mn}(x, y, z) = U_m(x, z) U_n(y, z) e^{-ikz} \tag{3.1.3}$$

$$U_m(x, z) = \left(\frac{2}{\pi}\right)^{\frac{1}{4}} \frac{1}{\sqrt{2^m m! w(z)}} H_m\left(\frac{\sqrt{2}x}{w(z)}\right)$$

$$\times \quad exp\left[-x^2\left(\frac{1}{w(z)^2} + \frac{ik}{2R(z)}\right)\right] exp\left[i\left(m + \frac{1}{2}\right)\eta(z)\right], \tag{3.1.4}$$

where $\eta(z)$, $w(z)$, $R(z)$ are the Gouy phase shift, spot size, and radius of curvature (ROC) of wave front at position z, and the beam profile is determined by these parameters completely. The Gouy phase is the phase shift with respect to that of a plane wave, the higher mode gains more Gouy phase shift as (3.1.4) indicates. The place where the ROC is infinite is called the waist and usually set as $z = 0$. The waist position is often chosen as the reference point from which the Gouy phase shift is measured.
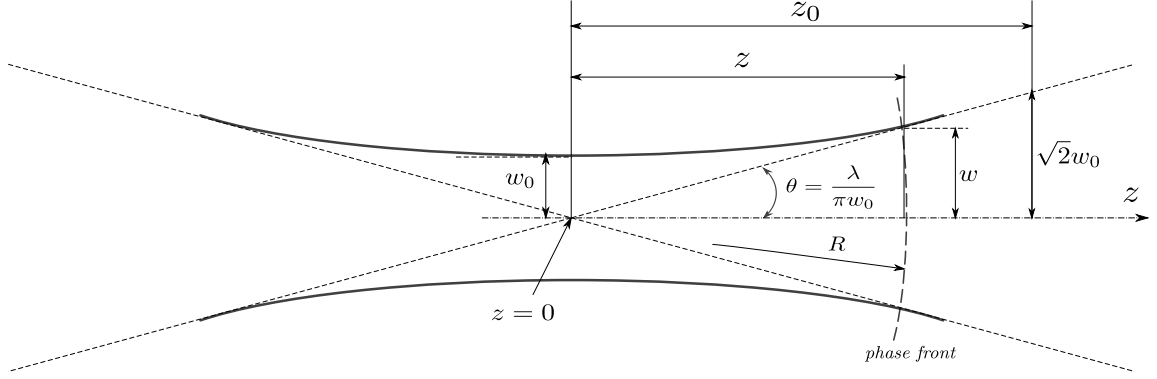
Figure 3.1: Gaussian beam parameters

$$w(z) = w_0 \left[1 + \left(\frac{z}{z_0} \right)^2 \right]^{\frac{1}{2}} \tag{3.1.5}$$

$$R(z) = z + \frac{z_0^2}{z} \tag{3.1.6}$$

$$\eta(z) = tan^{-1} \left(\frac{z}{z_0} \right) \tag{3.1.7}$$

w_0 is the waist size and z_0 is the Rayleigh range defined by

$$z_0 = \frac{\pi w_0^2}{\lambda}. \tag{3.1.8}$$

A fact that $\eta(z)$, $w(z)$, $R(z)$ are functions of distance from the waist requires accurate optical layout of an interferometer. As will be explained later, it is essential to have proper beam size and Gouy phase settings in order to get good error signal at each detection port. Figure 3.2 are some plots of $U_{mn}(x, y)$ at the waist position ($z = 0$).
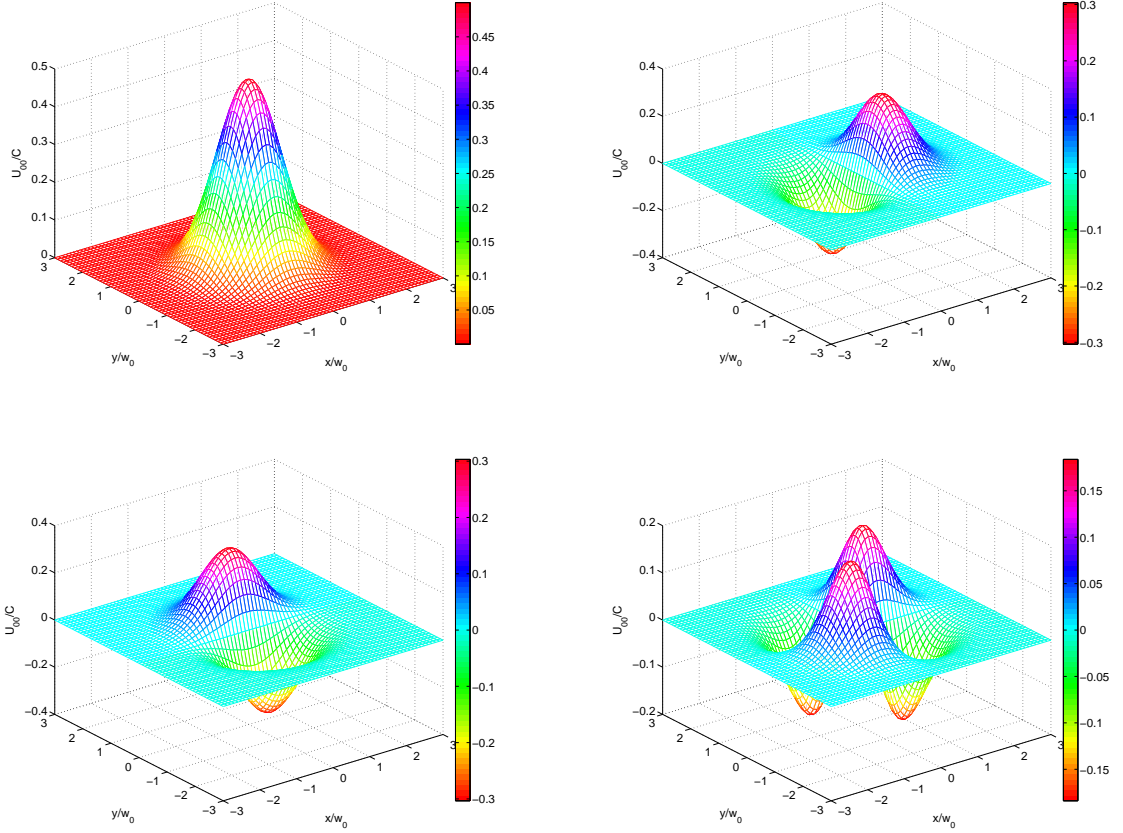
Figure 3.2: The first four U_{mn} normalized by a number $C = \sqrt{2/\pi}/w_0$. It turns out U_{10}, U_{01} can be associated with misalignment information in yaw and pitch directions. That is the heart of alignment sensing.

3.2 Modal Analysis

As we saw above, the electromagnetic field in a cavity can be described using a Hermite-Gaussian eigenmodes expansion

$$E\left(x, y, z\right) = \sum_{mn} a_{mn} U_{mn}\left(x, y, z\right), \qquad (3.2.1)$$

where a_{mn} is a vector representation in modal space. Namely, $a_{mn} = \left(a_{00}, a_{10}, a_{01}, a_{11}, ...\right)^T$. For convenience, we introduce *bra, ket* notation.

$$U_m(x, z) = |m\rangle \tag{3.2.2}$$

$$U_{mn}(x, y, z) = U_m(x, z)U_n(y, z)e^{-ikz} = |mn\rangle \tag{3.2.3}$$

Then, the orthogonality condition of the basis will be expressed as follows.

$$\int_{-\infty}^{\infty} U_m^\dagger(x, z)U_n(x, z)dx = \delta_{mn} = \sum_{mn}|m\rangle\langle n| \tag{3.2.4}$$

$$\int_{-\infty}^{\infty}\int_{-\infty}^{\infty} U_{mn}^\dagger U_{kl}dxdy = \delta_{mk}\delta_{nl} = \sum_{mn,kl}|mn\rangle\langle kl| \tag{3.2.5}$$

Now, consider a situation in which the original electromagnetic field is modified by some operator O, i.e.,

$$E'(x, y, z_2) = O(x, y, z_2, z_1)\bigotimes E(x, y, z_1) \tag{3.2.6}$$

where z_1, z_2 are the original and transformed position in z direction. The operator O includes the effect of spatial propagation and misalignment. The matrix representation of the operator will be given by

$$O_{mn,op} = \int_{-\infty}^{\infty}\int_{-\infty}^{\infty} U_{mn}^\dagger OU_{op}dxdy = \langle mn|O|op\rangle. \tag{3.2.7}$$

We simplify the operator, separating the space propagation operator from the misalignment. Namely,

$$O(x, y, z_z, z_1) = P(z_2, z_1)\bigotimes M(x, y) \tag{3.2.8}$$

where P and M are the propagation and misalignment operators respectively. P is

essentially responsible for a significant phase shift, and $M(x, y)$ is a small offset from the original phase front in transverse directions by $Z(x, y)$. The matrix representation of the propagator P will be immediately

$$P_{mn,op} = \langle mn|P(z_2, z_1)|op\rangle = \delta_{mo}\delta_{np}e^{-ik(z_2-z_1)}e^{i[(m+n+1)\eta]} \qquad (3.2.9)$$

where $\eta = \eta(z_2) - \eta(z_1)$.
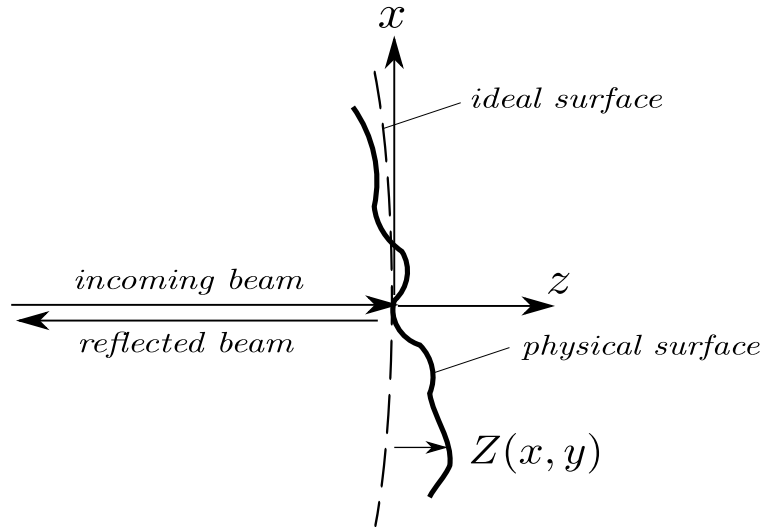
Figure 3.3: Reflection from misalinged surface. Phase shift is simplified by separating the significant phase shift from the one caused by small deviations at the mirror surface $Z(x, y)$.

For $M(x, y)$, considering the phase shift due to small deviation $Z(x, y)$,

$$M(x, y) = e^{-2ikZ(x,y)} \qquad (3.2.10)$$

where $k = \frac{2\pi}{\lambda}$ is the wave number of the laser beam. Therefore, the matrix representation of the misalignment operator will become

$$M_{mn,op} = \langle mn|e^{-2ikZ(x,y)}|op\rangle. \qquad (3.2.11)$$

For instance, if the misalignment is only in the yaw direction (around the y-axis) by a small angle θ, $Z(x, y)$ can be expressed as

$$Z(x, y) = \theta x = \frac{\lambda \Theta}{\pi w} x, \qquad (3.2.12)$$

where Θ is called the normalized angle. Using the following definite integrals $\int_{-\infty}^{\infty} e^{-x^2} dx = \sqrt{\pi}$ and $\int_{-\infty}^{\infty} x^2 e^{-x^2} = \sqrt{\pi}/2$, M will be calculated as follows (up to 1,0 mode).

$$M = e^{-\frac{1}{2}(2\Theta)^2} \begin{pmatrix} 1 & -i(2\Theta) \\ -i(2\Theta) & 1 - (2\Theta)^2 \end{pmatrix} \qquad (3.2.13)$$

$$\approx \begin{pmatrix} 1 - \frac{1}{2}(2\Theta)^2 & -i(2\Theta) \\ -i(2\Theta) & 1 - \frac{3}{2}(2\Theta)^2 \end{pmatrix} \qquad (3.2.14)$$

3.3 Detection Scheme

The Pound-Drever-Hall technique described in the previous chapter can be used to sense the misalignment of the mirrors that make up a resonant cavity [29, 30, 31]. The main differences from length sensing are the following:

♦ Firstly, we make use of the fact that misalignment causes higher-order mode excitation. The error signal is, therefore, made of beats between TEM$_{00}$, TEM$_{10}$ (yaw), and TEM$_{01}$ (pitch) of the carrier and the sidebands.

♦ The second difference is the influence of the Gouy phase. Since the Gouy phase shift is different between the fundamental mode and higher order modes, the error signal is affected by the Gouy phase in a crucial way.

3.3.1 Wave front sensing

Suppose the cavity is illuminated by the fundamental TEM$_{00}$ mode and that the cavity is on resonance and aligned as described in figure 3.4. Then, the field inside the cavity is expressed by Gaussian beam $U_{00}(x, y, z)$. Now suppose that the end mirror is tilted in the yaw direction by a small angle θ. The beam reflected from the end mirror is still TEM$_{00}$ along the new beam axis, but how does the beam look in the original axis? The answer was already given in the previous section. Specifically, using the misalignment operator $M(x, y)$, the reflected beam from the misaligned mirror can be calculated as

$$\begin{pmatrix} a'_{00} \\ a'_{10} \end{pmatrix} = \begin{pmatrix} 1 - \frac{1}{2}(2\Theta)^2 & -i(2\Theta) \\ -i(2\Theta) & 1 - \frac{3}{2}(2\Theta)^2 \end{pmatrix} \begin{pmatrix} a_{00} \\ 0 \end{pmatrix} = \begin{pmatrix} \left[1 - \frac{1}{2}(2\Theta)^2\right] a_{00} \\ -i(2\Theta) a_{00} \end{pmatrix}, \quad (3.3.1)$$

where a_{00} is the amplitude of the input beam TEM$_{00}$ mode. The point here is that the new field contains the U_{10} mode with an amplitude that is linear to the misalignment angle θ. Thus, the next question is how to extract the information from the
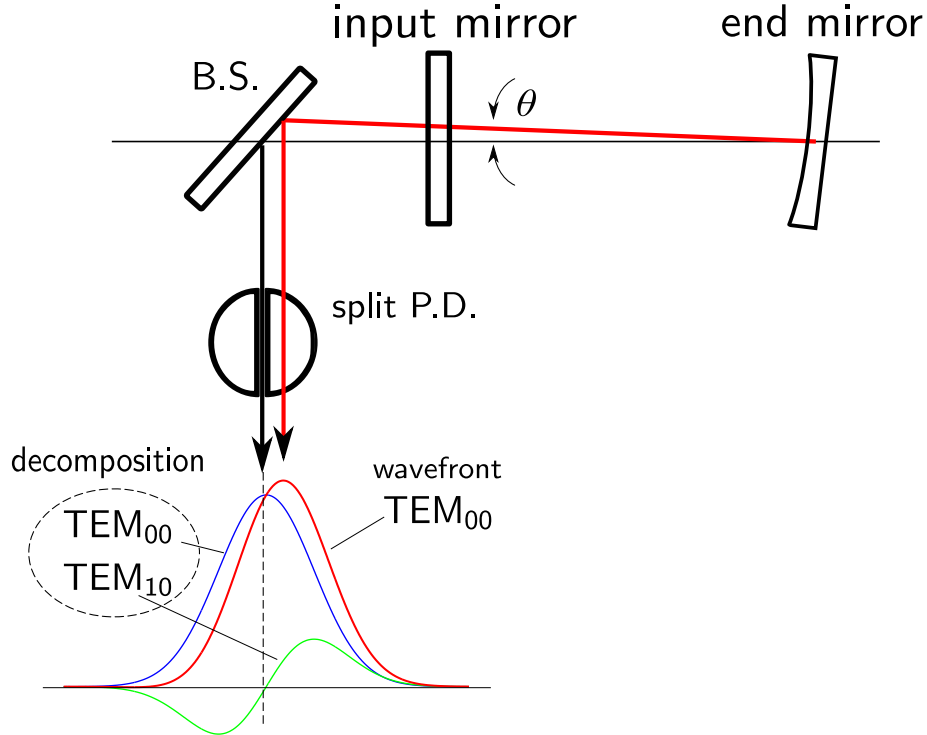
Figure 3.4: A tilted optical cavity. Reflected light from the tilted end mirror(red) can be decomposed into TEM_{00}(blue) and TEM_{10}(green) modes. The beat between the TEM_{10} mode and the directly reflected sideband(black) from the front mirror contains information about the angular tilt θ.

photodetector signal. That is the place where Pound-Drever-Hall technique comes into play. We now calculate the error signal to see how we play the game. For the simplest case, we consider only yaw motion of the end mirror, which requires two dimensions for the field.

$$E = \begin{pmatrix} a_{00} \\ a_{10} \end{pmatrix} \tag{3.3.2}$$

The operators to calculate the fields inside the cavity are similar to the one for length control. The only difference is that we need to include the misalignment operator in our description. Since we misalign the end mirror, the round trip operator will be given by

$$P_{rt} = r_1 r_2 P M_2 P, \tag{3.3.3}$$

where P, M_2 are the already derived space propagation operator and misslignment operator

$$P = e^{-ik(z_2 - z_1)} \begin{pmatrix} e^{i\eta} & 0 \\ 0 & e^{2i\eta} \end{pmatrix}, \tag{3.3.4}$$

$$M = \begin{pmatrix} 1 - \frac{1}{2}(2\theta)^2 & -2i\theta \\ -2i\theta & 1 - \frac{3}{2}(2\theta)^2 \end{pmatrix}. \tag{3.3.5}$$

Therefore, just as with length control, the field inside the cavity and that reflected from the cavity can be calculated by

$$E_{circ} = t_1(I - P_{rt})^{-1}E_{in} \tag{3.3.6}$$

$$E_{out} = r_1 E_0 - t_1 r_2 P M P E_{circ} \tag{3.3.7}$$

$$= r_1 \left[I - \frac{r_1^2 + t_1^2}{r_1^2} P_{rt} \right] (I - P_{rt})^{-1} E_{in}. \tag{3.3.8}$$

where I is the identity matrix. Since our input field is phase modulated, we can express the reflected field in the following way.

$$E_{out} = E^{CR} + E^{SB+} + E^{SB-} \tag{3.3.9}$$

The power at the output port will be, analogue to (2.1.34),

$$P = [P(\eta)E_{out}]^\dagger D^\Omega [P(\eta)E_{out}]. \tag{3.3.10}$$

$P(\eta)$ is a propagator for the Gouy phase shift to account for the phase change between

66

the cavity and the output port [1]. D^Ω is the operator for the geometric shape of the photodetector. Here, we use a split photodetector as described in figure 3.4 and it has the following form.

$$D^\Omega = \begin{pmatrix} 0 & 1 \\ 1 & 0 \end{pmatrix}.$$ (3.3.11)

Notice that we did not need D^Ω in the length sensing system since there was no need to take beats between the fundamental TEM_{00} mode and any other mode. The demodulated signal is therefore

$$S = \left(E^{CR}\right)^\dagger D^\Omega E^{SB-} + \left(E^{SB+}\right)^\dagger D^\Omega E^{CR}$$ (3.3.12)

The plot in figure 3.5 shows the field inside the cavity and also the error signal as a function of misalignment angle. As with length control, we can use the linear part around the zero-misalignment condition as an error signal for the alignment feedback.

3.3.2   ABCD matrix and beam parameters

It is someimes useful to use the *complex beam parameter* defined by

$$\frac{1}{q} = \frac{1}{R} - i\frac{\lambda}{\pi w^2},$$ (3.3.13)

where R is the radius of curvature of the phase front, w is the beam size, and λ is the wavelength. Once the parameter is given, we can propagate the parameter via the ABCD formalism as described below, which is useful even if the optical layout becomes complicated. ABCD matrices (or ray matrices) are 2×2 ray transfer matrices which tell us the path of optical rays.

---

[1]In this subsection, we ignore it assuming output port exists just in front of the cavity (looking from incoming beam side). But, as will be shown later, it is important to find the Gouy phase which gives the maximum error signal.
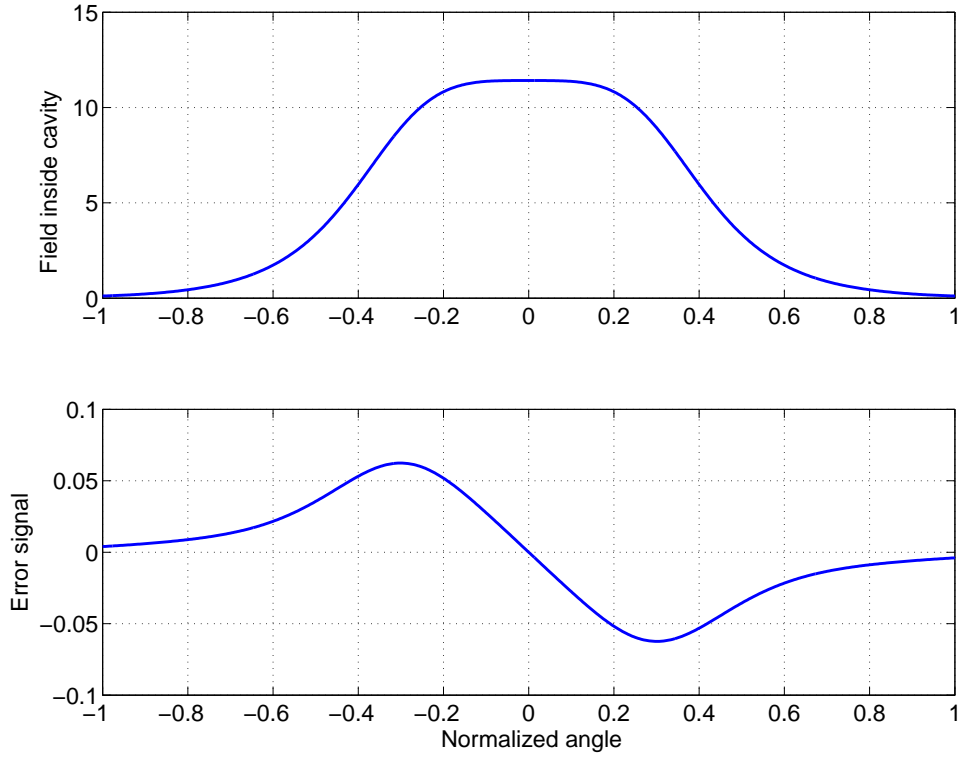
Figure 3.5: Angular error signal. The field inside the cavity (*top*) and error signal (*bottom*) as a function of misalignment angle. As with length sensing, the deflection from resonance is sensed as a linear signal of misalignment angle. All parameters from table 1.1 are used. Modulation index = 0.45.

$$\begin{pmatrix} x_2 \\ x_2' \end{pmatrix} = \begin{pmatrix} A & B \\ C & D \end{pmatrix} \begin{pmatrix} x_1 \\ x_1' \end{pmatrix} \tag{3.3.14}$$

Here, x is the displacement of a ray from the optical axis and x' is its slope. The details of ABCD matrix can be found in [22, 23]. The usefulness comes from the fact that a new beam parameter is given simply by

$$\frac{1}{q_2} = \frac{Cq_1 + D}{Aq_1 + B} \tag{3.3.15}$$

The radius of curvature and beam size are

$$R_2 = Re\left[\frac{1}{q_2}\right] \tag{3.3.16}$$

$$w_2 = \sqrt{\left[-Im\left[\frac{1}{q_2}\right]\frac{\pi}{\lambda}\right]^{-1}} \tag{3.3.17}$$

The formalism of ABCD matrices is convenient especially for complicated optical systems. For alignment sensing, it is crucial to calculate the Gouy phase and beam size accurately along the optical path. Details can be found in [49].

3.4 A matrix model of a full interferometer

Using matrices introduced in the previous section, we develop matrices representing a full interferometer [34, 35, 36, 37, 38, 39, 40, 41]. The goal in this section is to derive operator expressions for the three detection ports (anti-symmetric port, reflected port, and recycling cavity port) where the wave front sensors are located. First, consider a Fabry-Perot cavity.
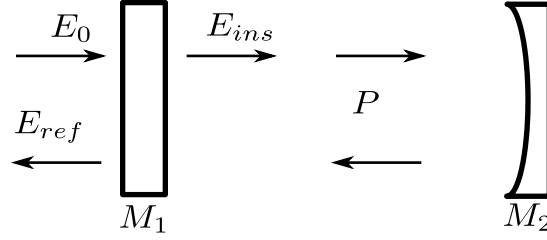
Figure 3.6: Fabry-Perot cavity.

Using the propagator, misalignment operator, reflection coefficient, and transmission coefficient, the round trip operator can be written in the following.

$$P_{rt} = (-r_1)(-r_2)M_1 P M_2 P. \tag{3.4.1}$$

We use a convention where we multiply -1 every time light is reflected from coated surface. Therefore, the field inside the cavity is

$$E_{ins} = P_{rt}E_{ins} + t_1 E_0 \tag{3.4.2}$$

$$\therefore E_{ins} = t_1(I - P_{rt})^{-1}E_0. \tag{3.4.3}$$

The reflected field is

$$
\begin{aligned}
E_{ref} &= r_1 M_1^\dagger E_0 - t_1 r_2 P M_2 P E_{ins} & (3.4.4) \\
&= r_1 M_1^\dagger \left[I - \frac{t_1^2}{r_1^2} P_{rt}(I - P_{rt})^{-1} \right] E_0 & (3.4.5) \\
&= r_1 M_1^\dagger \left[(I - P_{rt})(I - P_{rt})^{-1} - \frac{t_1^2}{r_1^2} P_{rt}(I - P_{rt})^{-1} \right] E_0 & (3.4.6) \\
\therefore E_{ref} &= r_1 M_1^\dagger \left[I - \frac{r_1^2 + t_1^2}{r_1^2} P_{rt} \right] (I - P_{rt})^{-1} E_0 & (3.4.7)
\end{aligned}
$$

The last expression is exactly what we need to have reflected light from the arm cavities (either the x-arm or the y-arm). We treat cavity as a "big" operator G. Namely,

$$
E_{1ref} = G_1 E_{1in} \tag{3.4.8}
$$

$$
E_{2ref} = G_2 E_{2in}. \tag{3.4.9}
$$

E_{1in}, E_{2in} are the electromagnetic field going into the x-arm cavity and y-arm cavity respectively, and E_{1ref}, E_{2ref} are reflected from each cavity.

The cavity operators G_1, G_2 allow us to treat each arm as a (complicated) mirror. Then, we define common Michelson and differential Michelson operators as

$$
M_C = t_6^2 P_{l_1} G_1 P_{l_1} + r_6^2 P_{l_2} G_2 P_{l_2} \tag{3.4.10}
$$

$$
M_D = r_6 t_6 (P_{l_1} G_1 P_{l_1} - P_{l_2} G_2 P_{l_2}) \tag{3.4.11}
$$

P_{l_1}, P_{l_2} are the propagation opetators for the short Michelson lengths l_1 and l_2. r_6 and t_6 are the reflection and transmission coefficients of the beam splitter. We can use M_C and M_D to get the electromagnetic field in each detection port. Next, we
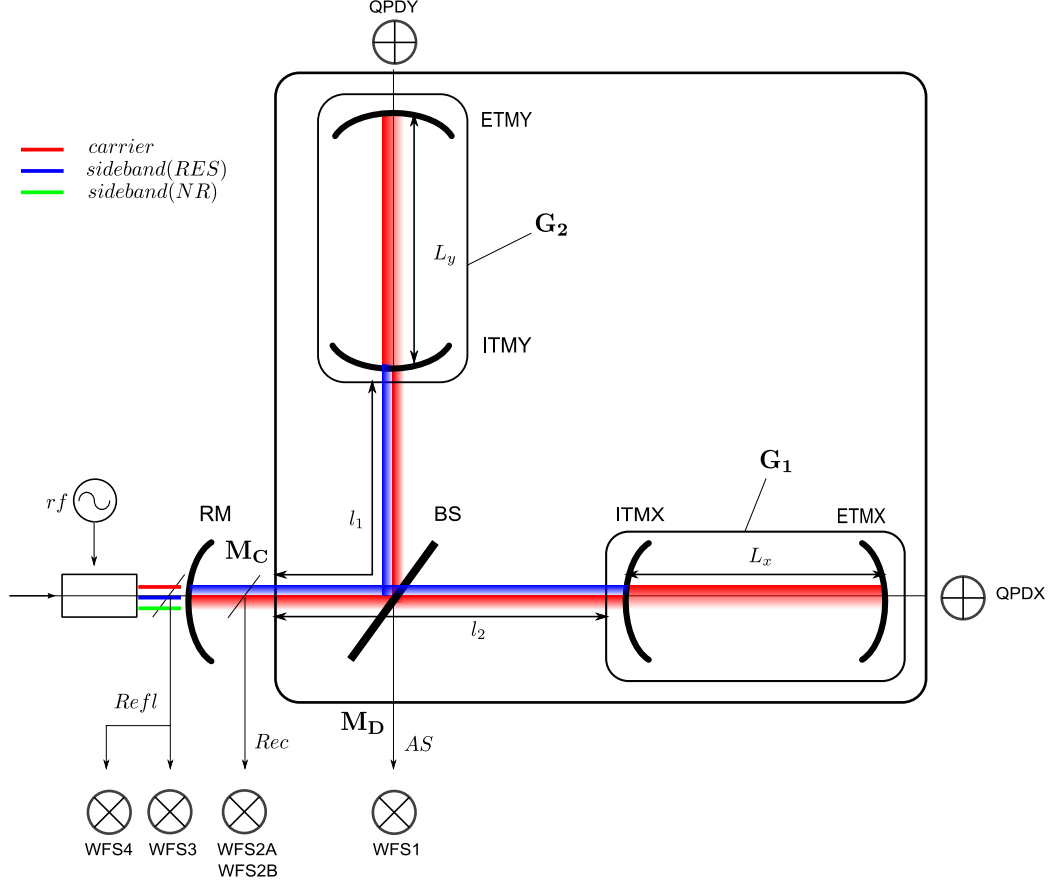
Figure 3.7: Matrices. Carrier light(red) is resonant both in the arm cavities(x and y) and the recycling cavity, while the resonant sideband(blue) is only resonant in the recycling cavity. The non-resonant sideband(green) is not resonant anywhere, but it is reflected from the recycling mirror immediately.

repeat this trick, and represent the whole Michelson interferometer consisting of the x and y arm and the beamsplitter as another (complicated) mirror, and then obtain the electric fields E_{rec}, E_{ref}, and E_{as} at the three different places such as inside the recycling cavity (rec), just outside the recycling mirror (ref), and the dark port (as), respectively.

$$
\begin{align}
E_{rec} &= t_5(I + r_5 M_5 M_C)^{-1} E_0 \tag{3.4.12} \\
E_{ref} &= r_5 M_5^\dagger (I + \frac{r_5^2 + t_5^2}{r_5} M_5 M_C)(I + r_5 M_5 M_C)^{-1} E_0 \tag{3.4.13} \\
E_{as} &= M_D E_{rec} \tag{3.4.14}
\end{align}
$$
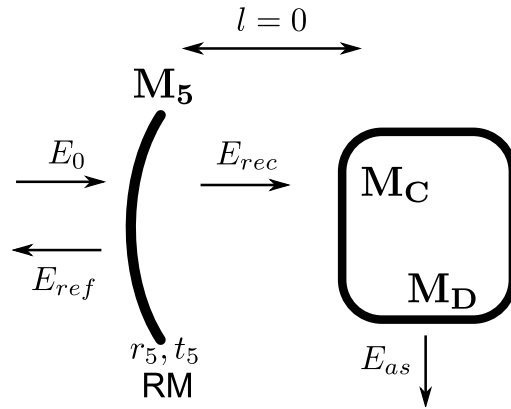
Figure 3.8: Combined matrices. We can view full interferometer in the same way as Fabry-Perot cavity is treated.

In principle, we can calculate matrices of any complicated configuration in the same manner. In the next section, we will look at error signal calculated by the formalism in this section.

3.5 Sensing Matrix

3.5.1 Theory

Now are we ready to calculate the error signals at the detection ports, such as anti-symmetric port, refl port, and pick-off port (inside the recycling cavity). The final goal is, at the three ports, to sense misalignment of the five core optics: ITMX, ITMY, ETMX, ETMY, RM, and to correct the misalignment by feedback control servos. Because of the complexity of the detector and of the Gouy phase shift along the optical path, it is not clear where we can find good sensing signals until we perform the calculation. Even when we include only first excited mode, the analytical expression at each detection port will become complicated. Then, numerical calculation is usually employed.

Of the ten alignment degrees of freedom - yaw and pitch direction for each of the five core optics, we only consider the five degrees of freedom for yaw. And, instead of using each angle, a new basis will be used as defined below.

$$
\begin{pmatrix} \Delta\theta_{ETM} \\ \Delta\theta_{ITM} \\ \overline{\theta_{ETM}} \\ \overline{\theta_{ITM}} \\ RM \end{pmatrix} = \frac{1}{\sqrt{2}} \begin{pmatrix} 0 & -1 & 0 & 1 & 0 \\ -1 & 0 & 1 & 0 & 0 \\ 0 & 1 & 0 & 1 & 0 \\ 1 & 0 & 1 & 0 & 0 \\ 0 & 0 & 0 & 0 & \sqrt{2} \end{pmatrix} \begin{pmatrix} \theta_{ITMX} \\ \theta_{ETMX} \\ \theta_{ITMY} \\ \theta_{ETMY} \\ RM \end{pmatrix} \tag{3.5.1}
$$

First, we need to have the interferometer in operating condition which is summarized below.

Making sure that the operating condition is satisfied, we introduce a misalgnment in one degree of freedom at a time and observe the demodulated signal at each port. For instance, we introduce a small angle $\Delta\theta_{ETM}$ and look at the detection signals. Since the signals depend on the Gouy phase, study of graphs like the one in figure

frequency	arm cavity	recycling cavity
CR	✓	✓
SB		✓
NR		

Table 3.1: LIGO's operating condition. CR, SB, NR are carrier, resonant sideband, and non-resonant sideband respecively. CR is resonant in both the arm cavity and recycling cavity. SB is resonant only in the recycling cavity. NR is not resonant anywhere, but it reflects immediately from recycling mirror.

3.9 allows us to find the Gouy phase that gives maximum signal.

The plot in figure 3.9 shows the demodulated signals in response to small differential misalignment in ETM. The top plot shows that the I-phase signal and the bottom plot shows Q-phase signal. Of the three detection ports, we see that the AS port is the most sensitive to this dof (dETM), and the maximum appears in the Q-phase at a Gouy phase of 90 degrees. The other plots are shown in Appendix C. Following a similar procedure, we can find a combination of the most efficient port, demodulation phase, and Gouy phase for each DOF, and this set will be our alignment sensing scheme.

In order to sense ten degrees of freedom, four quadrant photodetectors have been used in LIGO. They are WFS1, WFS2, WFS3, and WFS4. WFS1 is at the anti-symmetric port and is the most sensitive to dETM and dITM. WFS2 picks up the signal from the recycling cavity port and it works as two different sensors by demodulation phase. The Q-phase is called WFS2B, and it senses dITM, while the I-phase is called WFS2A and it measures cITM and RM DOFs. WFS3 and WFS4 are placed in the reflected port and they get the same light, but in different Gouy phases. WFS4 senses the common mode degrees of freedom, cITM and cETM, while WFS3 is sensitive to RM. These are summarized in figure 3.10, which is a copy from [34].

3.5.2   Measured sensing matrix

This subsection describes how the sensing matrix is measured in reality. The previous subsection described the theory, in which everything is perfectly aligned but one dof
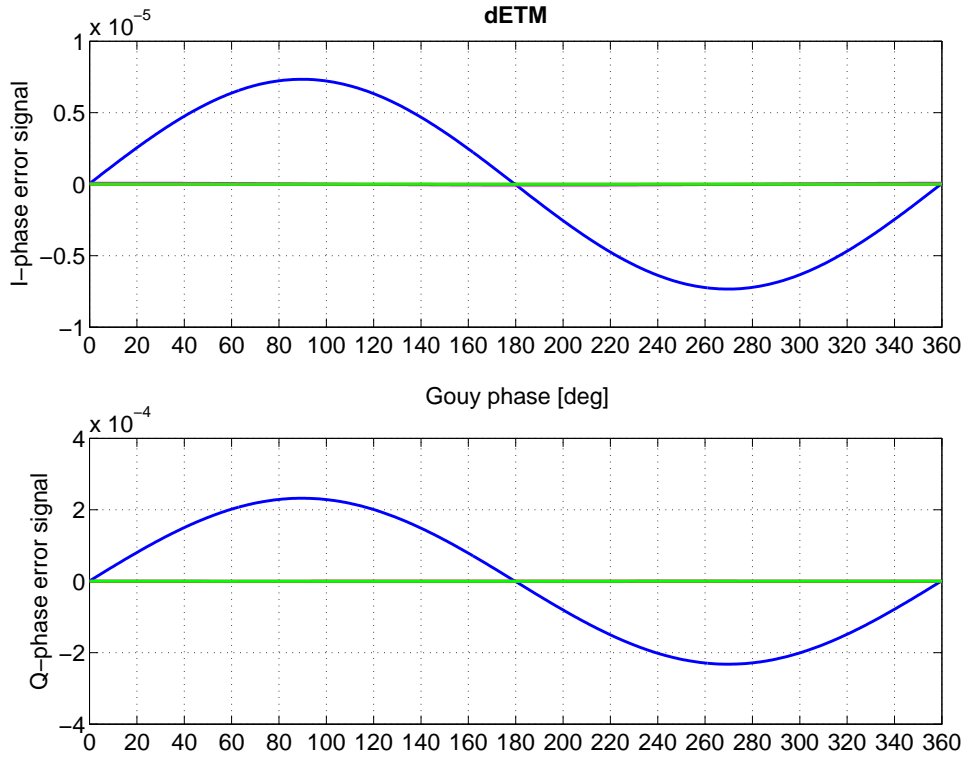
Figure 3.9: Error signals to dETM at detection ports as a function of the Gouy phase. The color scheme is as follows. *blue*:antisymmetric port, *magenta*:refl, *green*:pick-off, *red*:refl(NR).

Table 2. Alignment Sensing Parameters Defined in Eq. 16 for Each Sensing Port[a]

Sensing Port	Angular Degree of Freedom				
	$\triangle$ETM	$\triangle$ITM	$\overline{\text{ETM}}$	$\overline{\text{ITM}}$	RM
Antisymmetric	25 Q 90°	11 Q 90°	9.9×10^{-6} Q 156°	4.5×10^{6} Q 156°	1.2×10^{3} Q 90°
Reflected	2.3×10^{2} Q 144°	1.4 Q 144°	0.73 I 97°	6.2 I 146°	9.6 I 146°
Recycling cavity	1.8×10^{3} Q 144°	0.11 Q 144°	1.4×10^{2} I 61°	0.52 I 143°	0.72 I 144°
Reflected NR sidebands	1.5×10^{4} I 148°	1.7×10^{3} Q 0°	2.1 I 90°	0.97 I 90°	1.9 I 0°

[a]For each angular degree of freedom, the top number listed is A_i (in watts, with significant values in boldface); below left is the RF phase ϕ_{D_i}, in phase I or in quadrature Q with the modulation phase at the input, and below right is the Gouy phase angle η_i. The last row lists the signals produced with phase-modulation sidebands that are not resonant (NR sideband) in the interferometer.

Figure 3.10: The table from [34]. A table by which initial LIGO's angular sensing and control (ASC) scheme was initially designed. Boxes are added to show which photodetector covers which DOF.

to which we introduce misalignment. In reality, the interferometer is under the influence of various noise such as seismic noise, thermal noise, shot noise etc, and each mirror is controlled to satisfy the running condition. Given that the natural frequency of the angular mode (either yaw or pitch) of the mirror suspension is around 0.5 Hz, the most influential noise will be seismic noise. It is impossible to measure the sensing matrix, completely equivalent to what we have in the theory where everything is static. So we take, instead, the transfer function from exciting each mirror at a certain frequency 9.7Hz [44]. If one mirror is shaken, everything will start responding to the fluctuation due to feedback control loops - everything is coupled in reality. Then, we use a *notch filter* which passes all frequencies except for 9.7 Hz. We activated the filters related to angular control, which allows us to see the WFS's *uncontrolled*[2] signals in response to each mirror's excitation at 9.7Hz, while allowing the angular control servos to keep the interferometer aligned. The assumption here is that the relative response of each WFS will be the same at lower frequencies - around 0.5 Hz. The excitation signal at 9.7 Hz is injected into the control path to each mirror (the five core optics, plus BS and MMT3) [3] one at a time, and record the transfer function of WFS signals (WFS1, WFS2, WFS3, WFS4), QPDX, and QPDY.

The table shows response of photodetectors to each mirror excitation in counts per micro radian [45]. For instance, when ETMX is excited by one micro radian, WFS1 senses the motion by 169079.631 cts and the relative phase difference to the excitation motion is -3.121532 radian. Some of these values will be used in the model we developed for understanding of angular instability (see chapter 4). Values for the pitch direction are acquired in the same manner. As we see, if we excite one mirror, all photodetectors sense the excitation. In other words, everything is coupled here

---

[2]We want each WFS's response when a misalignment is introduced in a mirror, which is the situation we have in the theory. The situation can be called *uncontrolled*, since if ASC system senses the misalignment in reality, all optics immediately respond to fix the misalignment. We need to cut off the control to measure sensing matrix, but need the IFO in the operating condition. That is why we need the notch filter to make the system *uncontrolled* at 9.7Hz.

[3]BS and MMT3 are controlled for beam centering of the laser beam. Quadrant photodiodes called QPDX, QPDY are located behind end mirrors (ETMX, ETMY) to sense beam centering and the signal is fed back to BS and MMT3.

WFS	ETMX	ETMY	ITMX	ITMY	RM	BS	MMT3
WFS1	169079.631	131788.0265	-51572.22852	-55658.32425	6642.757075	-813.8707905	2520.927769
	(-3.121532)	(-3.12098)	(3.168657)	(3.163367)	(-0.13606)	(-3.112959)	(-0.314514)
WFS2A	3300.800189	144.3731638	-27364.04886	-20897.09309	156612.4084	-71214.44234	5219.263222
	(-3.070222)	(0.1379)	(0.022006)	(3.171583)	(-0.00586)	(0.020085)	(-0.185835)
WFS2B	722.1845287	298.2350085	-8228.773865	-15452.7151	76653.71285	-52745.26995	2422.408771
	(-2.953122)	(0.00891)	(0.004467)	(3.164843)	(-0.01646)	(0.009492)	(-0.080297)
WFS3	2961.088764	1657.873538	-10350.24362	-7797.50872	93092.46622	-24248.55425	60825.90474
	(-0.025724)	(-3.13538)	(-0.040866)	(3.166531)	(-0.00616)	(0.018053)	(3.132466)
WFS4	9759.176994	7474.121764	-1812.04814	-1929.186009	25890.10953	-4953.629098	25325.76183
	(0.015053)	(-3.12392)	(0.2162715)	(3.178285)	(3.126379)	(-3.140449)	(-0.018053)
QPDX	1046.681723	10.35131097	-1182.245404	-5.012753643	34.72445802	-8.257156132	11.80078105
	(0.013721)	(-0.32177)	(0.022899)	(5.03053)	(2.550526)	(1.981451)	(-2.596754)
QPDY	18.11150978	725.3134442	-10.50703441	-1103.853674	9.690568406	-21.18291435	42.43329428
	(-0.4296799)	(-3.10841)	(-0.76179)	(3.170551)	(4.34081)	(-2.379739)	(-1.578234)

Table 3.2: Measured sensing matrix which is extracted from a file yawH1_051206_1823.txt: transfer function to excitation of each mirror. The unit is counts per microradian calibrated by optical lever [43], and numbers in the bracket are phase relative to the excitation, in radian.

to some extent. Feedback gains are calculated by taking the inverse of the sensing matrix with some truncation based on the significance of each component [46]. The matrix is called the output matrix. Table 3.3 is an output matrix determined by commissioners at some point during S5.

	WFS1	WFS2A	WFS2B	WFS3	WFS4	QPDX	QPDY
ETMX	0.946	0.800	-0.466	-0.605	-0.952	0.330	
ETMY	1.054	-0.880	-0.520	0.667	1.048		-0.200
ITMX		0.952	-0.830	-0.640	0.165	4.560	
ITMY		-1.048	-1.170	0.740	-0.181		-2.160
RM		0.365		-1.00	0.153	0.370	
BS						0.100	-0.100
MMT3						1.00	

Table 3.3: Output matrix in S5. It defines how feedback takes place after sensing misalignment angle via the wave front sensors. Essentially, it is the inverse of the sensing matrix, but some components are truncated based on significance of the signals.

In table 3.3, we can see the basis is fit to differential and common motion. For example, the WFS1 is fed back to the ETMX and ETMY by a feedback gain 0.946, 1.054 respectively. As discribed already, the WFS1 is responsible for differential angle change $d\theta_{ETM} = \theta_{ETMX} - \theta_{ETMY}$. So, all signs in the table seem flipped here (i.e., the common motion has different sign while differential mode has the same sign.). In

this way, we determine the output matrix to control misalignment of each mirror. It is essentially the inverse of the sensing matrix. In the next chapter, we will discuss the effect of radiation pressure on the ASC system.

Chapter 4

Angular Instability

4.1 Sigg-Sidles instability

As the laser power that is stored in an optical resonator like a LIGO arm cavity becomes larger, so does the radiation pressure or photon recoil force exerted on the mirrors. This force is resisted by the mechanical restoring force of the mirror suspension. In the context of LIGO-like cavities, such a coupling to longitudinal motion of the mirrors has been experimentally demonstrated by Nergis Mavalvala et. al [43].

In this chapter, we describe a measurement of an instability coupling of the radiation pressure to the angle of the mirrors, which was first theoretically predicted by D. Sigg and J. Sidles [32]. They studied the angular instability in an optical resonator caused by radiation pressure; this might be a problem at high power operation in future gravitational wave detectors [32][33]. The physics of the problem can be described as follows. Let's consider an optical resonator described in the figure below.
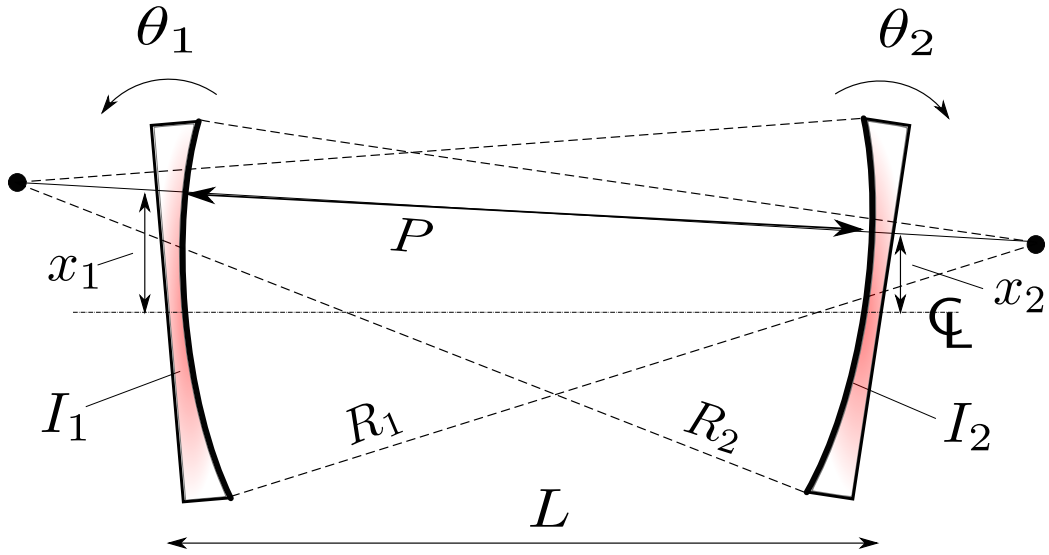
Figure 4.1: Tilted Optical Resonator. Two mirrors are coupled by radiation pressure caused by the power of the laser beam P, pushing at distance x_1 and x_2 away from the center line when tilted angles are θ_1, θ_2 respectively. I_1, I_2 are moment of inertia of the mirrors. R_1, R_2, L are radius of curvature of the mirrors and distance between the mirrors respectively. The sketch can be viewed as either yaw or pitch motion.

The sketch shows two tilted coated mirrors whose moment of inertia are I_1, I_2 with

very large radius of curvature R_1, R_2 (larger than distance between two mirrors in LIGO), optical axis defined by a line connecting centers of curvature of the mirrors. The sketch can be viewed either as yaw motion or pitch direction. The angles of the mirror θ_1, θ_2 are defined as sketched. The two mirrors have a mechanical restoring force from the wire loop holding them onto the suspension system. The force is proportional to the small angle measured from equilibrium position, for which we use a spring constant of torsion pendulum μ_1 and μ_2. Due to high reflectivity of the mirror, when the optical resonant condition is satisfied, the force due to laser power $\frac{2P}{c}$ will become recognizable, where P is the laser power and c is the speed of light. And, if pointing of the laser beam is off-centered, the mirror will experience torque due to the radiation pressure

$$\tau_1 = \frac{2Px_1}{c} \tag{4.1.1}$$

$$\tau_2 = \frac{2Px_2}{c}, \tag{4.1.2}$$

where x_1 and x_2 are the distance of the beam spot from the center of the mirror.

With no light, each mirror can exhibit torsional oscillations independent of the other arm. When the cavity is filled with light, there are two coupled modes in the opto-mechanical system.

Suppose that both mirrors tilt in such a way that the ray axis runs across the center line [1]. In this situation, radiation pressure works so as to enhance the restoring force from the wire which pushes the mirrors back to the original angles. This is sometimes called an "auto-alignment mechanism". It is a stable mode. If the tilt angle becomes larger, the beam spot will move outward and the torque due to radiation pressure will become larger, which means mirrors experience bigger restoring torque to reduce the

---

[1] The figure 4.2 and figure 4.3 are the projections to a plane perpendicular to the mirror rotation axis. We are only considering either yaw motion or pitch motion in the sketches.

angle. The eigenfrequency of this mode will be bigger than the original uncoupled pendulum natural frequency, since the net spring constant is bigger than the original.
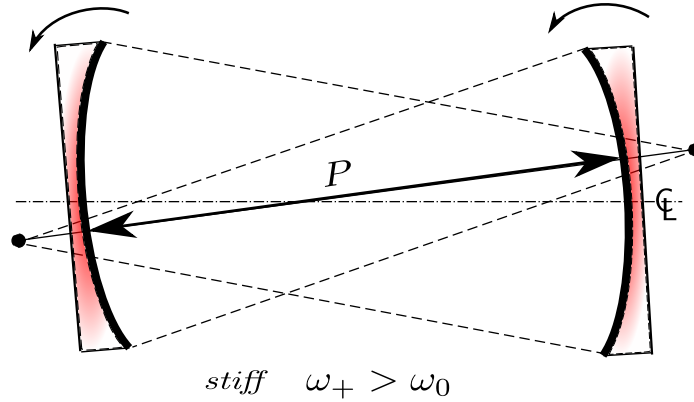
$$stiff \quad \omega_+ > \omega_0$$

Figure 4.2: Stiff mode of angular motion in optical resonator. Radiation pressure works to enhance the mechanical restoring force, resulting in auto-alignment. The larger tilt, the bigger torque due to radiation pressure to enhance restoring force.

On the other hand, suppose that both mirrors tilt in such a way that the ray axis does not run across the center line. In that situation, the radiation pressure works against the restoring force from the wire.

$$soft \quad \omega_- < \omega_0$$
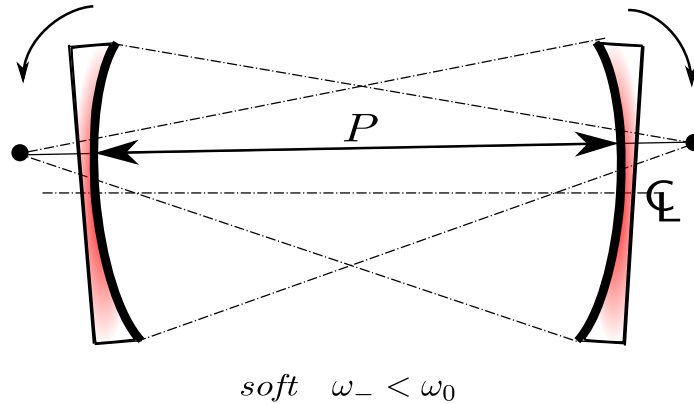
Figure 4.3: Soft mode of angular motion in optical resonator. Radiation pressure works against restoring force from wire, and if power exceeds a critical value, laser light will walk off from the cavity.

So, if the tilt angle becomes larger, the beam spot will move outward and the torque will become larger, which means the net restoring force will become smaller. When the power inside the optical resonator reaches a critical value, the net restoring force

will become zero, or negative - i.e., not a restoring force any more. Above the critical power, the mode is unstable, since once the system is in the situation, the beam spots will walk away from the cavity.

In order to discuss the above quantitatively, we will consider the equations of motion of the system. Kinetic energy K and potential V of the system are as follows.

$$K = \frac{1}{2}I_1\dot{\theta_1}^2 + \frac{1}{2}I_2\dot{\theta_2}^2 \tag{4.1.3}$$

$$V = \frac{1}{2}\mu_1\theta_1^2 + \frac{1}{2}\mu_2\theta_2^2 - \int \tau_1 d\theta_1 - \int \tau_2 d\theta_2 \tag{4.1.4}$$

The relation between θ and x are given by the following geometrical relations [23].

$$x_1 = \frac{g_2}{1 - g_1 g_2} L\theta_1 + \frac{1}{1 - g_1 g_2} L\theta_2 \tag{4.1.5}$$

$$x_2 = \frac{1}{1 - g_1 g_2} L\theta_1 + \frac{g_1}{1 - g_1 g_2} L\theta_2, \tag{4.1.6}$$

where g_1 and g_2 are so-called *g-parameters*

$$g_1 = 1 - \frac{L}{R_1} \tag{4.1.7}$$

$$g_2 = 1 - \frac{L}{R_2} \tag{4.1.8}$$

Therefore, the potential energy terms due to torque can be rewritten as follows.

$$\int \tau_1 d\theta_1 = \frac{2P}{c} \int d\theta_1 \left(\frac{g_2}{1 - g_1 g_2} L\theta_1 + \frac{1}{1 - g_1 g_2} L\theta_2 \right)$$

$$\int \tau_2 d\theta_2 = \frac{2P}{c} \int d\theta_2 \left(\frac{1}{1 - g_1 g_2} L\theta_1 + \frac{g_1}{1 - g_1 g_2} L\theta_2 \right)$$

$$\therefore$$

$$\int \tau_1 d\theta_1 + \int \tau_2 d\theta_2$$

$$= \frac{PL}{c} \left(\frac{g_2}{1 - g_1 g_2} \theta_1^2 + \frac{g_1}{1 - g_1 g_2} \theta_2^2 + \frac{2}{1 - g_1 g_2} \theta_1 \theta_2 \right) \qquad (4.1.9)$$

The Lagrangian of the system is, therefore

$$\mathcal{L} = \frac{1}{2} I_1 \dot{\theta_1}^2 + \frac{1}{2} I_2 \dot{\theta_2}^2 - \frac{1}{2} \mu_1 \theta_1^2 - \frac{1}{2} \mu_2 \theta_2^2 +$$

$$\frac{PL}{c} \left[\frac{g_2}{1 - g_1 g_2} \theta_1^2 + \frac{g_1}{1 - g_1 g_2} \theta_2^2 + \frac{2}{1 - g_1 g_2} \theta_1 \theta_2 \right]. \qquad (4.1.10)$$

The first line is for the mechanical aspect of the two mirrors, and the second line is radiation pressure effect from the laser inside the optical resonator. The equations of motion of the system are,

$$I_1 \ddot{\theta_1} + \left(\mu_1 - \frac{2PL}{c} \frac{g_2}{1 - g_1 g_2} \right) \theta_1 - \frac{2PL}{c} \frac{1}{1 - g_1 g_2} \theta_2 = 0 \qquad (4.1.11)$$

$$I_2 \ddot{\theta_2} + \left(\mu_2 - \frac{2PL}{c} \frac{g_1}{1 - g_1 g_2} \right) \theta_2 - \frac{2PL}{c} \frac{1}{1 - g_1 g_2} \theta_1 = 0. \qquad (4.1.12)$$

Now, we consider small oscillations around the equilibrium position, denoting the kinetic energy term and potential energy term as $K = \frac{1}{2} K_{ij} \dot{\theta_i} \dot{\theta_j}$, $V = \frac{1}{2} V_{ij} \theta_i \theta_j$ respectively $(i, j = 1, 2)$.

$$K_{ij} = \begin{pmatrix} I_1 & 0 \\ 0 & I_2 \end{pmatrix} \qquad (4.1.13)$$

$$V_{ij} = \begin{pmatrix} \mu_1 - \frac{2PL}{c}\frac{g_2}{1-g_1 g_2} & -\frac{2PL}{c}\frac{1}{1-g_1 g_2} \\ -\frac{2PL}{c}\frac{1}{1-g_1 g_2} & \mu_2 - \frac{2PL}{c}\frac{g_1}{1-g_1 g_2} \end{pmatrix}. \tag{4.1.14}$$

In order to find the eigenfrequencies ω of the system, we solve $det\,(V - \omega^2 K) = 0$. Namely,

$$\begin{vmatrix} \mu_1 - \frac{2PL}{c}\frac{g_2}{1-g_1 g_2} - \omega^2 I_1 & -\frac{2PL}{c}\frac{1}{1-g_1 g_2} \\ -\frac{2PL}{c}\frac{1}{1-g_1 g_2} & \mu_2 - \frac{2PL}{c}\frac{g_1}{1-g_1 g_2} - \omega^2 I_2 \end{vmatrix} = 0. \tag{4.1.15}$$

After some calculations, we get the following characteristic equation.

$$I_1 I_2 \omega^4 - I_1\left(\mu_2 - \frac{2PL}{c}\frac{g_1}{1-g_1 g_2}\right)\omega^2 - I_2\left(\mu_1 - \frac{2PL}{c}\frac{g_2}{1-g_1 g_2}\right)\omega^2$$
$$+\left(\mu_2 - \frac{2PL}{c}\frac{g_1}{1-g_1 g_2}\right)\left(\mu_1 - \frac{2PL}{c}\frac{g_2}{1-g_1 g_2}\right) - \frac{4P^2}{c^2}\left(\frac{L}{1-g_1 g_2}\right)^2 = 0 \tag{4.1.16}$$

In the following discussion, we assume $I_1 = I_2 = I$, and $\mu_1 = \mu_2 = \mu$, which is reasonable approximation for LIGO. The above equation will be, therefore

$$I^2\omega^4 - 2I\left(\mu - \frac{PL}{c}\frac{g_1 + g_2}{1-g_1 g_2}\right)\omega^2$$
$$+ \left(\mu^2 - \frac{2PL}{c}\frac{g_1 + g_2}{1-g_1 g_2}\mu - \frac{4P^2 L^2}{c^2}\frac{1}{1-g_1 g_2}\right) = 0. \tag{4.1.17}$$

This will give two eigenfrequencies as follows.

$$\omega_{\pm}^2 = \omega_0^2 + \frac{PL}{Ic}\left[\frac{-(g_1 + g_2) \pm \sqrt{4 + (g_1 - g_2)^2}}{1-g_1 g_2}\right], \tag{4.1.18}$$

where ω_0 is the normal angular frequency of a torsion pendulum.

$$\omega_0 = \sqrt{\frac{\mu}{I}} \qquad (4.1.19)$$

ω_+ goes up as P goes up, while ω_- goes down. Therefore, ω_- will hit zero at some laser power. We name the mode corresponding to ω_+ as *stiff*, and the mode corresponding to ω_- as *soft*. The eigenvectors for these eigenfrequencies are

$$\vec{\theta_+} = \begin{pmatrix} \frac{2}{1-g_1g_2} \\ \frac{g_1-g_2-\sqrt{4+(g_1-g_2)^2}}{1-g_1g_2} \end{pmatrix} \qquad (4.1.20)$$

$$\vec{\theta_-} = \begin{pmatrix} \frac{2}{1-g_1g_2} \\ \frac{g_1-g_2+\sqrt{4+(g_1-g_2)^2}}{1-g_1g_2} \end{pmatrix}. \qquad (4.1.21)$$

These eigenvectors correspond to figure 4.2 and figure 4.3, respectively.

In order to investigate the system's behavior, we apply a sinusoidal external torque $Tcos\omega t$ to one of the mirrors and observe the response of the mirror, where T is the amplitude of the torque, ω is the angular frequency of the excitation. Modifying (4.1.12), the system's equations of motion now will become as follows[2]

$$I_1\ddot{\theta}_1 + \left(\mu_1 - \frac{2PL}{c}\frac{g_2}{1-g_1g_2}\right)\theta_1 - \frac{2PL}{c}\frac{1}{1-g_1g_2}\theta_2 = 0 \qquad (4.1.22)$$

$$I_2\ddot{\theta}_2 + \left(\mu_2 - \frac{2PL}{c}\frac{g_1}{1-g_1g_2}\right)\theta_2 - \frac{2PL}{c}\frac{1}{1-g_1g_2}\theta_1 = Tcos\omega t. \qquad (4.1.23)$$

From now on, we denote 1 and 2 to express ITM and ETM. So, we apply an external torque to the ETM in this case. Letting θ_1, θ_2 as follows, we will determine the coefficients .

---

[2]The first equation is identical to (4.1.12).

$$\theta_1 = A cos\omega t + B sin\omega t \tag{4.1.24}$$

$$\theta_2 = C cos\omega t + D sin\omega t \tag{4.1.25}$$

The straightforward calculation gives

$$\frac{A}{T} = \frac{\alpha}{I^2 \left(\omega^2 - \omega_+^2\right)\left(\omega^2 - \omega_-^2\right)} \tag{4.1.26}$$

$$\frac{C}{T} = \frac{\left(\omega^2 - \omega_z^2\right)}{I \left(\omega^2 - \omega_+^2\right)\left(\omega^2 - \omega_-^2\right)} \tag{4.1.27}$$

$$B = D = 0 \tag{4.1.28}$$

where

$$\omega_\pm^2 = \omega_0^2 + \frac{PL}{Ic}\left[\frac{-\left(g_1 + g_2\right) \pm \sqrt{4 + \left(g_1 - g_2\right)^2}}{1 - g_1 g_2}\right] \tag{4.1.29}$$

$$\omega_z^2 = \omega_0^2 - \frac{2PL}{cI}\frac{g_2}{1 - g_1 g_2} \tag{4.1.30}$$

$$\alpha = \frac{2PL}{c}\frac{1}{1 - g_1 g_2}. \tag{4.1.31}$$

As we expect, (4.1.29) is identical to (4.1.18). In the following, we will look into the transfer function $\frac{C}{T}$, which is the transfer function of the mirror-angle to the torque applied to the mirror. Or, redefining it in the Laplace domain (s-domain),

$$H(s) = \frac{-\left(s^2 + \omega_z^2\right)}{\left(s^2 + \omega_-^2\right)\left(s^2 + \omega_+^2\right)}. \tag{4.1.32}$$

Two pairs of poles $\omega_\pm$ correspond to the previous eigenfrequencies of the system and ω_z is a pair of zeros. As shown in figure 4.4, ω_+ increases as P goes up, while ω_- and ω_z decrease as P goes up. Then, both ω_- and ω_z will eventually hit zero and become imaginary numbers. The corresponding poles and zeros become real. Bode di-

agrams and a pole map of (4.1.32) are shown in Figure 4.5 and Figure 4.6 respectively.
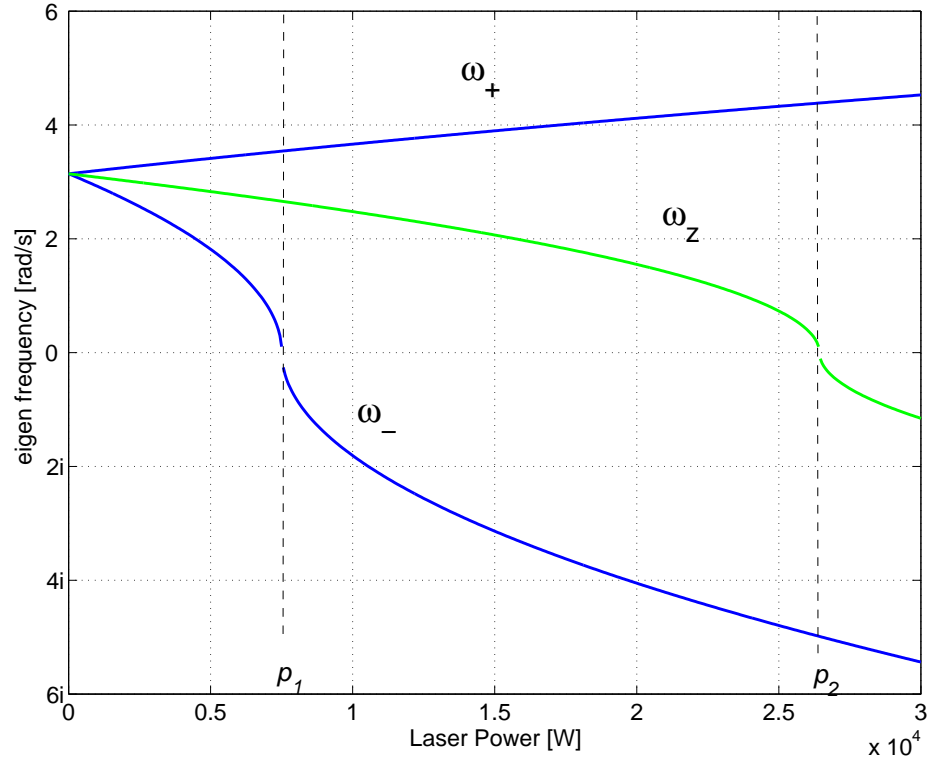

Figure 4.4: How angular frequency of poles and zeros moves according to cavity laser power.

When $P = 0$, the two mirrors are un-coupled. So, the transfer function will be that for a simple torsion pendulum. When P is smaller than P_1, the two mirrors will be coupled and the Bode diagram will have two peaks associated with the two pairs of poles and one dip from the pair of zeros. In the *s-plane*, a pair of poles can be seen as ones going away from $s = \pm i\omega_0$ (triangles in the fugure 4.6). When P becomes larger than P_1, ω_- will become negative, which means one of the two pairs of poles will become real. At that point, a peak corresponding to ω_- in the Bode diagram will disappear. In the *s-plane*, the pair hit the origin, then move away from it on the real axis. When P reaches P_2 (above which a pair of zeros become imaginary), the dip corresponding to ω_z will disappear from the Bode diagram. The
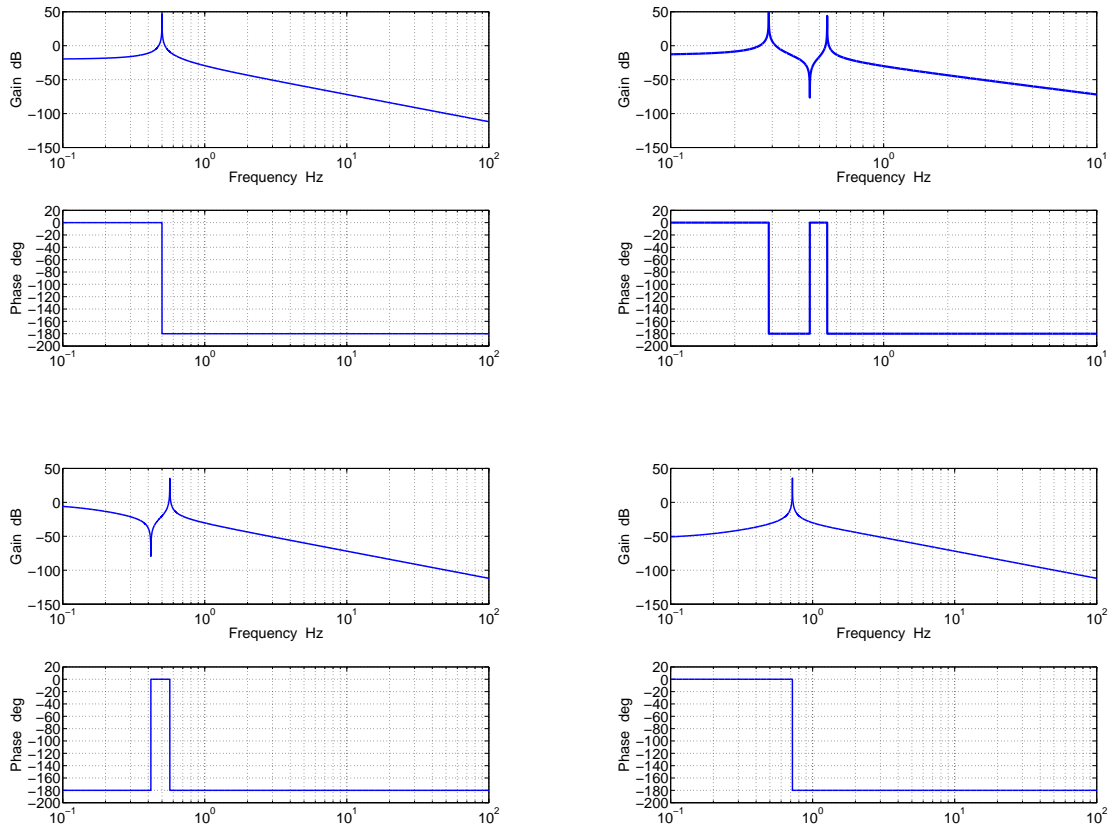
90

Figure 4.5: Bode plot of two-mirror system in various powers., *Top left $P = 0$, top right $0 < P < P_1$, bottom left $P_1 < P < P_2$, bottom right $P_2 < P$*

circles in the *s-plane* are the poles at the operating laser power in iLIGO. Poles in the right half plane indicate instability. Physically, it means when $p > P_1$, in a mode corresponding to ω_-, torque due to radiation pressure overtakes restoring torque of pendulum. Therefore, iLIGO would be unstable without angular control. In the next section, we introduce experiment performed in the 4-km LIGO interferometer in Hanford Observatory (LHO), WA.

4.2 Measurement

The angular sensing and control system (ASC) has ten degrees of freedom (DOF). They are the pitch and yaw motion of the five core optics (The two pair of mirrors in the Fabry-Perot cavities and the recycling mirror located upstream of the Michel-
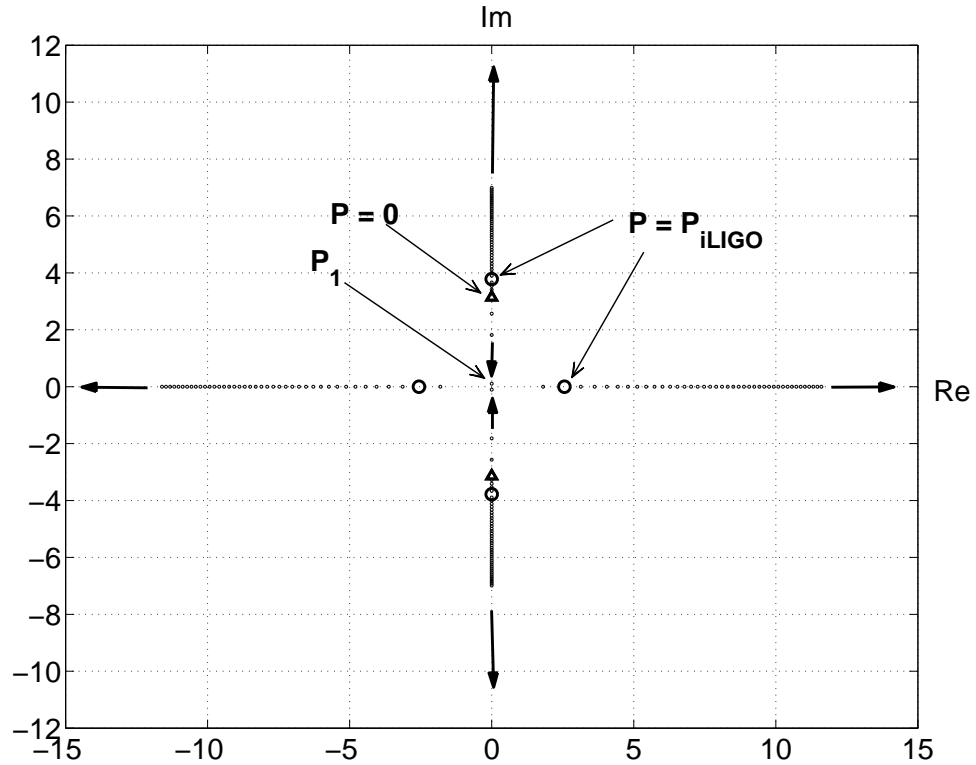
Figure 4.6: Pole movement in *s-plane* at various powers.

son interferometer). These DOFs are measured by quadrant photo detectors called wave front sensors (WFS) and controlled by electromagnetic actuators attached to the mirror surface. The principles of how the WFS works were already described in the previous chapter. We reduce the ten degrees of freedom to two by looking at only two WFSs which are sensitive to the differential degrees of freedom.

Besides these WFSs for global angular sensing, there are sensors called *optical levers* [48], which work only locally. An optical lever consists of a diode laser and a quadrant photodiode which senses the position of the laser spot reflected by the mirror, and thus allows a measurement of the angle of the mirror. We use the optical lever signal to monitor the response of the mirrors to angular excitation since that is the transfer function $H(i\omega)$ we investigated in the previous subsection. As we mentioned in the
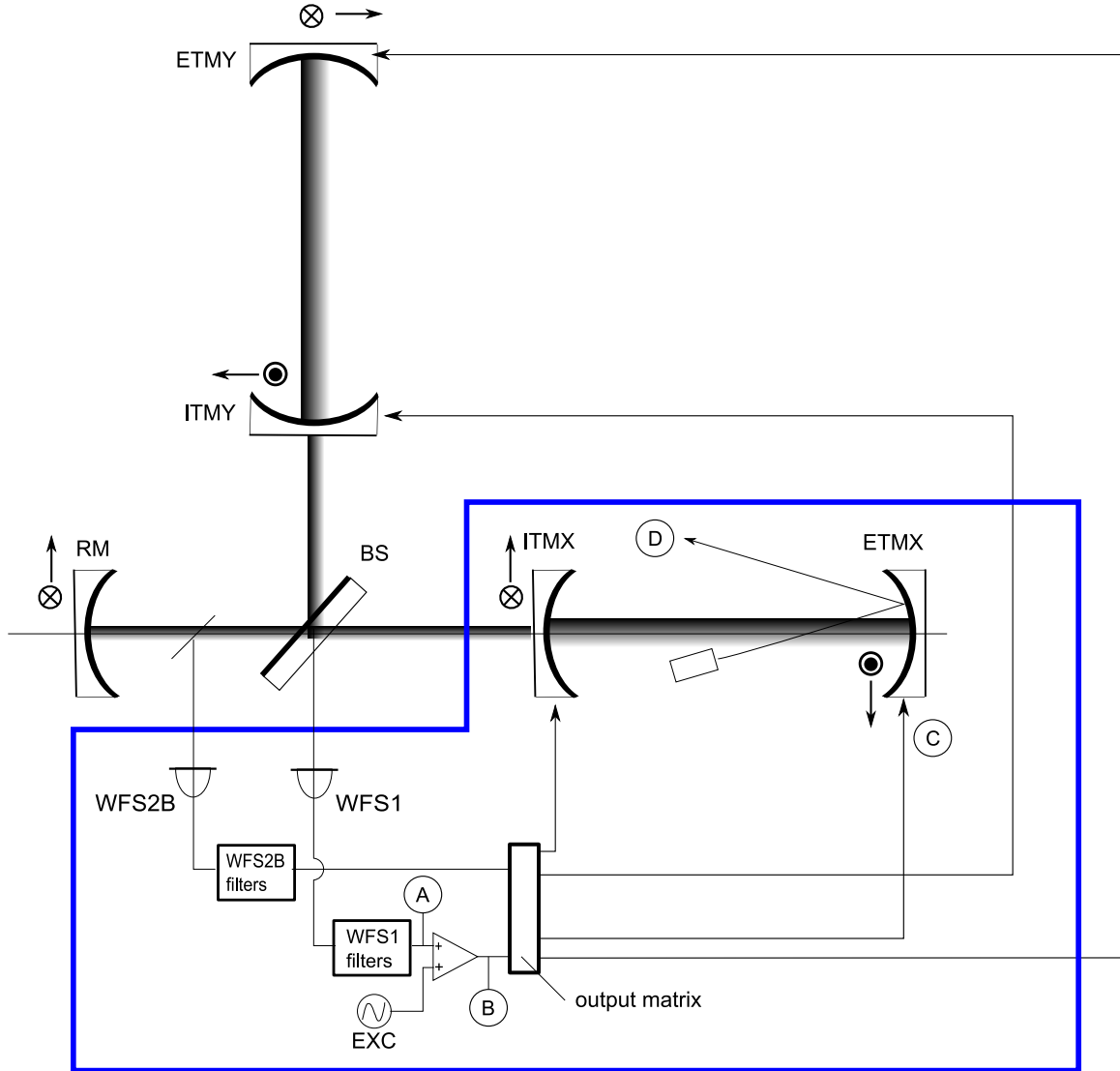
Figure 4.7: Extraction of the system from LIGO detector. An excitation signal is injected into the WFS1 path that dithers ETMX and ETMY in differential basis, i.e., $d\theta_{ETM} = \theta_{ETMX} - \theta_{ETMY}$. Both WFS1 and WFS2B are sensitive to differential angles (dETM, dITM), we only care the contribution to the x-arm. The symbols next to each core optics shows the rotation axes for pitch and yaw tilts. A positive tilt angle follows a right-handed rotation about the axis.

previous chapter, the wave front sensing scheme is not perfectly diagonal but there is always some contamination from other degrees of freedom. For example, WFS1 is the most sensitive to differential motion of end test masses, but it is also sensitive to all the other degrees of freedom. Therefore, we use optical lever output to monitor

pure mirror response[3].

In order to start the measurement, we first have the interferometer in the running condition where the two arm cavities and the recycling cavity are resonant, and the complete control system is engaged. Then, we inject an excitation signal into the WFS1 control path that results in dithering the end test masses differentially based on the output matrix, i.e., $d\theta_{ETM} = \theta_{ETMX} - \theta_{ETMY}$. Both WFS1 and WFS2B are sensitive to differential angles (dETM, dITM), we only extract the contribution to the x-arm for our study. Therefore, if we look at the yaw motion of the ITMY and ETMX, we can reduce 10 degrees of freedom into two [4]. WFS1's signal is fed back to the ETMs, while WFS2B's signal is fed back to both the ETMs and ITMs. This is why we chose WFS1 path for the excitation injection. During the excitation, we monitor the optical lever signal of the end mirror in the x-arm and a signal which goes into the driver of actuator attached to the mirror. Since the driver signal is proportional to the torque produced by the actuator, we are able to monitor the transfer function of the mirror angle D to torque C applied to the same mirror up to some overall gain. The transfer function is the direct analog to the one we introduced in the previous section, i.e., the response of the ETMX mirror angle to the torque applied to the mirror. In addition, we record signals from two points located in just upstream A and downstream B of the excitation point in the WFS1 control loop. This enables us to calculate open loop transfer function of the WFS1 control loop. We here call the two transfer functions OPLEV and OLG respectively.

---

[3]I do not want to give wrong impression about WFS here. The WFS is less noisier than the optical lever. Also, since the WFS does not require extra reference to the interferometer, it does not suffer from DC drift like the optical lever does

[4]Although we can investigate the pitch motion as well, we omit it here. We know the pitch's torsion pendulum frequency is very close to that of yaw's. And, the moment of inertia should be almost identical for both the yaw and the pitch. So, we concentrate on the yaw motion in this thesis although we need to verify in the future that the pitch motion does not have something completely new. Besides, we could extract the x-arm cavity by looking at the common degrees of freedom with the other WFSs. These are left for the future.

$$OPLEV = \frac{D}{C} \qquad (4.2.1)$$

$$OLG = \frac{A}{B} \qquad (4.2.2)$$

We made the measurement at three different input laser powers such as 0.8 W, 4.0 W, and 6.8 W [46]. We kept the entire control system activated during the measurement. Figures 4.8 and 4.9 show Bode diagrams of the measured transfer function as well as simulated results described in the next section. Different markers in the figures correspond to different input powers - 0.8 W :*circles*, 4.0 W :*triangles*, and 6.8 W :*squares*. Coherence of the measurement is listed in the Appendix E.

First, we notice there is only one peak observed in the optical lever transfer function. The peak is associated with a pair of poles $s = \pm i\omega_-$, but the transfer function is much more complicated than (4.1.15) due to the control loops. The reason why we only have one peak is that when loop gain is high enough as iLIGO, a pair of zeros and the other pair of poles $s = \pm i\omega_+$ asymtotically approach the same value and cancel each other. This will be explained in the next section using our mathematical model.

Second, the phase of optical lever transfer function at 6.8W has a 180 degree phase lead, which indicates again that iLIGO would be unstable without control. Since the transfer function OPLEV should not be affected by the control, the transfer function should tell us the system's behavior without control. Precisely speaking, however, it is not completely true, since the ITM is under the influence of control as will be described shortly. Nevertheless, this is evidence that the radiation pressure effect on tilted optical resonators predicted by Sigg and Sidles really exists in the interferometer and the system is already naturally unstable [5].

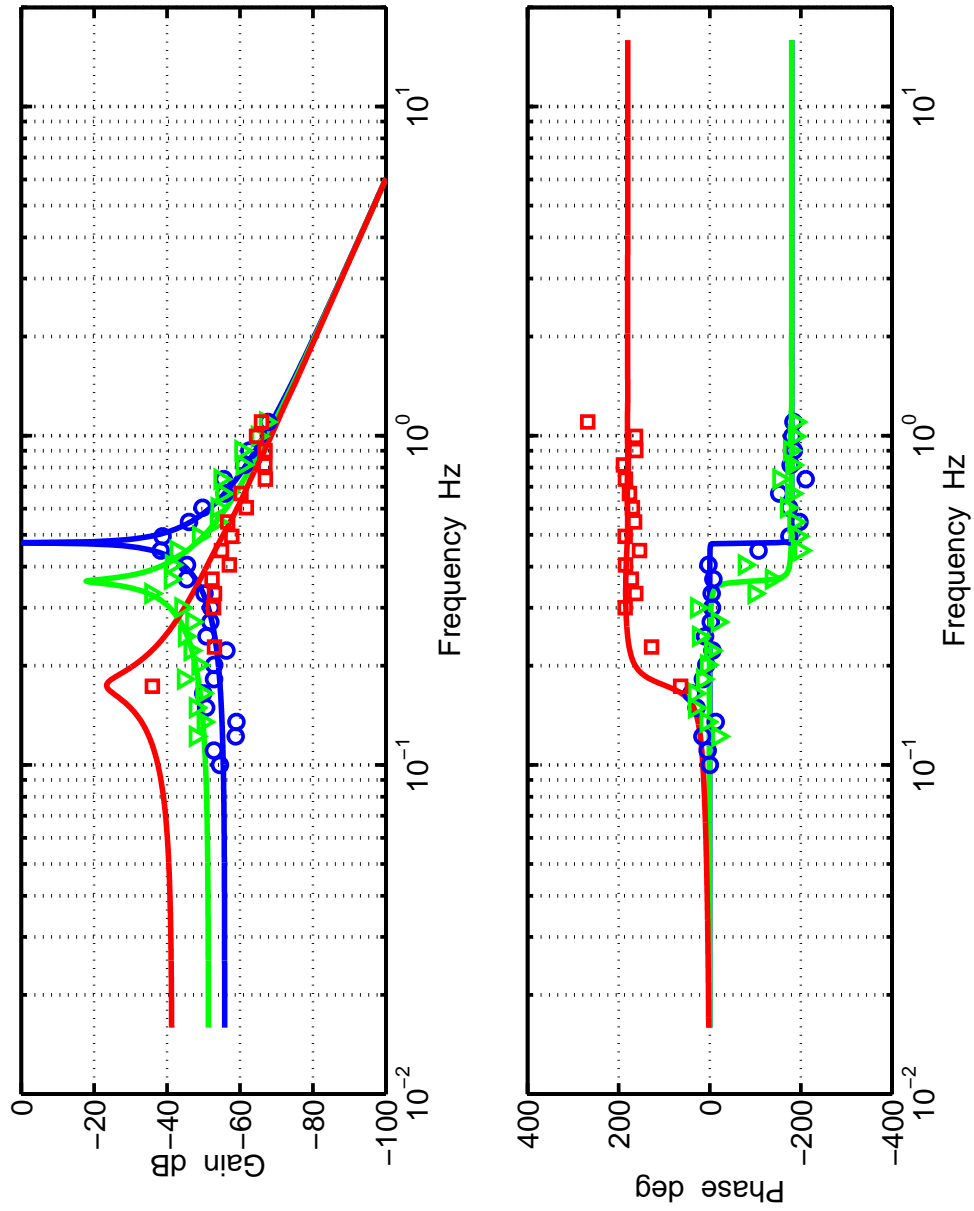[5]By "naturally" we here mean the system without control.

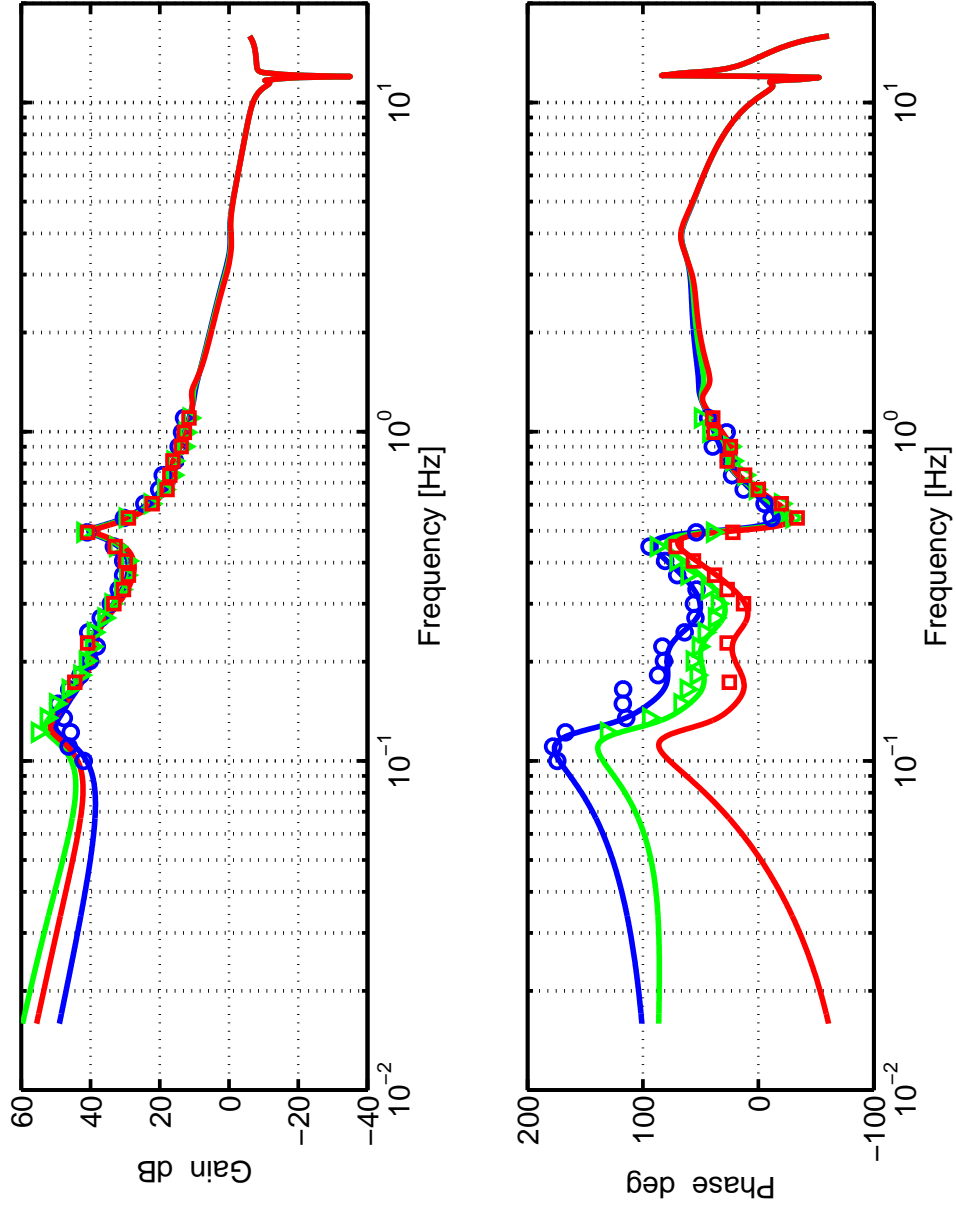Figure 4.8: Bode plot of optical lever transfer function

Figure 4.9: Bode plot of open loop transfer function

Third, the frequency associated with the peak shifts toward lower frequencies as laser power goes up. This is understood as a radiation pressure effect, since the peak we observed corresponds to a pair of poles $s = \pm i\omega_-$ and ω_- goes down as shown in the figure 4.4. But, the frequency does not go down as fast as the system we described in the previous section, which is a case without control, since the WFS control servos enhance the effective restoring force on the ITM. This will be confirmed using our modeling in the next section as well.

Finally, the radiation pressure effect is also observed in phase of the open loop transfer function.

4.3 Modeling

In order to understand the physics of the system[6], we developed a mathematical model with feedback control loops using *Matlab/Simulink* package [60][7].

Figure 4.11 shows the block diagram of the model, which is comprised of a mechanical part and a control part. The mechanical part is circled like C-shape in the block diagram. This part models the (Laplace transformed) equations of motion (4.1.11) and (4.1.12).

The feedback control part is located in the middle of the diagram. WFS sensing and control matrix which are labeled as a, b, c, d and B, C, D respectively. Both WFSs have some sensitivity to the angles of both mirrors (We already showed this in both theoretically and experimentally in the last chapter). As mentioned earlier, WFS1's signal is fed back to only ETM, while WFS2B's signal is fed back to both the ITM and the ETM. These are controlled by the control matrix (B, C, and D) and the matrix is essentially the inverse of the sensing matrix(a,b,c, and d) with some truncation based

---

[6]The mathematical model helped our understanding a lot. Initially, we did not understand why we observed only one peak in the transfer function OPLEV, for instance.

[7]The package is very useful especially a model contains complicated filter banks as our case is.

on the significance as described in chapter 3. We imported the output matrix as of February 2007, which is listed in table 3.3, while we used a sensing matrix measured in December 2005 (See table 3.2). The signals are fed back to each mirror to control the deflection angles. In this model, we assume misalignment angles of the mirrors are perfectly sensed by the WFSs.
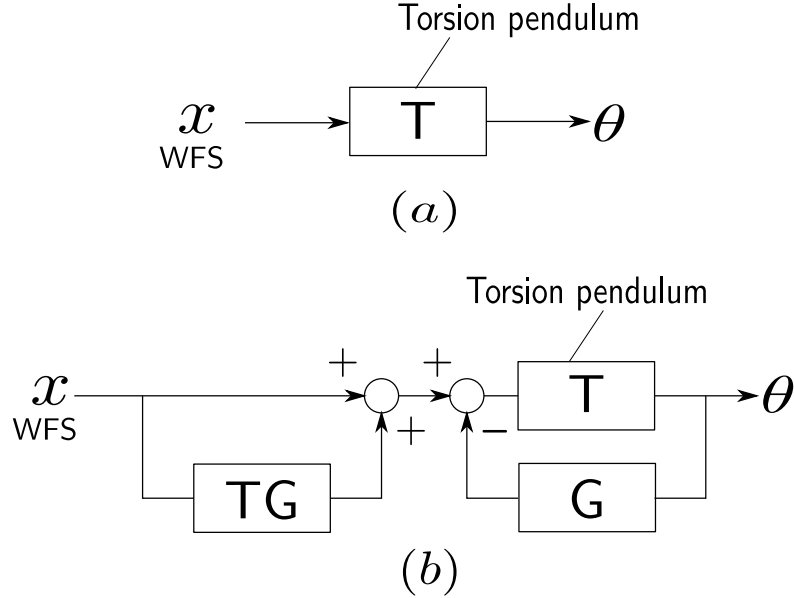

Figure 4.10: Block diagram of oplev compensation. (a) describes the original WFS-pendulum(T) system, while (b) describes the WFS-pendulum(T)-optical lever(G)-optical lever compensation system.

There is also a local loop for each mirror called an optical lever as well as the compensation loop to make the optical lever invisible to WFS's. Figure 4.10 shows a conceptual block diagram of the idea of the optical lever compensation. The diagram (a) does not have optical lever control nor the compensation. In reality, the situation is like the diagram (b). We have the optical lever since the WFS's bandwidth is small (The unity gain frequency is roughly order of a couple of Hz), we added the optical lever loop to enhance the stability of suspended mirrors. The optical lever control loop will modify the transfer function from T to $\frac{T}{1+TG}$, but as we discussed in the chapter 3, the WFS's sensing matrix is measured at a frequency which is free from influence of control. Therefore, the optical lever control will mess up the WFS scheme

unless we add a filter $1 + TG$ in the upstream. This is the concept of the optical lever compensation. However, as we have seen, the torsion pendulum is not static but under influence of radiation pressure from the laser light. So far, T in the $1 + TG$ is fixed, so the compensation will not work well once the cavity stores very high power.

All of the real filter banks associated with the two WFS's are built in the model. The Bode plots of these filters can be found in Appendix D. Commissioning activities in the past done by many people give very useful information to develop the model, such as sensing matrix, WFS's unity gain frequencies, optical lever gain etc. Gains in loops are set to satisfy that information, so the only adjustable parameter comes down to the laser power P inside the arm.

We run the model for a variety of values of P. Following the method of our measurement, we inject an excitation signal in the WFS path which is denoted EXC in the diagram. The transfer function OPLEV is modeled as $\frac{\theta_2}{T}$ here while OLG is modeled as $\frac{Y}{X}$. As already shown in figure 4.8 and figure 4.8, the simulated results agree with our measurement very well. The laser power P in the model for the plots are 1600 W (blue), 7000 W (green), and 12500 W (red) respectively. Knowing that the full interferometer is a much more complicated system with more control loops, the agreement is somewhat surprising. In fact, we have not taken into account common angular motion here, which is sensed and controled by the other WFS's. We could in principle perform the calculation for the common mode in the similar manner, which would involve extension of our model to full interferometer, but this will be left for future work.

Given the agreement between our model and the measurement, we believe our analysis will be very useful for design of future ASC system, especially for Advanced LIGO (AdvLIGO) where laser power is about twenty times the current LIGO's power level.
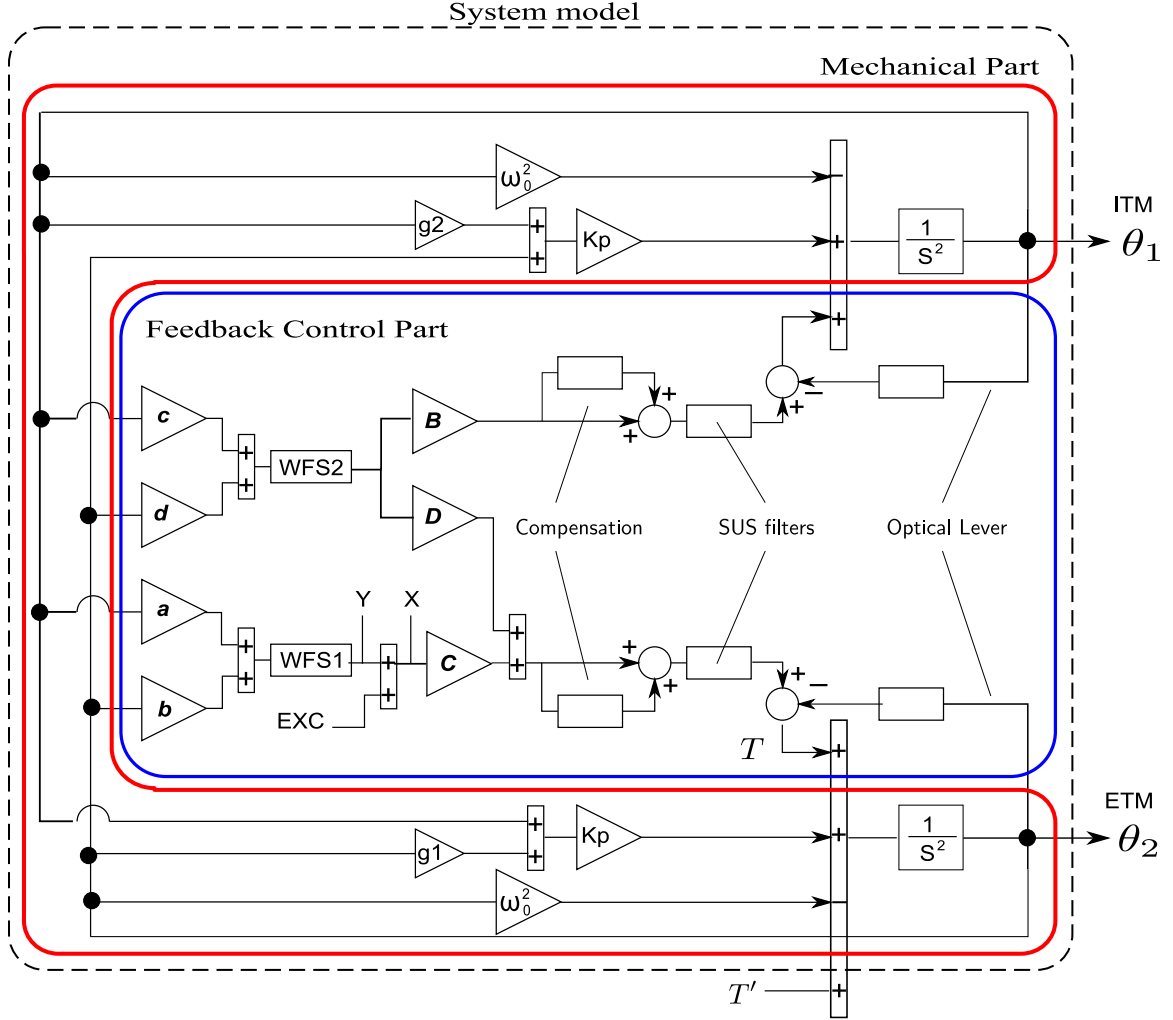
Figure 4.11: Block diagram of coupled torsion pendulum with feedback control loop. a, b, c, d and B, C, D are sensing and control matrix respectively. Rectangular blocks stand for filter banks. $k_p = 2PL/\left[cI(1 - g_1 g_2)\right]$
.

4.3.1 Effects of WFS gain

We briefly mentioned that under influence of WFS control, a pair of poles $s = \pm i\omega_+$ and a pair of zeros $s = \pm i\omega_z$ in the transfer function cancel each other with sufficiently high WFS gain. In order to see the effect clearly, we disable the optical lever loops and the compensation loops when we run the model. The next plots show the transfer function $\frac{D}{C}$ changing gains of WFS1 and WFS2B without the optical lever and the compensation.
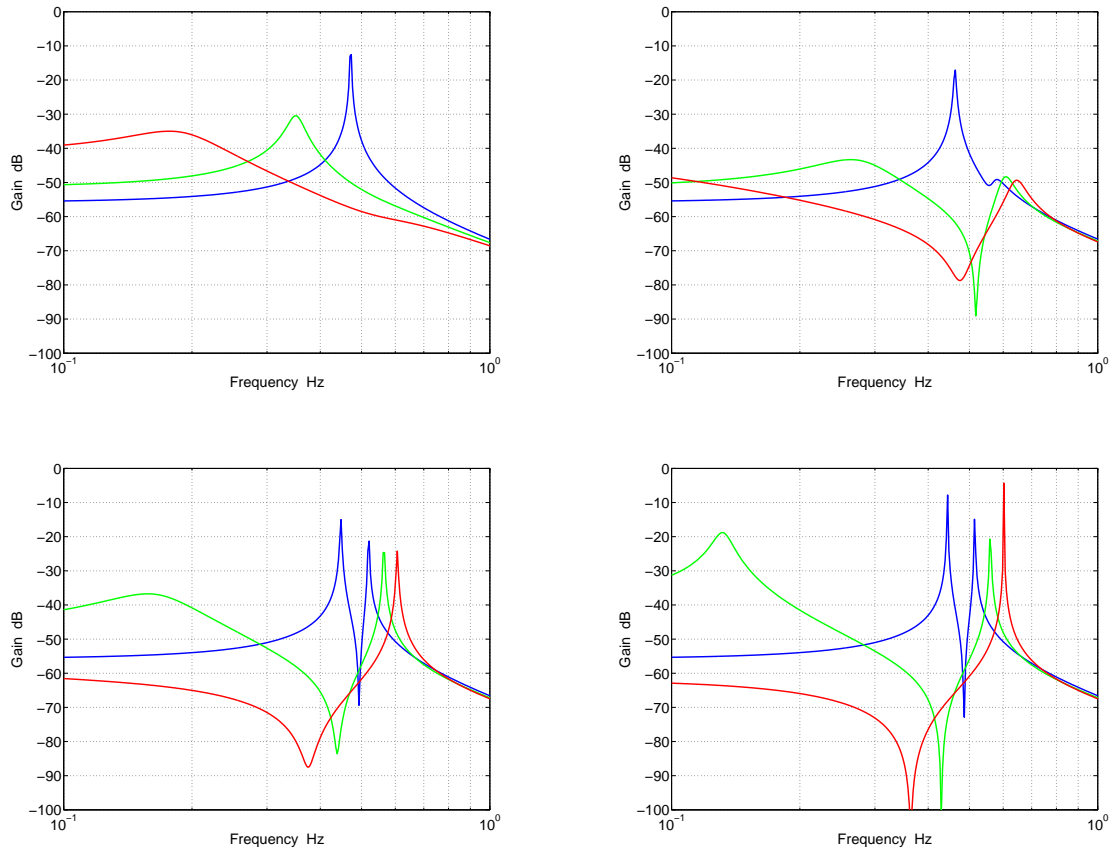
Figure 4.12: Effect of WFS gain on the transfer function $\frac{D}{C}$. (a)*Top left*: The same model as one that creates the figure 4.8 except lack of optical lever control and the compensation. Let's say the gain $G_{WFS} = a$. (b)*Top right*: $G_{WFS} = 0.1 \times a$. (c)*Bottom left*: $G_{WFS} = 0.01 \times a$. (d)*Bottom right*: $G_{WFS} = 0.001 \times a$. The color scheme is as follows - blue: $P = 1600W$, green: $P = 7000W$, red: $P = 12500W$.

As WFS gain goes down, the transfer functions start regaining a property of two pairs of poles. Namely, the peak corresponding to a pair of poles $s = \pm i\omega_+$ and the dip corresponding to a pair of zeros $s = \pm i\omega_z$ are coming out as the WFS gain is decreased. One important feature is that frequency for ω_- goes up as WFS gain goes up. Namely, WFS gain enhances the system stability. Since our transfer function should not see the effect of control on WFS1, this enhancement must come from the effect of the other WFS, i.e., WFS2B. In order to confirm it, we will discuss the case where ITM does not move at all.

4.3.2 Effect of ITM's motion

In the measurement description, we mentioned briefly that frequency corresponding to a pair of pole $s = \pm i\omega_-$ in the transfer function $\frac{D}{C}$ does not go down as fast as one without control. The transfer function $\frac{D}{C}$ is the response of the end mirror's angle to torque applied to the same mirror, so the transfer function won't see the effect of WFS control. Thus, the effect must come from the front mirror ITM. In order to confirm this, we force ITM's motion to be zero. Figure 4.13 shows that the transfer function $\frac{D}{C}$ with ITM's angle zero. We clearly see the peak frequencies at each laser power are higher when we fix the ITM's motion.
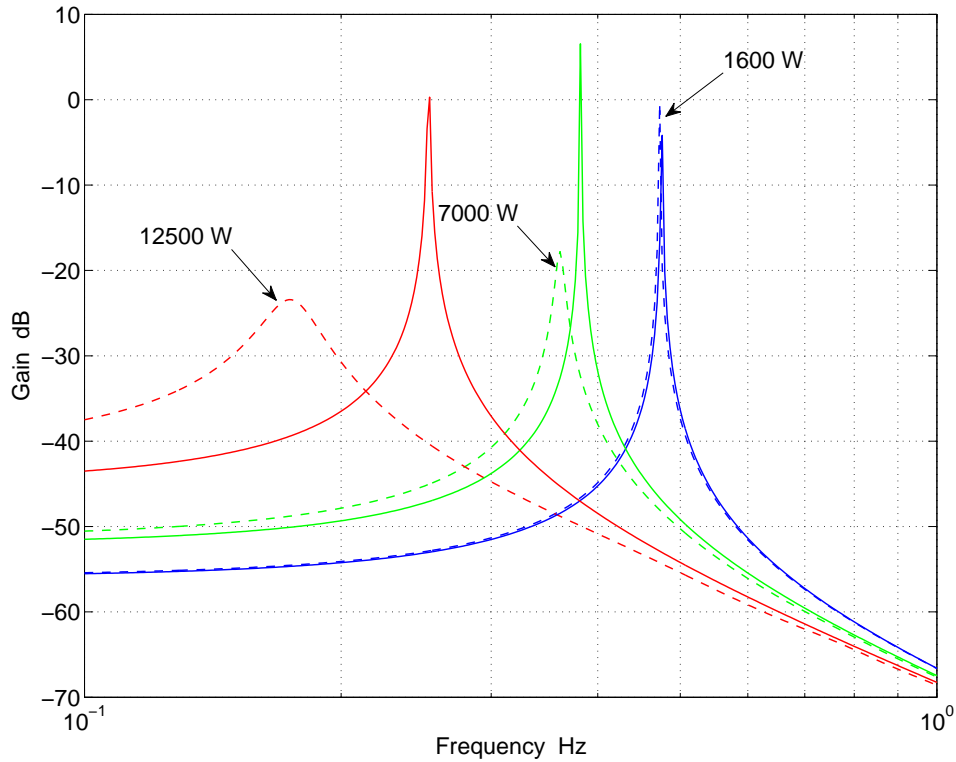

Figure 4.13: Effect of ITM on the transfer function $\frac{D}{C}$. The dashed lines are identical to 4.8 while solid lines are cases when input test mass does not move at all. The plot indicates why peak frequency shift more slowly in the presence of ITM control. The plot also shows the benefit will become larger as radiation pressure is higher.

4.4　Stability

It is very important to know how more power can be handled with the current control scheme for coming high power laser operation. In particular, an upgrade to the iLIGO interferometer is now being developed. It will have laser power three times greater than iLIGO, and will have an almost identical control system to that in iLIGO. As described already, it is understood that if pole location of the closed loop transfer function is in the right half plane, it will make the system unstable.

When we discussed stability of the system without control above, an external torque was applied to the system from 'outside' the system. That corresponds to T . Now we have control loops, so the T is not really 'outside', but is included within the whole system that consists of a mechanical part and a control part. Therefore, in order to judge stability of the whole system, we need to consider another torque T', which is located outside the whole system.

$$H^\star = \frac{\theta_2}{T'}. \tag{4.4.1}$$

Figure 4.14 shows how the system poles move in the *s-plane* as a function of the cavity laser power. We immediately notice the difference between figure 4.14 and figure 4.6. Circles which describe iLIGO full laser power level are now in the left half plane as expected. According to this study, the system will be stable until cavity laser power reaches roughly $P/P_{iLIGO} = 8.5$. Even with the current control settings, then, the radiation pressure effect on ASC should not be an issue at eLIGO (enhanced LIGO) laser power level. As for AdvLIGO (Advanced LIGO), we need to take into account the detailed control design since it is crucial (as we have seen difference between figure 4.14 and figure 4.6). But, we believe, the technique developed here will be useful in AdvLIGO ASC design.

Also, a new approach on this issue is being tested in eLIGO commisioning [65]. They

use a different basis on *stiff* and *soft* for the ASC scheme.

4.5   Conclusions

We observed the radiation pressure effect on ASC of LIGO core optics at LHO. This is the first measurement of this effect performed in the full gravitational wave interferometers. Only one of two angular modes survives with feedback control since the other mode is suppressed when control gain is large enough as it is the case. A mathematical model has been developed to understand the physics, and it indicates that the current system has some margin for higher laser power. Angular instability due to radiation pressure won't happen until laser power reaches about eight times the iLIGO power level. This analysis was based on the differential mode. A more complete analysis including the common mode will be left for future work.
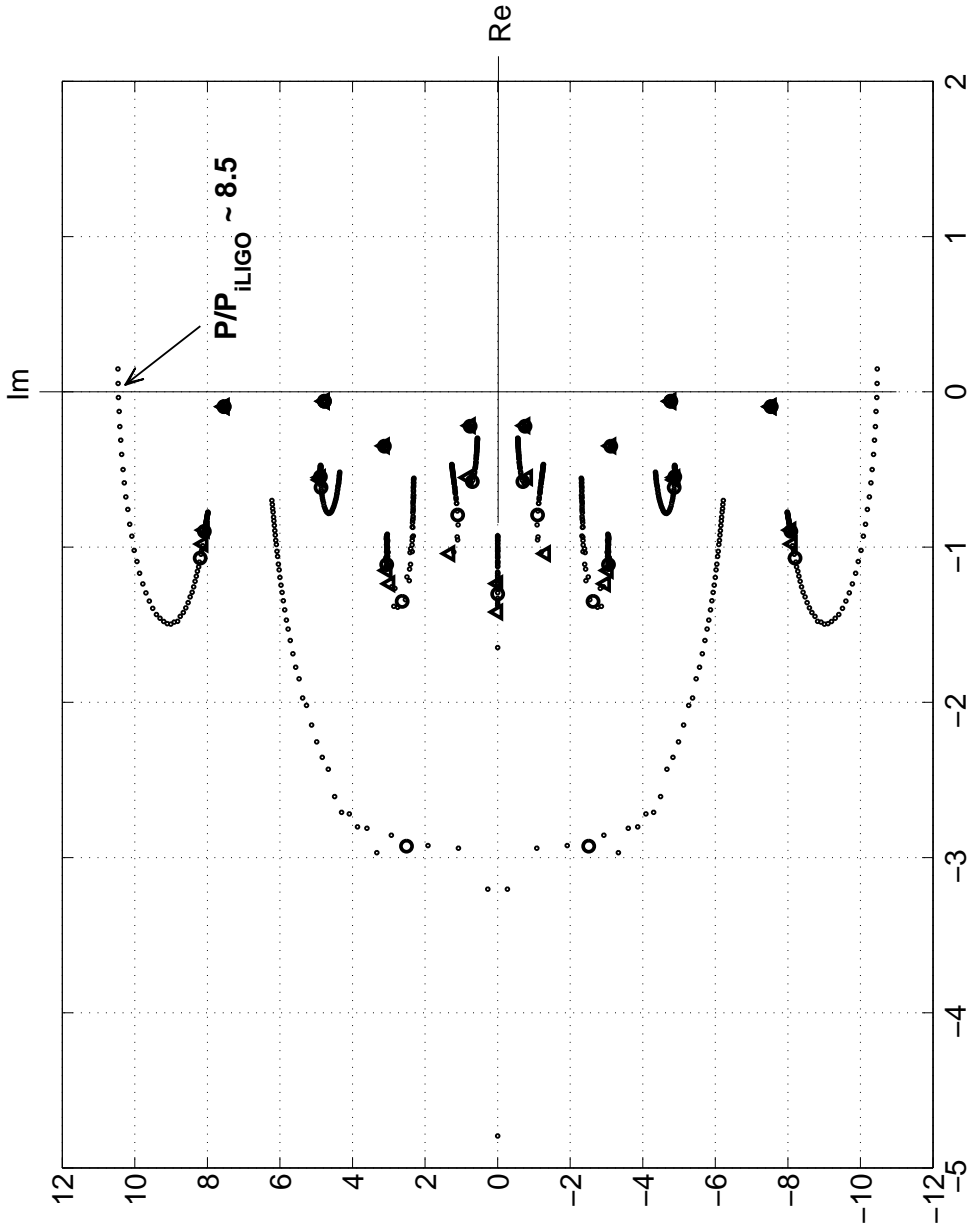
Figure 4.14: Poles of the system with feedback control. Triangles and circles are for $P = 0$, $P = P_{iLIGO}$ respectively.

Appendices

Appendix A

General Relativity

In the following, we will briefly go through the derivation of the wave equation, propagation of gravitational waves, and finally response of test masses to see the two different polarizations $+$ and $\times$, starting with the Einstein-Hilbert action.

A.1   Field equation

Einstein's field equation is derived from the Einstein-Hilbert action

$$S = \int d^4x \sqrt{-g}(\mathcal{L}_G + \mathcal{L}_m) \tag{A.1.1}$$

where g is the determinant of the metric $g = det(g_{\mu\nu})$, $\mathcal{L}_G$ and $\mathcal{L}_m$ are Lagrangian densities for the action of the gravitational field and the action of matter fields on spacetime respectively.

$$\mathcal{L}_G = \frac{c^3}{16\pi G}R \tag{A.1.2}$$

R is the Ricci scalar defined by the Ricci tensor $R_{\mu\nu}$, i.e.,

$$R = R^{\mu}_{\mu} = g^{\mu\nu}R_{\mu\nu} \tag{A.1.3}$$

$$R_{\mu\nu} = R^{\lambda}_{\mu\lambda\nu}. \tag{A.1.4}$$

Varying S_G by the metric $g_{\mu\nu}$, we get

$$\delta S_G = \frac{c^3}{16\pi G}\int d^4x\, \delta(\sqrt{-g}R). \tag{A.1.5}$$

For the variation in the above, we use the following relations

$$\delta(\sqrt{-g}) = -\frac{1}{2}\sqrt{-g}\,g_{\mu\nu}\delta g^{\mu\nu} \tag{A.1.6}$$

$$\delta R = -\delta g^{\mu\nu}R_{\mu\nu} + \nabla_{\mu}(g^{\alpha\beta}\delta\Gamma^{\mu}{}_{\alpha\beta} - g^{\mu\nu}\delta\Gamma^{\alpha}{}_{\nu\alpha}) \tag{A.1.7}$$

to have

$$\frac{16\pi G}{c^3}\delta S_G = \int d^4x\{\sqrt{-g}(R_{\mu\nu} - \frac{1}{2}g_{\mu\nu}R)\delta g^{\mu\nu} + $$
$$\nabla_{\mu}\left[\sqrt{-g}\left(g^{\alpha\beta}\delta\Gamma^{\mu}{}_{\alpha\beta} - g^{\mu\nu}\delta\Gamma^{\alpha}_{\nu\alpha}\right)\right]. \tag{A.1.8}$$

The second term will dissapear using Gauss's theorem. Therefore, variation of S_G becomes

$$\delta S_G = \frac{c^3}{16\pi G}\int d^4x\sqrt{-g}\left(R_{\mu\nu} - \frac{1}{2}g_{\mu\nu}R\right)\delta g^{\mu\nu}, \tag{A.1.9}$$

while the variation of S_M becomes

110

$$\delta S_m \;=\; \int d^4x\, \delta\left(\sqrt{-g}\mathcal{L}_m\right) \tag{A.1.10}$$

$$=\; -\frac{1}{2}\int d^4x\sqrt{-g}T_{\mu\nu}\delta g^{\mu\nu}, \tag{A.1.11}$$

where $T_{\mu\nu}$ is the stress-energy tensor

$$T_{\mu\nu} \equiv \frac{-2}{\sqrt{-g}}\frac{\delta\left(\sqrt{-g}\mathcal{L}_m\right)}{\delta g^{\mu\nu}}. \tag{A.1.12}$$

Thus, requiring $\delta S = 0$, we will get the field equations.

$$R_{\mu\nu} - \frac{1}{2}g_{\mu\nu}R = \frac{8\pi G}{c^3}T_{\mu\nu} \tag{A.1.13}$$

A.2   Linearized theory

Einstein's equations have wave solutions. When spacetime is nearly flat, the metric can be described as a Minkowski metric plus a small deviation, i.e.,

$$g_{\mu\nu} = \eta_{\mu\nu} + h_{\mu\nu}. \tag{A.2.1}$$

Then, the Christoffel symbols are obtained by a straightforward calculation as

$$\Gamma^\mu{}_{\alpha\beta} = \frac{1}{2} \left(\partial_\alpha g_{\mu\beta} + \partial_\beta g_{\alpha\nu} - \partial_\nu g_{\alpha\beta} \right)$$

$$= \frac{1}{2} g^{\mu\nu} \left(\partial_\alpha h_{\nu\beta} + \partial_\beta h_{\alpha\nu} - \partial_\nu h_{\alpha\beta} \right)$$

$$\therefore \Gamma^\mu{}_{\alpha\beta} = \frac{1}{2} \left(\partial_\alpha h^\mu{}_\beta + \partial_\beta h_\alpha{}^\mu - \partial^\mu h_{\alpha\beta} \right). \tag{A.2.2}$$

Therefore, the Ricci tensor will be

$$
\begin{aligned}
R_{\mu\nu} &= R^\alpha{}_{\mu\alpha\nu} = \partial_\alpha \Gamma^\alpha{}_{\mu\nu} - \partial_\nu \Gamma^\alpha{}_{\mu\alpha} + \Gamma^\alpha{}_{\beta\alpha} \Gamma^\beta{}_{\mu\nu} - \Gamma^\alpha{}_{\beta\nu} \Gamma^\beta{}_{\mu\alpha} \\
&= \frac{1}{2} \{ \partial_\alpha \left(\partial_\mu h^\alpha{}_\nu + \partial_\nu h^\alpha{}_\nu - \partial^\alpha h_{\mu\nu} \right) \\
&\quad - \partial_\nu \left(\partial_\mu h^\alpha{}_\alpha + \partial_\alpha h^\alpha{}_\nu - \partial^\alpha h_{\mu\alpha} \right) + O(h^2) \} \\
&\approx \frac{1}{2} \{ \partial_\alpha \partial_\mu h^\alpha{}_\nu - \partial_\alpha \partial^\alpha h_{\mu\nu} - \partial_\nu \partial_\mu h^\alpha{}_\alpha + \partial_\nu \partial^\alpha h_{\mu\alpha} \}. \\
\therefore R_{\mu\nu} &\approx \frac{1}{2} \{ \partial_\alpha \partial_\mu h^\alpha{}_\nu - \partial_\alpha \partial^\alpha h_{\mu\nu} - \partial_\nu \partial_\mu h^\alpha{}_\alpha + \partial_\nu \partial^\alpha h_{\mu\alpha} \}. \tag{A.2.3}
\end{aligned}
$$

The Ricci scalar is therefore given by

$$
\begin{aligned}
R &= g^{\mu\nu} R_{\mu\nu} \\
&= \eta^{\mu\nu} R_{\mu\nu} + O(h^2) \\
&\approx \frac{1}{2} (\partial_\alpha \partial^\nu h^\alpha{}_\nu - \partial_\alpha \partial^\alpha h^\nu{}_\nu - \partial^\mu \partial_\nu h^\alpha{}_\alpha + \partial_\nu \partial^\alpha h^\nu{}_\alpha) \\
&\approx \partial_\alpha \partial^\nu h^\alpha{}_\nu - \partial_\alpha \partial^\alpha h^\nu{}_\nu \\
\therefore R &\approx \partial_\alpha \partial^\nu h^\alpha{}_\nu - \partial_\alpha \partial^\alpha h^\nu{}_\nu \tag{A.2.4}
\end{aligned}
$$

Plugging (A.2.3) and (A.2.4) into the Einstein equations (A.1.13),

$$
\begin{aligned}
L.H.S. \;=\; & \frac{1}{2}\{\partial_\alpha\partial_\mu h^\alpha{}_\nu - \partial_\alpha\partial^\alpha h_{\mu\nu} - \partial_\nu\partial_\mu h^\alpha{}_\alpha + \partial_\nu\partial^\alpha h_{\mu\alpha}\} \\
& - \frac{1}{2}\eta_{\mu\nu}(\partial_\alpha\partial^\nu h^\alpha{}_\nu - \partial_\alpha\partial^\alpha h^\nu{}_\nu) + O(h^2) \\
\therefore \partial_\alpha\partial_\mu h^\alpha{}_\nu \;-\;& \partial_\alpha\partial^\alpha h_{\mu\nu} - \partial_\nu\partial_\mu h^\alpha{}_\alpha \\
+\;& \partial_\nu\partial^\alpha h_{\nu\alpha} - \eta_{\mu\nu}\partial_\alpha\partial^\beta h^\alpha{}_\beta + \eta_{\mu\nu}\partial_\alpha\partial^\alpha h^\beta{}_\beta = \frac{16\pi G}{c^3}T_{\mu\nu}
\end{aligned}
$$

$$
\therefore -\Box\psi_{\mu\nu} + \partial_\alpha\partial_\mu\psi^\alpha{}_\nu + \partial_\nu\partial^\alpha\psi_{\mu\nu} - \eta_{\mu\nu}\partial_\alpha\partial^\beta\psi^\alpha{}_\beta = \frac{16\pi G}{c^3}T_{\mu\nu}, \tag{A.2.5}
$$

where

$$
\psi_{\mu\nu} \;=\; h_{\mu\nu} - \frac{1}{2}\eta_{\mu\nu}h^\alpha{}_\alpha \tag{A.2.6}
$$

$$
\Box \;=\; \partial_\alpha\partial^\alpha \tag{A.2.7}
$$

Now, using the harmonic gauge condition,

$$
\partial_\alpha\psi^\alpha{}_\mu = 0, \tag{A.2.8}
$$

we get a wave equation.

$$
\Box\psi_{\mu\nu} = -\frac{16\pi G}{c^3}T_{\mu\nu} \tag{A.2.9}
$$

A.3 Generation of gravitational waves

A.3.1 Quadrupole formula

The wave equation in electromagnetism is given by

$$\Box A_\mu = -\frac{1}{c\epsilon_0} J_\mu, \tag{A.3.1}$$

and the solution is known to be

$$A_\mu(x) = \frac{1}{4\pi c\epsilon_0} \int d^3x' \frac{J_\mu\left(x^0 - |\mathbf{x} - \mathbf{x'}|, \mathbf{x'}\right)}{|\mathbf{x} - \mathbf{x'}|}. \tag{A.3.2}$$

Applying this result to the wave equation (A.2.9), we can write down the wave solution in terms of the stress-energy tensor. Namely,

$$\psi_{\mu\nu} = \frac{4G}{c^4} \int d^3x' \frac{T_{\mu\nu}\left(x^0 - |\mathbf{x} - \mathbf{x'}|, \mathbf{x'}\right)}{|\mathbf{x} - \mathbf{x'}|} \tag{A.3.3}$$

Using conservation of the energy-momentum tensor $\partial_\mu T^{\mu\nu} = 0$,

$$\partial_0 \int T^{0i} x^j dV = \int \left(\partial_0 T^{0i}\right) x^j dV$$
$$= -\int \partial_k T^{ki} x^j dV = -\int \partial_k \left(T^{ki} x^j\right) dV + \int T^{ij} dV.$$

The first term in the last line will dissapear by Gauss' law.

$$\therefore \partial_0 \int T^{0i} x^j dV = \int T^{ij} dV \tag{A.3.4}$$

Similarly,

$$\partial_0 \int T^{00} x^i x^j \, dV = -\int \partial_k T^{k0} x^i x^j \, dV$$

$$= \int T^{k0} \partial_k \left(x^i x^j \right) dV = \int \left(T^{i0} x^j + T^{j0} x^i \right) dV$$

$$\therefore \partial_0^2 \int T^{00} x^i x^j \, dV = \partial_0 \int \left(T^{i0} x^j + T^{j0} x^i \right) dV = 2 \int T^{ij} \, dV.$$

Therefore, for $x \ll x'$, we can rewrite (A.3.3) in the following way.

$$\therefore \psi_{ij} = \frac{2G}{c^4 R} \int T^{ij} x^i x^j \, dV = \frac{2G}{c^4 R} \partial_0^2 \int \rho x^i x^j \, dV = \frac{2G}{c^4 R} \partial_0^2 I_{ij}, \qquad \text{(A.3.5)}$$

where I_{ij} is the second moment of the mass distribution.

$$I_{ij} = \int \rho x^i x^j \, dV \qquad \text{(A.3.6)}$$

For TT gauge,

$$\psi_{ij}^{TT} = \left(p_i^k p_j^l - \frac{1}{2} p_{ij} p^{kl} \right) \psi_{kl} = h_{ij}^{TT} \qquad \text{(A.3.7)}$$

where

$$p^{ij} = \delta^{ij} - n^i n^j \qquad \text{(A.3.8)}$$

$$n^i = \frac{x^i}{r}. \qquad \text{(A.3.9)}$$

Because of the TT, the second moment of mass distribution is identical to the original one,

$$h_{ij}^{TT} = \frac{2G}{c^4 R} \partial_0^2 I_{ij} = \frac{2G}{c^4 R} \partial_0^2 I_{ij}^{TT}. \qquad \text{(A.3.10)}$$

where

$$I_{ij} = I_{ij} - \frac{1}{3}\delta_{ij}I_k^k \tag{A.3.11}$$

Using Isaacson's formula [58], gravitational wave power emition is given by

$$\left(\dot{E}\right)_{GW} = \frac{c^5}{32\pi G} \int_{r\to\infty} d\Omega r^2 \left\langle \dot{h}^{ijTT} \dot{h}_{ij}{}^{TT} \right\rangle \tag{A.3.12}$$

Now,

$$\dot{h}^{ijTT}\dot{h}_{ij}{}^{TT} = \frac{4G^2}{c^8 r^2} \left(p_i^k p_j^l - \frac{1}{2}p_{ij}p^{kl} \right) \left(p_m^i p_n^j - \frac{1}{2}p_{mn}p^{ij} \right) \dddot{I}_{kl} \dddot{I}^{mn} \tag{A.3.13}$$

Knowing some properties of the projection operator such as $p_{jl}p_{lk} = p_{jk}$ and $p_{kk} = 2$,

$$
\begin{aligned}
&\dot{h}^{ijTT}\dot{h}_{ij}^{TT} \\
&= \frac{4G^2}{c^8 r^2} \left(\delta_m^k \delta_n^l - \delta_m^k n^l n_n - \delta_n^l n^k n_m - \frac{1}{2}\delta_{mn}\delta^{kl} + \frac{1}{2}\delta_{mn}n^k n^l + \frac{1}{2}\delta^{kl}n_m n_n + \frac{1}{2}n_m n_n n^k n^l \right) \dddot{I}_{kl} \dddot{I}^{mn} \\
&= \frac{4G^2}{c^8 r^2} \left(\delta_m^k \delta_n^l - \delta_m^k n^l n_n - \delta_n^l n^k n_m + \frac{1}{2}n_m n_n n^k n^l \right) \dddot{I}_{kl} \dddot{I}^{mn} \cdot \left(\because \dddot{I}_k^{kTT} = 0 \right)
\end{aligned}
$$

Using the following integral formulas $\int d\Omega = 4\pi$, $\int n_i n_j d\Omega = \frac{4\pi}{3}\delta_{ij}$, and $\int n_i n_j n_k n_l d\Omega = \frac{4\pi}{15}\left(\delta_{ij}\delta_{kl} + \delta_{ik}\delta_{jl} + \delta_{il}\delta_{jk}\right)$,

$$
\begin{aligned}
&\int d\Omega r^2 \left\langle \dot{h}^{ijTT}\dot{h}_{ij}^{TT} \right\rangle \\
&= 4\pi \left[\delta_m^k \delta_n^l - \frac{1}{3}\delta_m^k \delta_n^l - \frac{1}{3}\delta_n^l \delta_m^k + \frac{1}{30}\left(\delta_{mn}\delta^{kl} + \delta_m^k \delta_n^l + \delta_m^l \delta_n^k\right) \right] \left\langle \dddot{I}_{kl} \dddot{I}^{mn} \right\rangle \\
&= 4\pi \left(1 - \frac{2}{3} + \frac{2}{30} \right) \left\langle \dddot{I}_{mn} \dddot{I}^{mn} \right\rangle \\
&= \frac{8\pi}{5} \left\langle \dddot{I}_{mn} \dddot{I}^{mn} \right\rangle
\end{aligned}
$$

Finally, we get the Landau-Lifshitz quadrupole radiation formula

$$\therefore \left(\dot{E}\right)_{GW} = \frac{G}{5c^5} \left\langle \dddot{I}_{mn} \dddot{I}^{mn} \right\rangle . \tag{A.3.14}$$

A.3.2 Application of quadrupole formula

Based on the previous calculation, here are some numerical estimations of gravitational radiation, produced by a rotating bar and binary pulsar.

Rotating rod

Suppose we design a gravitational wave generator using a metal rod as shown in figure A.1. The mass, length, density, cross section are M, L, ρ, and A, respectively.
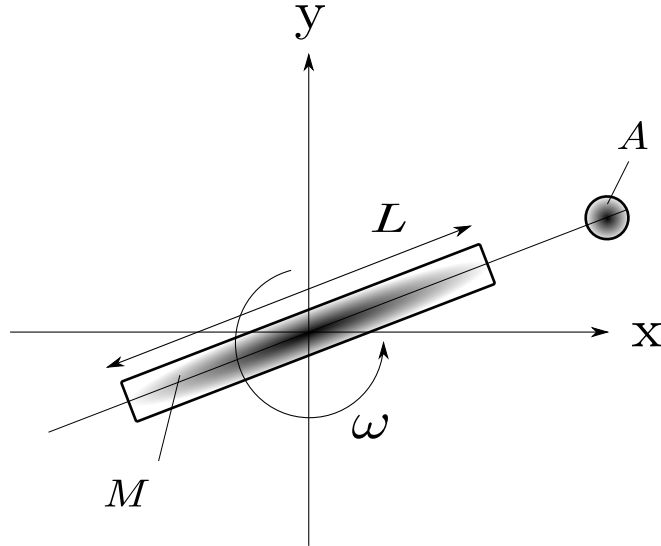
Figure A.1: A rod whose mass, length, cross sectional area are M, L, A is rotating around the origin with angular velocity ω.

First, we calculate the reduced quadrupole moments.

$$I_{xx} = \frac{\rho A L^3}{24}\left(cos2\omega t + \frac{1}{3}\right) = \frac{MAL^2}{24}\left(cos2\omega t + \frac{1}{3}\right) \qquad \text{(A.3.15)}$$

$$I_{yy} = \frac{\rho A L^3}{24}\left(-cos2\omega t + \frac{1}{3}\right) = \frac{MAL^2}{24}\left(-cos2\omega t + \frac{1}{3}\right) \qquad \text{(A.3.16)}$$

$$I_{xy} = I_{yx} = \frac{\rho A L^3}{24}\left(sin2\omega t\right) = \frac{MAL^2}{24}\left(sin2\omega t\right) \qquad \text{(A.3.17)}$$

The strain measured by an observor R away from the detector is given by

$$|h| = \frac{2G}{Rc^4}\frac{ML^2\omega^2}{6} \qquad \text{(A.3.18)}$$

Stress in the rod can be calculated by

$$\sigma = \frac{ML\omega^2}{8A}\left(1 - \frac{4r^2}{L^2}\right). \qquad \text{(A.3.19)}$$

So, maximum stress occurs at the center of the rod, i.e.,

$$\sigma_{max} = \frac{ML\omega^2}{8A} = \frac{\rho L^2\omega^2}{8}. \qquad \text{(A.3.20)}$$

Suppose we plan to detect the waves by a state-of-the-art gravitational wave detector on the Earth, LIGO in which the best sensitivity of the detector comes around 100Hz. The material of the rod is, say, Titunium-64 whose density is 4400 $\left[\frac{kg}{m^3}\right]$ and UTS (Ultimate Tensile Strength) is roughly 1000 MPa. Plugging in these numbers,

$$\therefore L \lesssim \sqrt{\frac{8\sigma_{max}}{\rho\omega^2}} \approx 2\,[m] \qquad \text{(A.3.21)}$$

We choose $A = 1$ m^2 (It makes the bar's mass about 9 tons!), and $R = 10$ m. Assuming that we find a motor to drive the monster bar, which is also so quiet that

the LIGO detector does not sense it,

$$|h| \cong 10^{-30}. \tag{A.3.22}$$

The monster is not going to generate observable gravitational waves.

PSR B1913+16

Hulse and Taylor found that the rate of change of the orbital period (of a binary pulsar) predicted by general relativity fits their observation of PSR B1913+16 very well [63, 64]. It is known that the rate of change of the semimajor axis for a system of two point masses in elliptical orbit is given by

$$\left\langle \frac{da}{dt} \right\rangle = -\frac{64}{5} \frac{G^3 m_1 m_2 (m_1 + m_2)}{c^5 a^3 (1 - e^2)^{7/2}} \left(1 + \frac{73}{24} e^2 + \frac{37}{96} e^4 \right), \tag{A.3.23}$$

where e is eccentricity. And, from Kepler's third law,

$$\left(\frac{T}{2\pi} \right)^2 = \frac{a^3}{G(m_1 + m_2)}. \tag{A.3.24}$$

From these equations,

$$\dot{T} = \frac{2\pi}{\sqrt{G(m_1 + m_2)}} \frac{3}{2} a^{\frac{1}{2}} \dot{a} \tag{A.3.25}$$

$$= -\frac{192}{5} \frac{\pi G^{\frac{5}{3}}}{c^5} \left(\frac{T}{2\pi} \right)^{-\frac{5}{3}} (1 - e^2)^{-\frac{7}{2}}$$

$$\times \left(1 + \frac{73}{24} e^2 + \frac{37}{96} e^4 \right) m_1 m_2 (m_1 + m_2)^{-\frac{1}{3}} \tag{A.3.26}$$

A fact that the rate of change of orbital period predicted by general relativity fits their observation of PSR B1913 (figure A.2), strongly support emission of gravitational waves. The difficulty of making observable gravitational wave generator on the Earth,
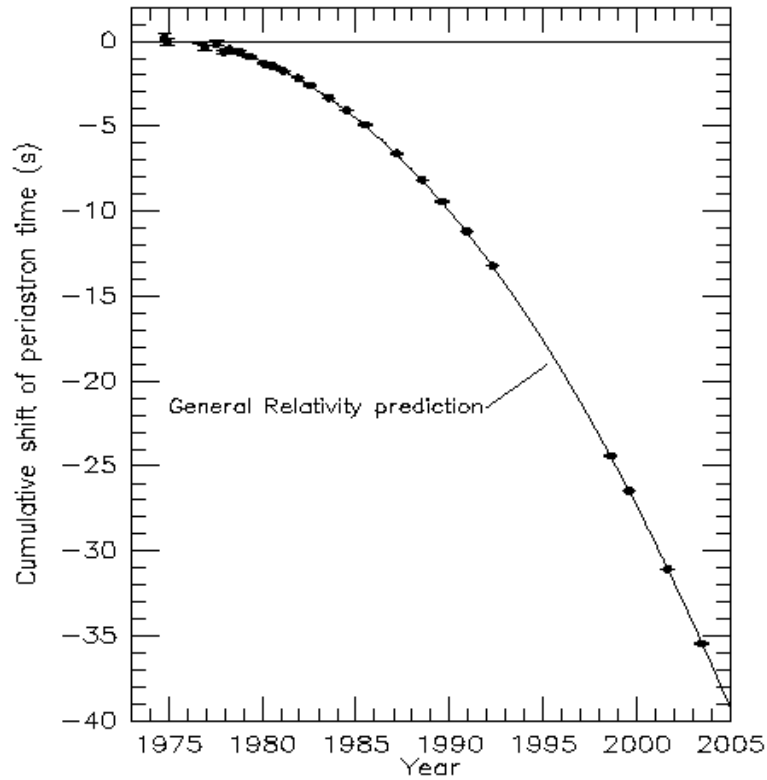
Figure 1.   Orbital decay of PSR B1913+16. The data points indicate
the observed change in the epoch of periastron with date while the
parabola illustrates the theoretically expected change in epoch for a
system emitting gravitational radiation, according to general relativity.

Figure A.2: Orbital decay of PSR B1913+16: copy from [64].

as discussed in the rotating rod case, and the discovery of PSR B1913+16 binary pulsar have motivated us to look for gravitational wave sources in the space.

A.4   Propagation of gravitational waves

In order to see how gravitational waves propagate in vacuum, we consider plane wave solutions to the Einstein field equations in the harmonic gauge (A.2.8). Using the same quantity as (A.2.6),

$$\Box \psi = 0 \tag{A.4.1}$$

$$\partial_\alpha \psi^\alpha{}_\mu = 0 \tag{A.4.2}$$

And we take the ansatz as follows.

$$\psi_{\mu\nu} = a_{\mu\nu} e^{ik\cdot x} \tag{A.4.3}$$

Plugging this ansatz into (A.4.1),

$$\begin{aligned}
\Box \psi &= \partial_\alpha \partial^\alpha a_{\mu\nu} e^{ik_\sigma x^\sigma} \\
&= -k_\alpha k^\alpha a_{\mu\nu} e^{ik\cdot x} = 0 \\
\therefore k_\alpha k^\alpha &= 0.
\end{aligned} \tag{A.4.4}$$

While plugging into (A.4.2),

$$\begin{aligned}
\partial_\alpha \psi^\alpha{}_\mu &= ik_\alpha \psi^\alpha{}_\mu = 0 \\
\therefore k_\alpha a^\alpha{}_\mu &= 0
\end{aligned} \tag{A.4.5}$$

(A.4.4) means k is lightlike while (A.4.5) means $a_{\mu\nu}$ is perpendicular to the direction of propagation. Therefore, the solution describes a transverse wave that propagates with the speed of the light. Since these conditions do not completely fix the degree of freedom, we introduce another gauge condition. That is equivalent to just having transverse traceless (TT) gauge in the initial perturbed metric $h_{\mu\nu}$, but here we rather explain how it leads to the condition. In order to do it, we introduce a new coordinate x' slightly different (to order h) from the original coordinate x.

$$\xi^\mu = x'^\mu - x^\mu \tag{A.4.6}$$

$$\therefore \frac{\partial x'^\mu}{\partial x^\nu} = \frac{\partial \xi^\mu}{\partial x^\nu} + \frac{\partial x^\mu}{\partial x^\nu}$$
$$= \delta^\mu_\nu + \partial_\nu \xi^\mu \tag{A.4.7}$$

$$\frac{\partial x^\nu}{\partial x'^\mu} = \frac{\partial x'^\nu}{\partial x'^\mu} - \frac{\partial \xi^\nu}{\partial x'^\mu}$$
$$= \delta^\nu_\mu - \partial_\mu \xi^\nu \tag{A.4.8}$$

Therefore,

$$g'(x') = \frac{\partial x^\lambda}{\partial x'^\mu} \frac{\partial x^\rho}{\partial x'^\nu} g_{\lambda\rho}$$
$$= \left(\delta^\lambda_\mu - \partial_\mu \xi^\lambda\right)\left(\delta^\rho_\nu - \partial_\nu \xi^\rho\right) g_{\lambda\rho}$$
$$= \left(\delta^\lambda_\mu \delta^\rho_\nu - \partial_\nu \xi^\rho \delta^\lambda_\mu - \partial_\mu \xi^\lambda \delta^\rho_\nu\right) g_{\lambda\rho}$$
$$\therefore g'(x') = g_{\mu\nu} - \partial_\nu \xi^\rho g_{\mu\rho} - \partial_\nu \xi^\lambda g_{\lambda\nu} \tag{A.4.9}$$

From (A.2.1),

$$g'_{\mu\nu} = \eta_{\mu\nu} + h_{\mu\nu} - (\eta_{\mu\rho} + h_{\mu\rho})\partial_\nu \xi^\rho - (\eta_{\lambda\nu} + h_{\lambda\nu})\partial_\mu \xi^\lambda$$
$$= \eta_{\mu\nu} + h_{\mu\nu} - \partial_{nu}\xi_\mu - \partial_\mu \xi_\nu - O(\xi^2)$$
$$\therefore h'_{\mu\nu} = h_{\mu\nu} - \partial_\nu \xi_\mu - \partial_\mu \xi_\nu. \tag{A.4.10}$$

Similarly,

$$
\begin{aligned}
\psi'_{\mu\nu} &= h'_{\mu\nu} - \frac{1}{2} h' \eta_{\mu\nu} \\
&= h_{\mu\nu} - \partial_\nu \xi_\mu - \partial_\mu \xi_\nu - \frac{1}{2} \eta^{\rho\sigma} h'_{\rho\sigma} \eta_{\mu\nu} \\
&= h_{\mu\nu} - \partial_\nu \xi_\mu - \partial_\mu \xi_\nu - \frac{1}{2} \eta^{\rho\sigma} (h_{\rho\sigma} - \partial_\rho \xi_\sigma - \partial_\sigma \xi_\rho) \eta_{\mu\nu} \\
&= h_{\mu\nu} - \partial_\nu \xi_\mu - \partial_\mu \xi_\nu - \frac{1}{2} (h^\sigma{}_\sigma - \partial^\sigma \xi_\sigma - \partial^\sigma \xi_\sigma) \eta_{\mu\nu} \\
\therefore \psi'_{\mu\nu} &= \psi_{\mu\nu} - \partial_\nu \xi_\mu - \partial_\mu \xi_\nu + \partial_\alpha \xi^\alpha \eta_{\mu\nu} \qquad\qquad\qquad (\text{A.4.11})
\end{aligned}
$$

Now, in order to fix the gauge freedom , let's consider the following gauge transformation.

$$
\xi_\mu = b_\mu e^{ik \cdot x} \qquad\qquad\qquad (\text{A.4.12})
$$

Using (A.4.3) and (A.4.11),

$$
a'_{\mu\nu} e^{ik \cdot x} = a_{\mu\nu} e^{ik \cdot x} - ik_\mu b_\nu e^{ik \cdot x} - ik_\nu b_\mu e^{ik \cdot x} + ik_\alpha b^\alpha e^{ik \cdot x} \eta_{\mu\nu}
$$
$$
\therefore a'_{\mu\nu} = a_{\mu\nu} - i(k_\mu b_\nu + k_\nu b_\mu - k \cdot b \eta_{\mu\nu}) \qquad\qquad (\text{A.4.13})
$$

In particular, for the spatial part,

$$
\begin{aligned}
a'^j{}_j &= a^j{}_j - i(k_j b^j + b_j k^j - k \cdot b \eta^j{}_j) \\
&= a^j{}_j - i(2\boldsymbol{k} \cdot \boldsymbol{b} - 3(k_0 b^0 + \boldsymbol{k} \cdot \boldsymbol{b})) \\
&= a^j{}_j + i(\boldsymbol{k} \cdot \boldsymbol{b} + 3k_0 b^0).
\end{aligned}
$$

So, choosing b_0 properly, we can have

$$
a^j{}_j = 0 \qquad\qquad\qquad (\text{A.4.14})
$$

Similarly,

$$
\begin{aligned}
a'_{jl}k^l &= \left(a_{jl} - i\left(k_j b_l + k_l b_j - k \cdot b \eta_{jl}\right)\right)k^l \\
&= a_{jl}k^l - i\left(k_j b_l k^l + k_l k^l b_j - k \cdot b k_j\right) \\
&= a_{jl}k^l - i\left(|\boldsymbol{k}|^2 b_j - \left(k^0 b_0\right)k_j\right).
\end{aligned}
$$

Choosing b_j properly, we can have

$$
a_{jl}k^l = 0. \tag{A.4.15}
$$

We see that the gauge transformation has added four more constraints. (A.4.5) adds four constraints, so the degree of freedom becomes six from ten. (Ten comes from symmetry of $a_{\mu\nu}$.) And, (A.4.14) and (A.4.15) add four more constraints to make the degree of freedom two. Now, consider a gravitational wave traveling along the z zxis.

$$
k = (k^0, k^1, k^2, k^3) = \left(\frac{\omega}{c}, 0, 0, \frac{\omega}{c}\right) \tag{A.4.16}
$$

From (A.4.5), (A.4.14), and (A.4.15),

$$
a_{\mu 0} + a_{\mu 3} = 0 \tag{A.4.17}
$$

$$
a_{11} + a_{22} + a_{33} = 0 \tag{A.4.18}
$$

$$
a_{j3} = 0. \tag{A.4.19}
$$

From these, we finally get

$$a_{\mu\nu} = \begin{pmatrix} 0 & 0 & 0 & 0 \\ 0 & a_{11} & a_{12} & 0 \\ 0 & a_{12} & -a_{11} & 0 \\ 0 & 0 & 0 & 0 \end{pmatrix}. \tag{A.4.20}$$

After all, this is just equivalent to having the so-called TT gauge.

$$\psi_{0\mu} = 0 \tag{A.4.21}$$

$$\psi^j{}_j = 0 \tag{A.4.22}$$

$$\partial_k \psi^k{}_j = 0 \tag{A.4.23}$$

Or, even knowing $\psi_{ij}^{TT} = h_{ij}^{TT}$,

$$h_{0\mu} = 0 \tag{A.4.24}$$

$$h^j{}_j = 0 \tag{A.4.25}$$

$$\partial_k h^k{}_j = 0 \tag{A.4.26}$$

If we look at the spatial part of a_{ij}, it can be expressed as

$$a_{ij} = a_{11} \begin{pmatrix} 1 & 0 & 0 \\ 0 & -1 & 0 \\ 0 & 0 & 0 \end{pmatrix} + a_{12} \begin{pmatrix} 0 & 1 & 0 \\ 1 & 0 & 0 \\ 0 & 0 & 0 \end{pmatrix}. \tag{A.4.27}$$

They are considered two different modes choosing x-y axes as principal axis. Then, the first term can be considered as the normal stress while the second term can be viewed as the shear stress acting on spacetime.

These modes are called '+ mode' and 'x mode' respectively.

a_{22}

a_{21}

a_{11}

a_{12}
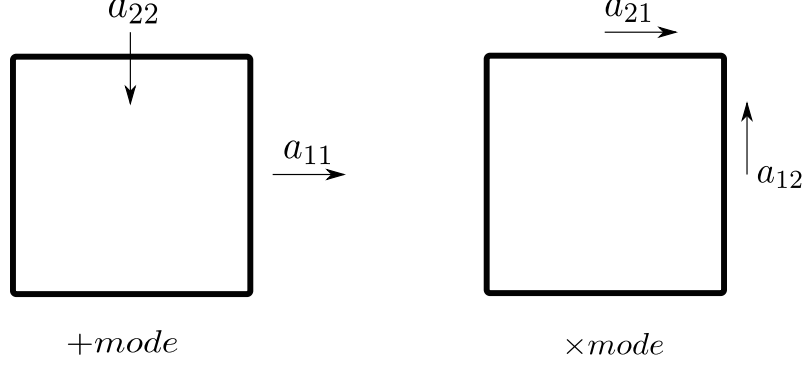
$+mode$

$\times mode$

Figure A.3: Two modes.

A.5   Response of test mass

We now consider two masses close to each other falling freely whose worldlines are $x^\mu(\tau)$ and $x^\mu(\tau) + \delta x^\mu(\tau)$ respectively. They obey geodesic equations.

$$\frac{d^2 x^\mu}{d\tau^2} + \Gamma^\mu{}_{\nu\lambda}(x)\frac{dx^\nu}{d\tau}\frac{dx^\lambda}{d\tau} = 0 \tag{A.5.1}$$

$$\frac{d^2}{d\tau^2}\left[x^\mu + \delta x^\mu\right] + \Gamma^\mu{}_{\nu\lambda}(x + \delta x)\frac{d}{d\tau}\left[x^\nu + \delta x^\nu\right]\frac{d}{d\tau}\left[x^\lambda + \delta x^\lambda\right] = 0 \tag{A.5.2}$$

Subtracting (A.5.1) from (A.5.2),

$$\frac{d^2 \delta x^\mu}{d\tau^2} + \partial_\rho \Gamma^\mu{}_{\nu\lambda}\delta x^\rho \frac{dx^\nu}{d\tau}\frac{dx^\lambda}{d\tau} + 2\Gamma^\mu{}_{\nu\lambda}\frac{dx^\nu}{d\tau}\frac{d\delta x^\lambda}{d\tau} = 0. \tag{A.5.3}$$

Covariant derivative of δx^μ along $x^\mu(\tau)$ is

$$\frac{D(\delta x^\mu)}{D\tau} = \frac{d(\delta x^\mu)}{d\tau} + \Gamma^\mu{}_{\nu\lambda}\frac{dx^\lambda}{d\tau}\delta x^\nu. \tag{A.5.4}$$

Therefore,

$$\frac{D^2}{D\tau^2}(\delta x^\mu) = \frac{d}{d\tau}\left[\frac{d(\delta x^\mu)}{d\tau} + \Gamma^\mu{}_{\alpha\beta}\frac{dx^\alpha}{d\tau}\delta x^\beta\right]$$

$$+ \Gamma^\mu{}_{\nu\lambda}\frac{dx^\lambda}{d\tau}\left[\frac{d(\delta x^\nu)}{d\tau} + \Gamma^\nu{}_{\alpha\beta}\frac{dx^\alpha}{d\tau}\delta x^\beta\right]$$

$$= \frac{d^2}{d\tau^2}\delta x^\mu + \partial_\rho\Gamma^\mu{}_{\alpha\beta}\frac{dx^\rho}{d\tau}\frac{dx^\alpha}{d\tau}\delta x^\beta + \Gamma^\mu{}_{\alpha\beta}\frac{d^2x^\alpha}{d\tau^2}\delta x^\beta$$

$$+ \Gamma^\mu{}_{\alpha\beta}\frac{dx^\alpha}{d\tau}\frac{d(\delta x^\beta)}{d\tau} + \Gamma^\mu{}_{\nu\lambda}\frac{dx^\lambda}{d\tau}\frac{d(\delta x^\nu)}{d\tau} + \Gamma^\mu{}_{\nu\lambda}\Gamma^\nu{}_{\alpha\beta}\frac{dx^\lambda}{d\tau}\frac{dx^\alpha}{d\tau}\delta x^\beta.$$

Using (A.5.1) and (A.5.3),

$$\frac{D^2}{D\tau^2}(\delta x^\mu) = -\partial_\rho\Gamma^\mu{}_{\nu\lambda}\delta x^\rho\frac{dx^\nu}{d\tau}\frac{dx^\lambda}{d\tau} - 2\Gamma^\nu{}_{\nu\lambda}\frac{dx^\nu}{d\tau}\frac{d(\delta x^\lambda)}{d\tau}$$

$$+ \partial_\rho\Gamma^\mu{}_{\alpha\beta}\frac{dx^\rho}{d\tau}\frac{dx^\alpha}{d\tau}\delta x^\beta + \Gamma^\nu{}_{\alpha\beta}\delta x^\beta\left(-\Gamma^\alpha{}_{\nu\lambda}\frac{dx^\nu}{d\tau}\frac{dx^\lambda}{d\tau}\right)$$

$$+ \Gamma^\mu{}_{\alpha\beta}\frac{dx^\alpha}{d\tau}\frac{d(\delta x^\beta)}{d\tau} + \Gamma^\nu{}_{\nu\lambda}\frac{dx^\lambda}{d\tau}\frac{d(\delta x^\nu)}{d\tau} + \Gamma^\mu{}_{\nu\lambda}\Gamma^\nu{}_{\alpha\beta}\frac{dx^\lambda}{d\tau}\frac{dx^\alpha}{d\tau}\delta x^\beta$$

$$= (\partial_\rho\Gamma^\mu{}_{\nu\beta} - \partial_\beta\Gamma^\mu{}_{\rho\nu} + \Gamma^\nu{}_{\alpha\rho}\Gamma^\alpha{}_{\nu\beta} - \Gamma^\nu{}_{\alpha\beta}\Gamma^\alpha{}_{\rho\nu})\frac{dx^\rho}{d\tau}\frac{dx^\nu}{d\tau}\delta x^\beta.$$

$$\therefore \frac{D^2}{D\tau^2}\delta x^\lambda = R^\lambda{}_{\nu\mu\rho}\frac{dx^\rho}{d\tau}\frac{dx^\nu}{d\tau}\delta x^\mu \qquad\qquad (A.5.5)$$

Assuming slow motion, i.e.,

$$\frac{dx^0}{d\tau} \,\backsim\, 1$$

$$\frac{dx^{(i)}}{d\tau} \,\lll\, 1,$$

$$\frac{d^2\delta x^i}{dt^2} = R^i{}_{0j0}z^j. \qquad\qquad (A.5.6)$$

Under TT gauge,

$$\Gamma^i{}_{00} = 0$$

$$\Gamma^i{}_{j0} = \frac{1}{2}\partial_0 h^i{}_j$$

$$R^i{}_{0j0} = \partial_k \Gamma^i{}_{00} - \partial_0 \Gamma^i{}_{k0} + \Gamma^i{}_{km}\Gamma^m{}_{00} - \Gamma^i{}_{0m}\Gamma^m{}_{k0}$$

$$\curlyvee -\frac{1}{2}\partial_0^2 h^i{}_j.$$

Therefore, (A.5.5) can be rewritten as

$$\frac{d^2 \delta x^i}{dt^2} = \frac{1}{2}\partial_0^2 h^i{}_j \delta x^j. \tag{A.5.7}$$

From (A.4.3),

$$h_{11} = a_{11} cos\{(\omega(t - z/c))\} \tag{A.5.8}$$

$$h_{12} = a_{12} cos\{(\omega(t - z/c))\}. \tag{A.5.9}$$

So, for the + mode, having $a_{12} = 0$, rewriting δx with normal x

$$\ddot{x} = \frac{1}{2}\frac{\partial^2}{\partial t^2}a_{11}x \tag{A.5.10}$$

$$\ddot{y} = \frac{1}{2}\frac{\partial^2}{\partial t^2}a_{22}y. \tag{A.5.11}$$

Integration gives

$$x = x(0) + \frac{1}{2}a_{11} cos\{(\omega(t - z/c))\}x(0) \tag{A.5.12}$$

$$y = y(0) - \frac{1}{2}a_{11} cos\{(\omega(t - z/c))\}y(0). \tag{A.5.13}$$

where $x \ll x(0)$ was used. Similarly, for the $\times$ mode,

$$x = x(0) + \frac{1}{2}a_{12}cos\left\{(\omega\left(t - z/c\right))\right\}y(0) \tag{A.5.14}$$

$$y = y(0) + \frac{1}{2}a_{12}cos\left\{(\omega\left(t - z/c\right))\right\}x(0). \tag{A.5.15}$$

The Sketch in the figure shows how test particles move according to the analysis above at $z = 0$. Test particles are initially on unit circle (black) at $T = 0$. Then as a gravitational wave arrives, they are stretched in one direction and compressed in the other direction as blue curves. The sketch shows one full cycle.
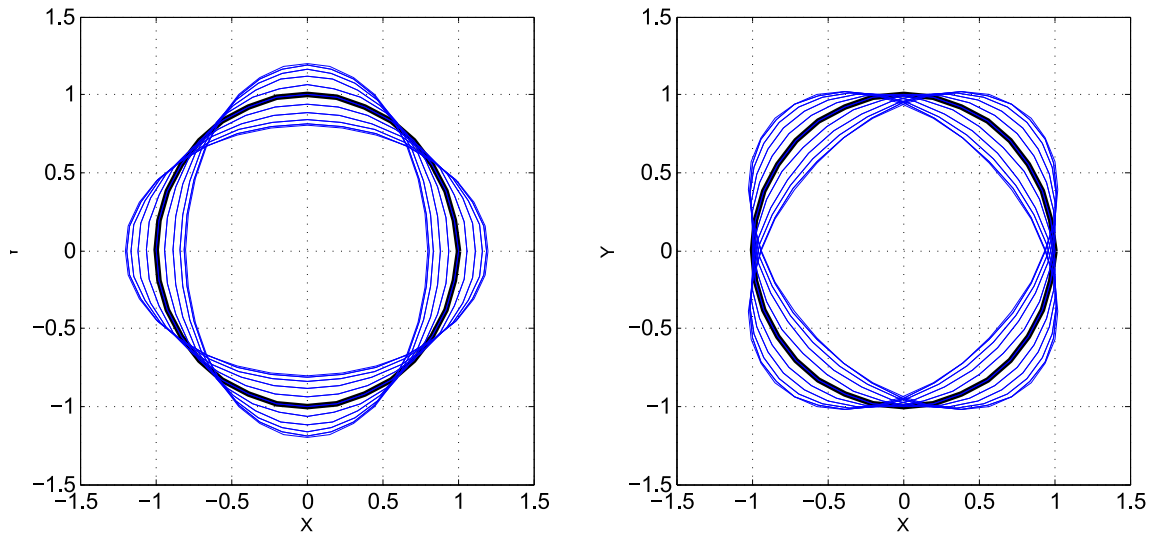
Figure A.4: How test particles move when GW passes through them. *left* shows + mode while *right* shows × mode

This picture can be understood as the very basic concept of gravitational wave detectors. By placing test masses along the x-axis and the y-axis and forming a Michelson interferometer, we can sense the displacement due to the gravitational wave. Since the strain level is so tiny, a lot of techniques are needed to make the gravitational wave observable.

Appendix B

Bode plots of some electronics in DARM control loop chain

Here are some Bode plots measured after S5. These are all analog parts in the DARM control loop as described in chapter 2. ASQ1, ASQ2, ASQ3, ASQ4 are names of different photodiodes and the legend in the plots are electronics for those. Similarly, UL, LL, UR, LR are upper left, lower left, upper right, and lower right respectively.
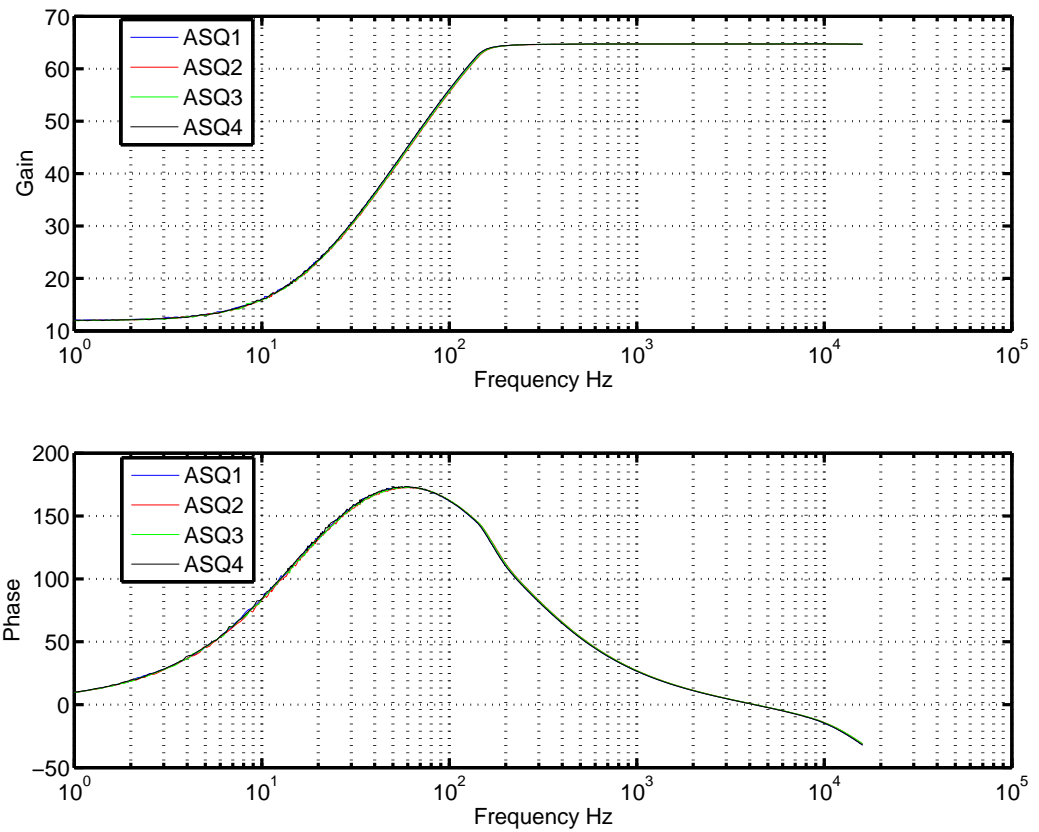
Figure B.1: Bode plot of the whitening filter in the sensing chain in the DARM loop. Un-whitening in digital domain is supposed to be the inverse of this to keep the overall gain constant.
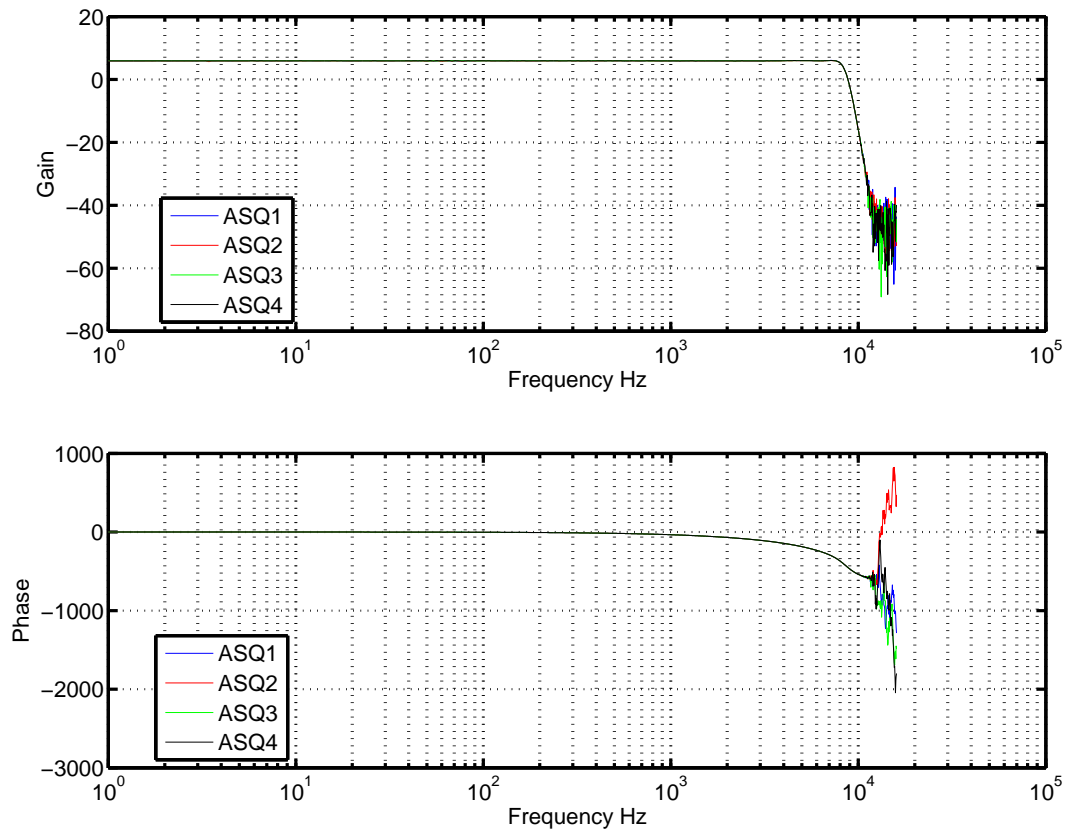
Figure B.2: Bode plot of the anti-aliasing filter in the sensing chain in the DARM loop. It cuts off beyond a frequency a half the sampling rate 16384 Hz.
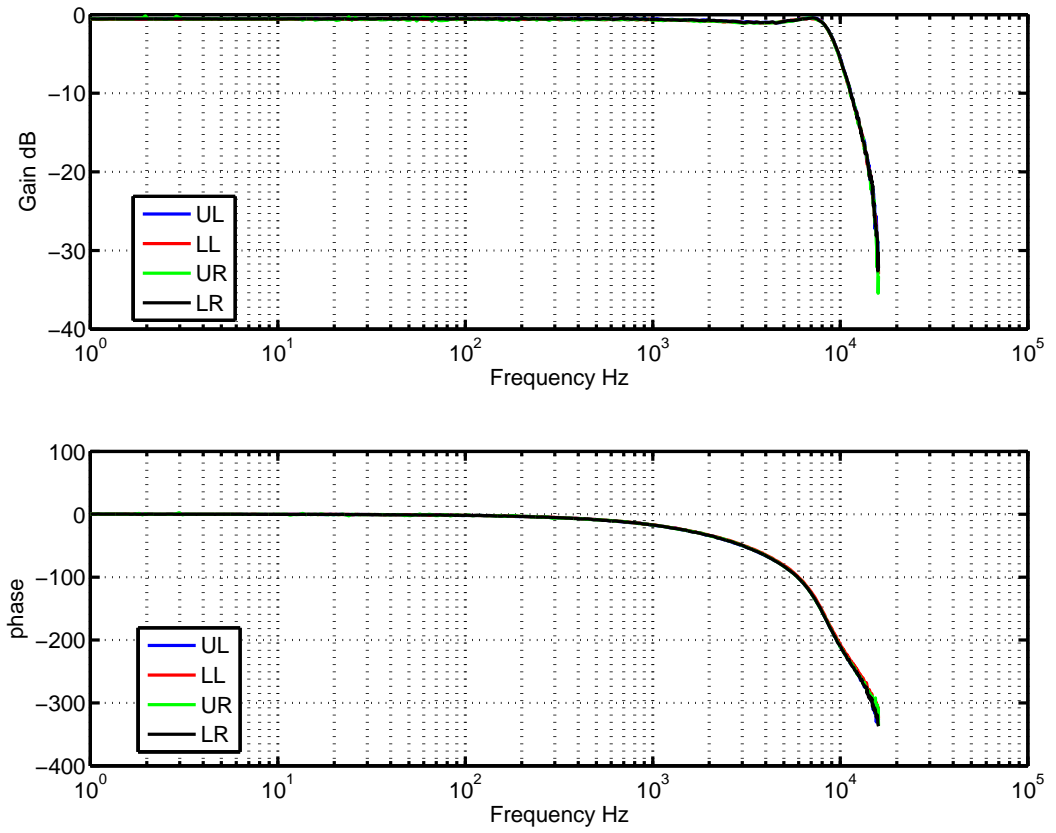
Figure B.3: Bode plot of the anti-imaging filter in the actuation chain in the DARM loop.
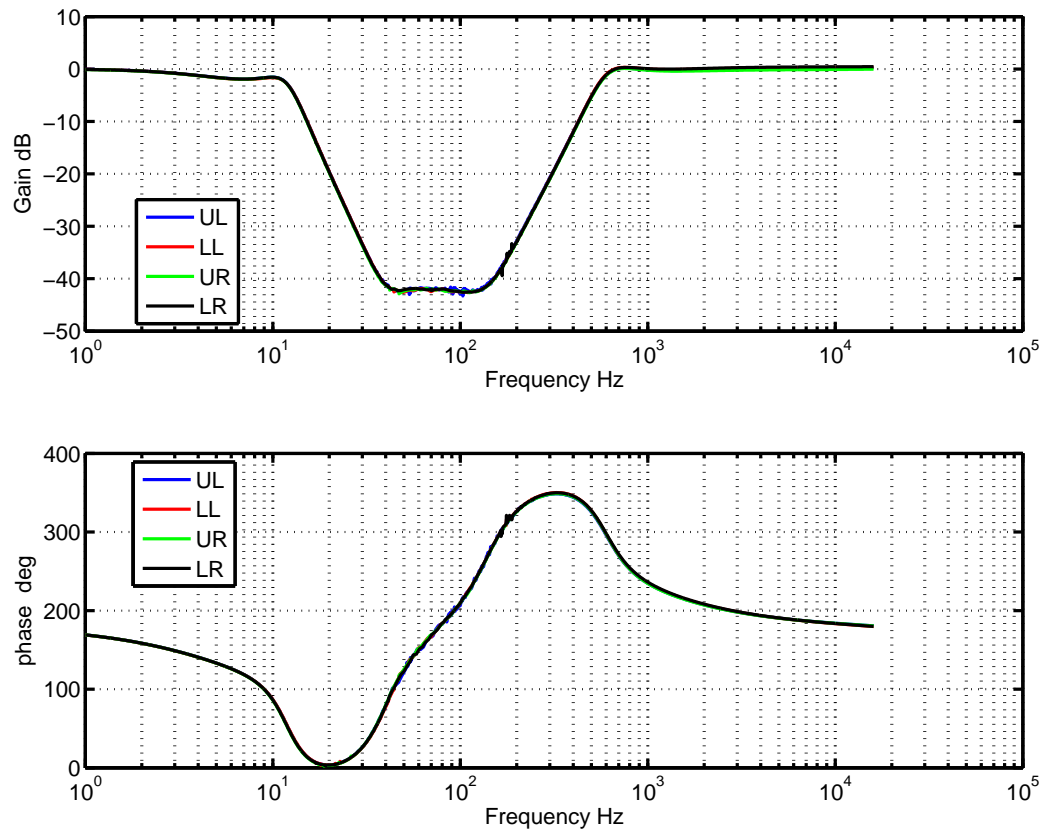
Figure B.4: Bode plot of the de-whitening filter in the actuation chain in the DARM loop.
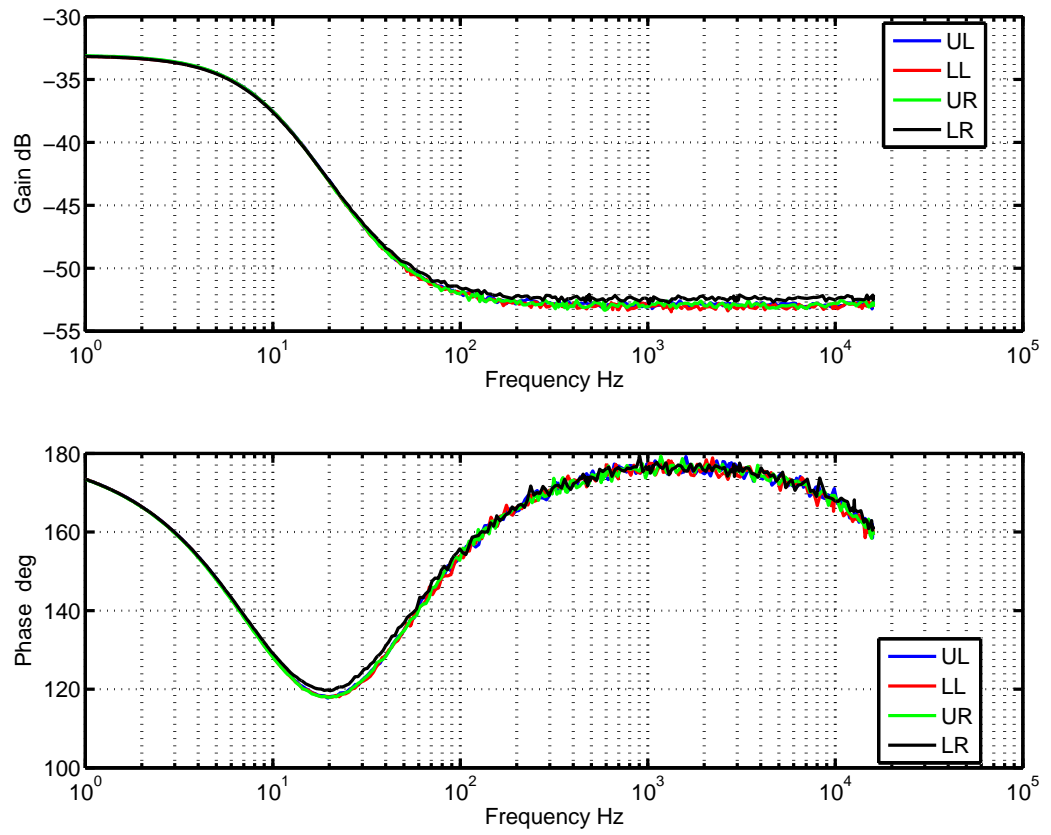
Figure B.5: Bode plot of the coil driver filter in the actuation chain in the DARM loop.

Appendix C

WFS error signals

Here are some plots of WFS error signals described in chapter 3. The x-axis is the Gouy phase shift from each port to a place where WFSs are located. The y-axis is the I-phase and the Q-phase error signal. The color scheme is the following: antisymmetric port - blue, reflected port - magenta, pickoff port - green, and reflected port (NR) - red.
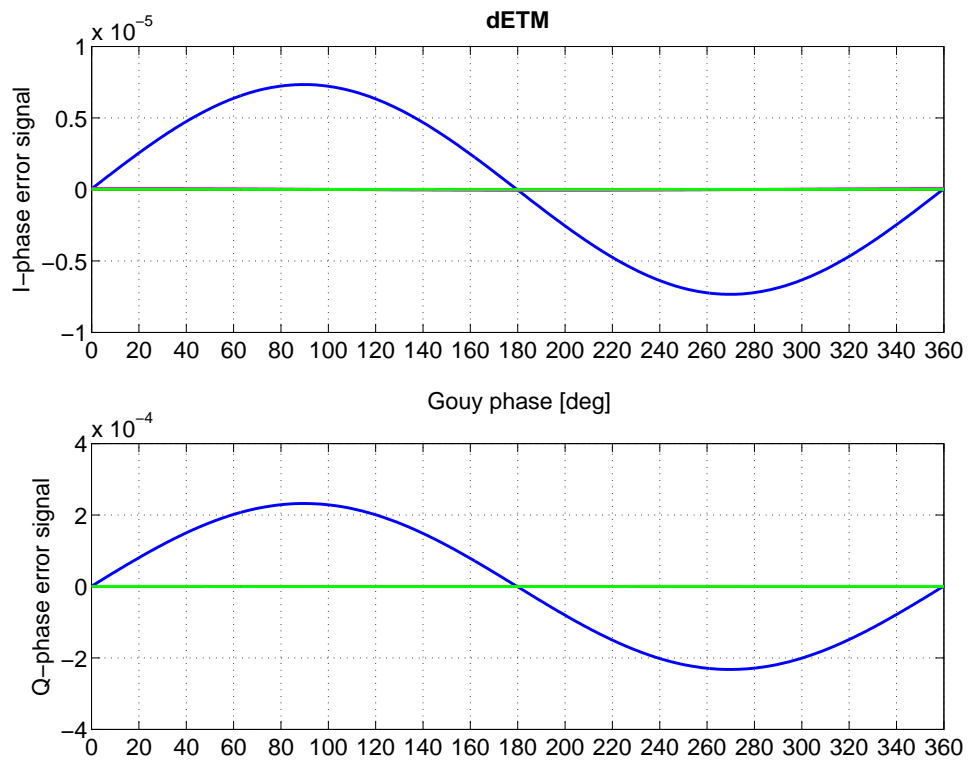
Figure C.1: Error signals to dETM
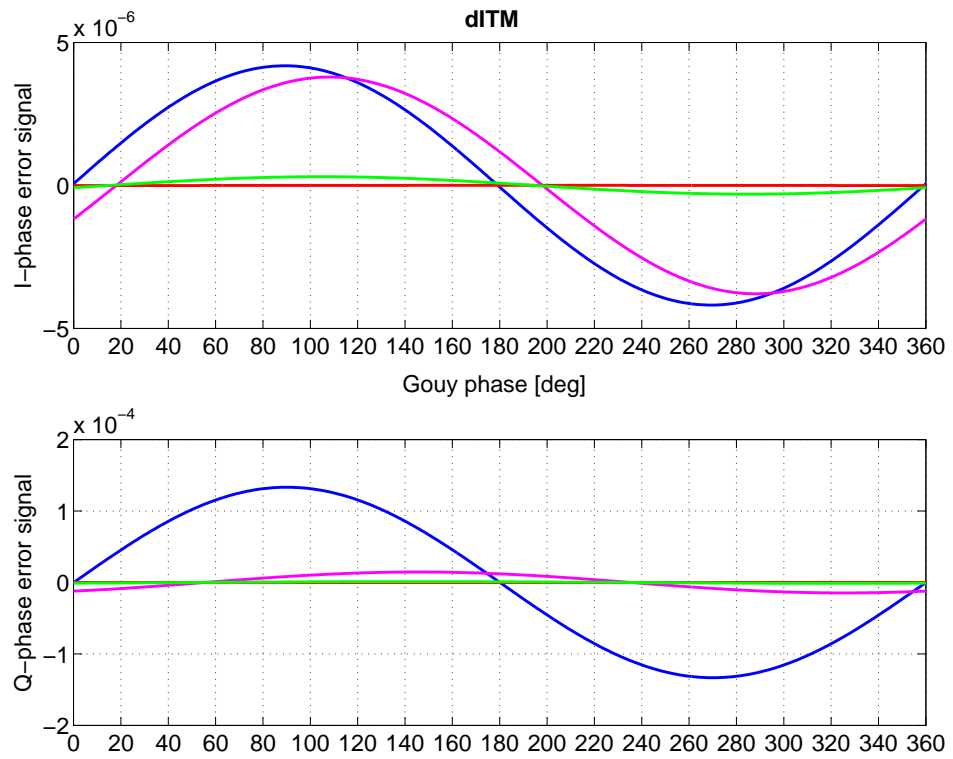
Figure C.2: Error signals to dITM
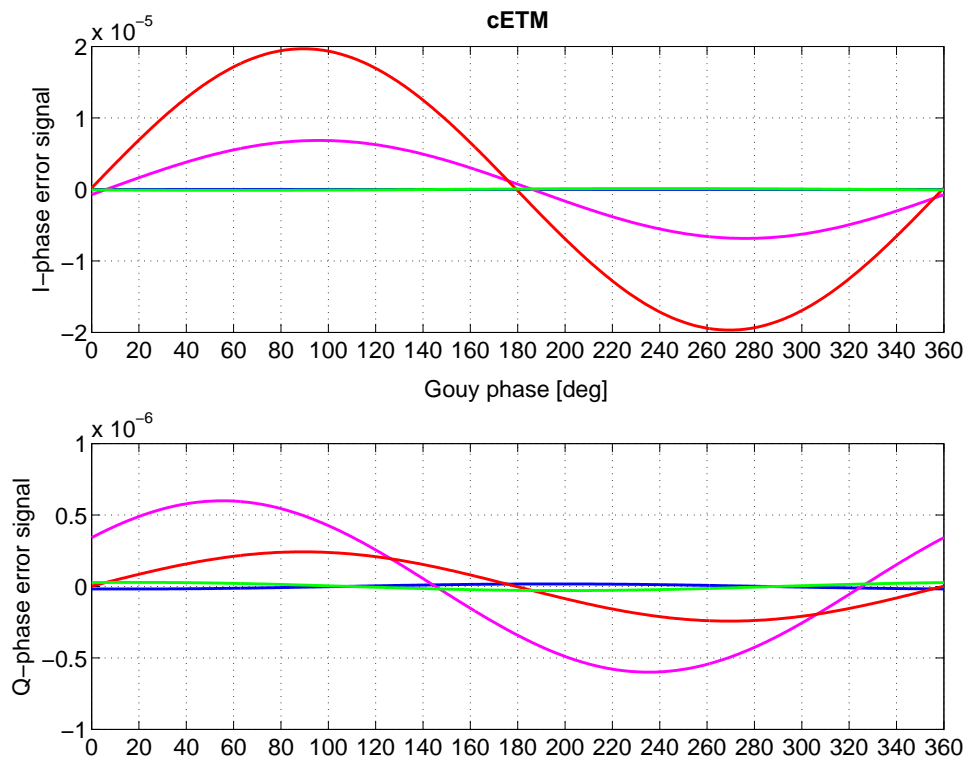
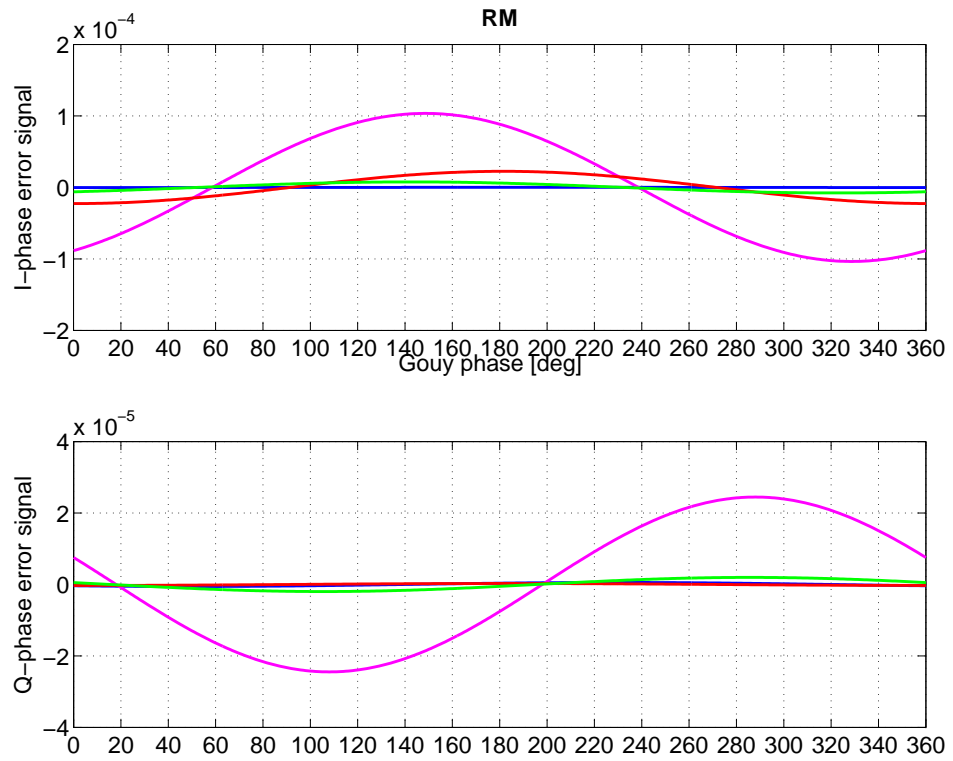Figure C.3: Error signals to cETM
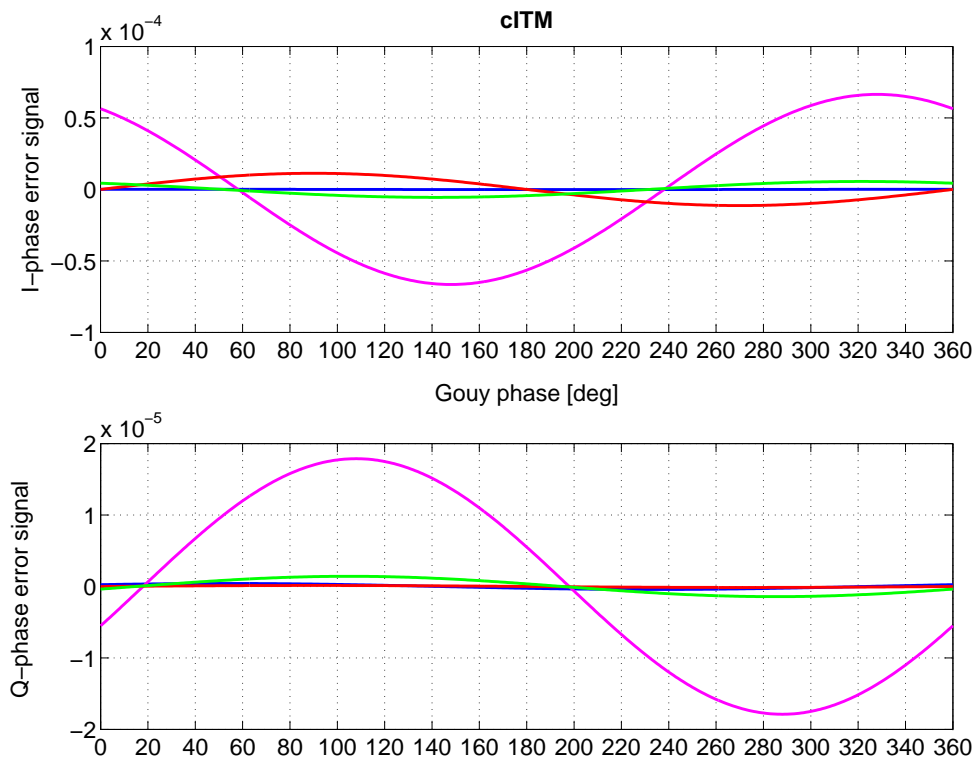
Figure C.4: Error signals to cITM

Figure C.5: Error signals to RM

Appendix D

Filters in the Angular Control Model

Here are filters built in the mathematical model described in chapter 4. All filters are exported from the real control system in LIGO when our measurement was done in Feburuary 2007. In order to fit a continuous model, all digital filters are replaced by the zpk model.
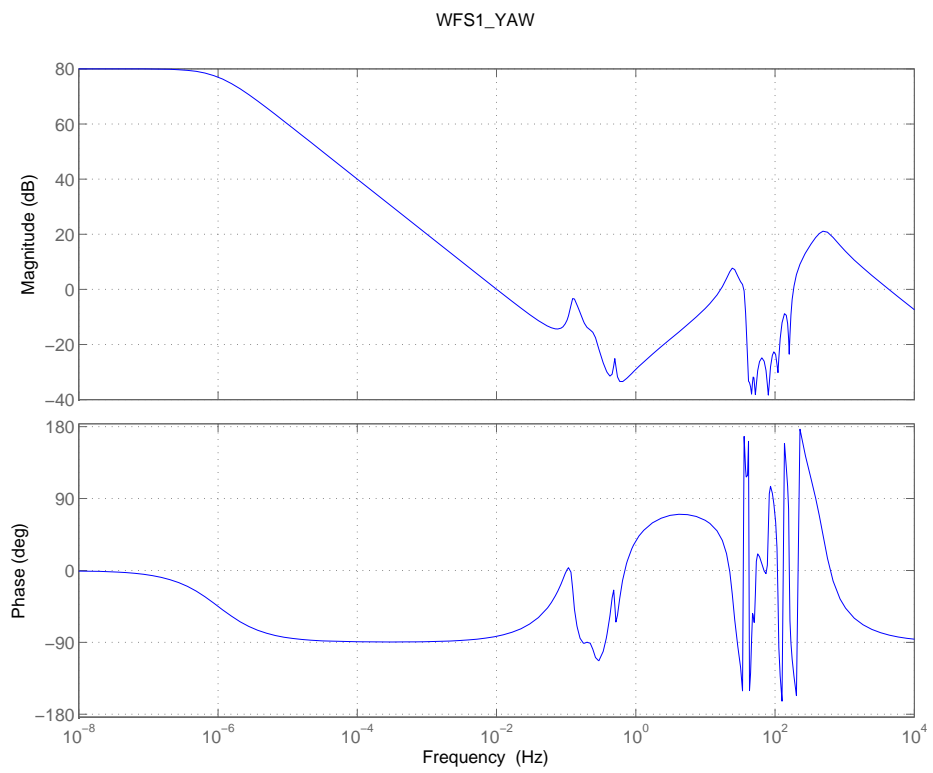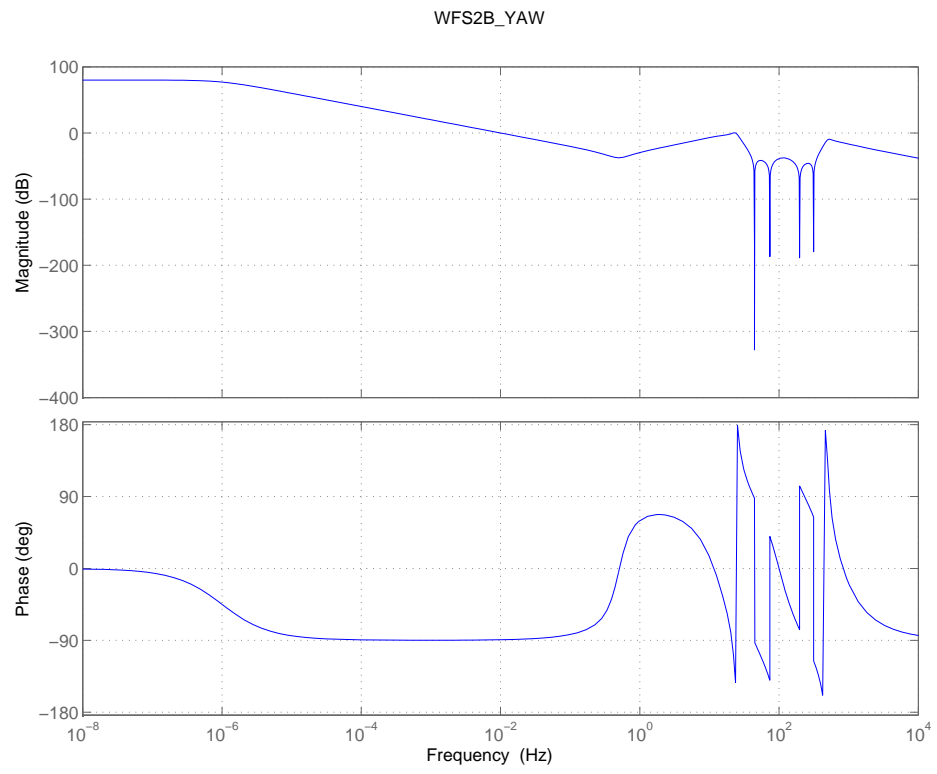
Figure D.1: WFS1_YAW filter
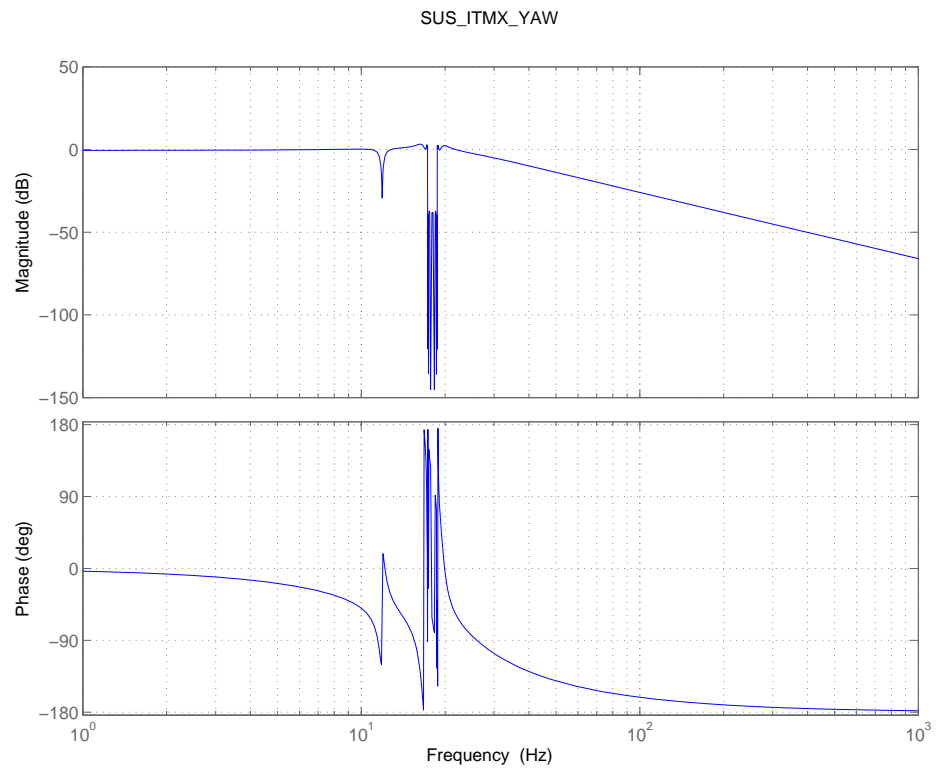
144

Figure D.2: WFS2B_YAW filter
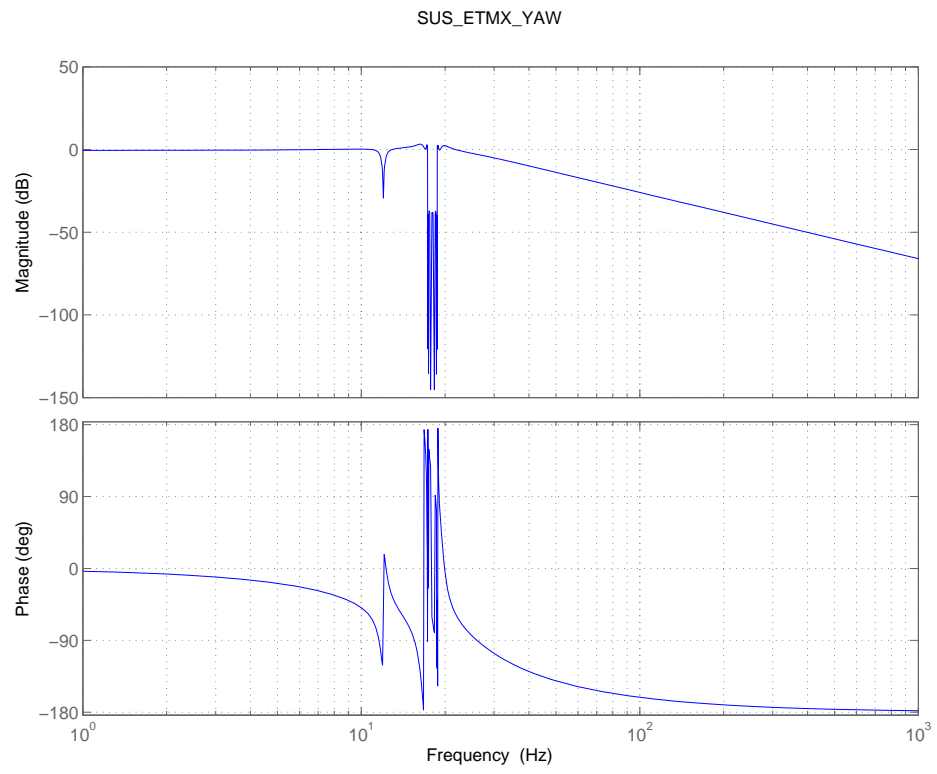
SUS_ITMX_YAW

Figure D.3: SUS_ITMX_YAW filter

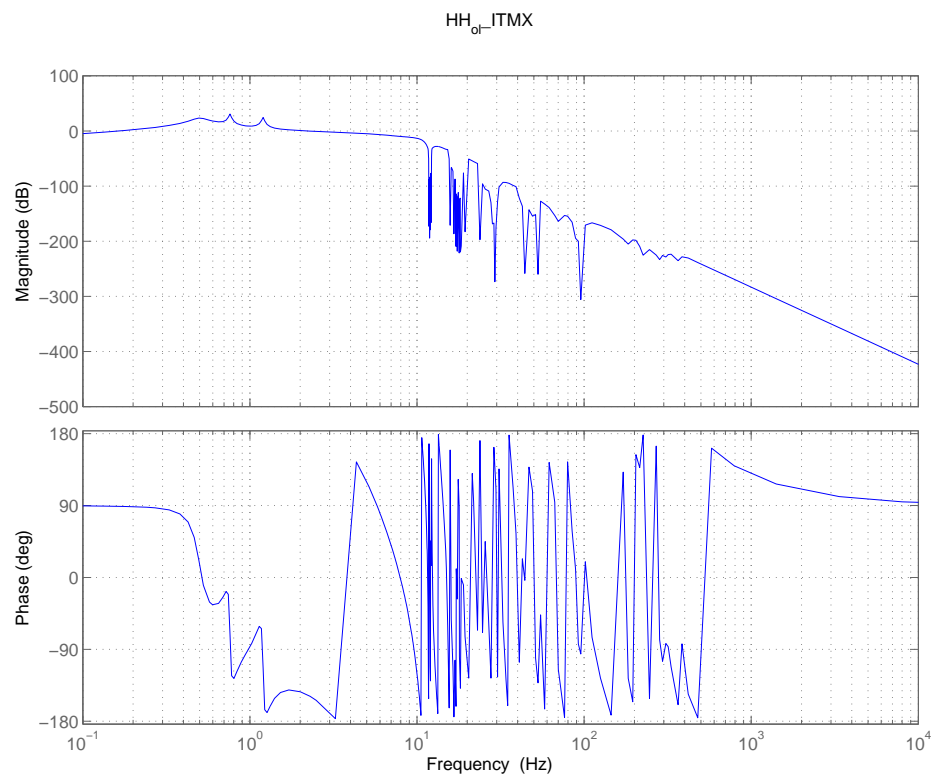Figure D.4: SUS_ETMX_YAW filter

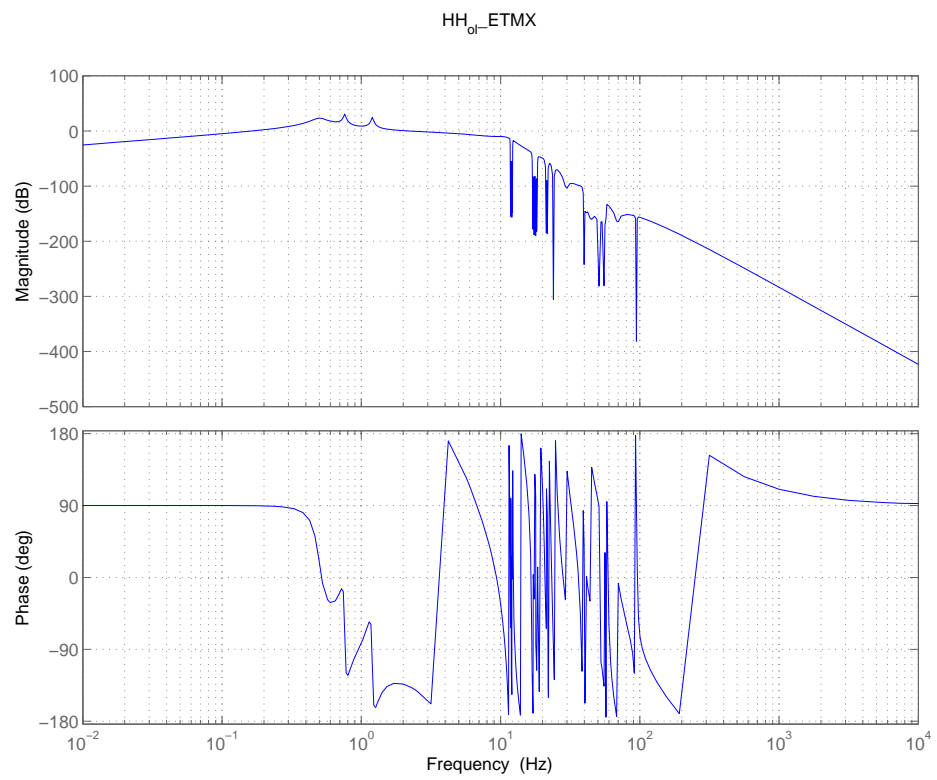Figure D.5: ITMX optical lever compensation filter
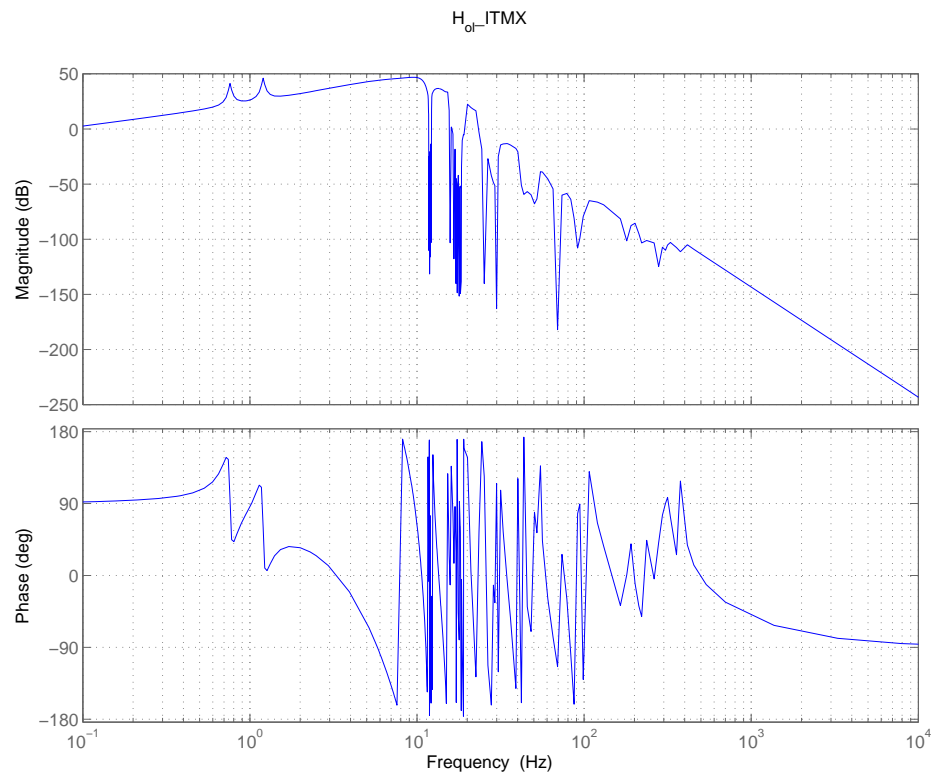
Figure D.6: ETMX optical lever compensation filter

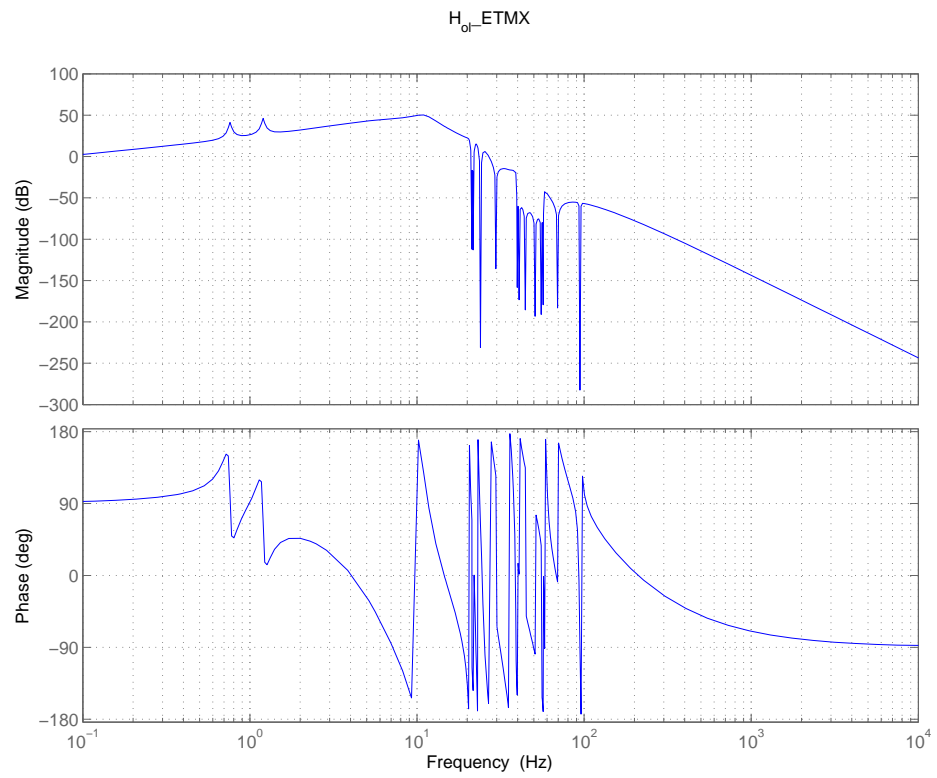Figure D.7: ITMX optical lever compensation filter

Figure D.8: ETMX optical lever compensation filter

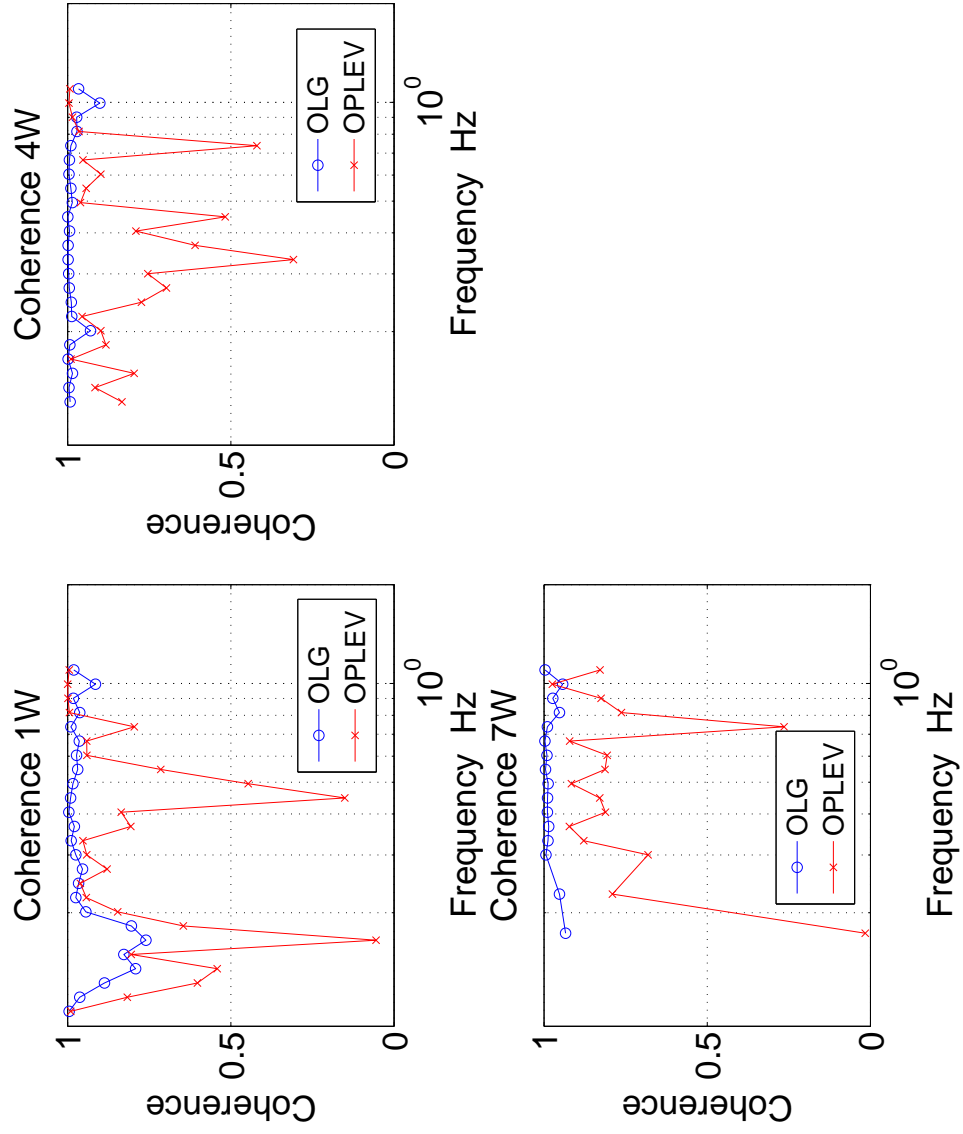# Appendix E

Coherence of the measurement described in 4.2

Figure E.1: Coherence of OPLEV and OLG in 4.2. The setting of the measurement: 40 cycles, 1 sec, ave = 3

Bibliography

[1] S. W. Hawking, G. F. R. Ellis, *The large scale structure of space-time*, Cambridge University Press (1973)

[2] Charles W. Misner, Kip S. Thorne, John Archibald Wheeler, *Gravitation*, W. H. Freedman and Company (1973)

[3] L. D. Landau, E. M. Lifshitz, *The Classical Theory of Fields*, Pergamon Press (1975)

[4] Steven Weinberg, *Gravitation and Cosmology*, John Wiley & Sons (1972)

[5] Hideo Kodama, *The Theory of Relativity*, Baifukan (1997)

[6] Edited by S. W. Hawking, W. I. Israel, *300 Years of Gravitation*, Cambridge Universiy Press (1987)

[7] Barry C. Barish, Rainer Weiss, *LIGO and the Detection of Gravitational Waves*, Physics Today, **52**, pp.44-50 (1999)

[8] Peter R. Saulson, *Fundamentals of Interferomeric Gravitational Wave Detectors*, World Scientific (1994)

[9] Samuel J Waldman (for the LIGO Scientific Collaboration), *Status of LIGO at the start of the fifth science run*, Class. Quantum Grav., **23**, S653-S660 (2006)

[10] Daniel Sigg (for the LIGO Scientific Collaboration), *Status of the LIGO Detectors*, LIGO-P070113-B-D (2007)

[11] Daniel Sigg, *Gravitational Waves*, LIGO-P980007-00-D (1998)

[12] Clifford M. Will, *Gravitational Radiation and the Validity of General Relativity*, Physics Today, **52**, pp.38-43 (1999)

[13] Clifford M. Will, *Theory and experiment in gravitational physics*, Cambridge University Press (1993)

[14] Clifford M. Will, *The Confrontation between General Relativity and Experiment*, Living Review in Relativity, http://relativity.livingreviews.org/Articles/lrr-2006-3/

[15] Peter Kurt Fritschel, *Techniques for Laser Interferometer Gravitational Wave Detectors*, PhD thesis Massachusetts Institute of Technology (1984)

[16] Rana Adhikari, *Sensitivity and Noise Analysis of 4km Laser Interferometric Gravitational Wave Anntene*, PhD thesis, Massachusetts Institute of Technology (2004)

[17] Stefan W. Ballmer, *LIGO interferometer operating at design sensitivity with application to gravitational radiometry*, PhD thesis, Massachusetts Institute of Technology (2006)

[18] Matthew Evans, *Lock Acquisition in Resonant Optical Interferometer*, PhD thesis, California Institute of Technology (2002)

[19] Keita KAWABE, *Development of a 3-meter Fabry-Perot-Michelson Interferometer for Gravitational Wave Detection*, PhD thesis, Massachusetts Institute of Technology (1998)

[20] Nergis Mavalvala, *Alignment Issues in Laser Interferometric Gravitational-Wave Detectors*, PhD thesis, Massachusetts Institute of Technology (1990)

[21] Marin W. Regehr, *Signal Extraction and Control for an Interferometric Gravitational Wave Detector*, PhD thesis, California Institute of Technology (1995)

[22] H. Kogelnik, T. Li, *Laser Beams and Resonators*, Appl. Opt. **5**, 1550-1567 (1966)

[23] A.E. Siegman, *Lasers*, University Science Books (1986)

[24] Daniel Sigg, *Strain Calibration in LIGO*, LIGO-T970101-B-D (1997, 2003)

[25] M. Rakhmanov, R. L. Savage, Jr, D. H. Reize, D. B. Tanner, *Dynamic Response of Light in Fabry-Perot Cavities*, arXiv:physics/0110061v1 (2001)

[26] Jean-Yves Vinet, Brian Meers, Catherine Nary Man, Allen Brillet, *Optimization of long-baseline optical interferometers for gravitational-wave detection*, Physical Review D. **38**, 433-447 (1988)

[27] J-Y Vinet, *Recycling interferometric antennas for periodic gravitational waves*, J. Physique. **47**, 639-643 (1986)

[28] M. W. Regehr, F. J. Raab, S. E. Whitcomb, *Demonstration of a power-recycled Michelson interferometer with Fabry-Perot arms by frontal modulation*, Optics Letters **20**, 1507-1509 (1995); LIGO-P50001-00-R

[29] Dana Z. Anderson, *Alignment of resonant optical cavities*, Appl. Opt. **23**, 2944-2949 (1984)

[30] Euan Morrison, Brian J. Meers, David I. Robertson, Henry Ward, *Automatic alignment of optical interferometers*, Appl. Opt. **33**, 5041-5049 (1994)

[31] Euan Morrison, Brian J. Meers, David I. Robertson, Henry Ward, *Experimental demonstration of an automatic alignment system for optical interferometers*, Appl. Opt. **33**, 5037-5040 (1994)

[32] John A. Sidles, Daniel Sigg, *Optical torques in suspended Fabry-Perot interferometers*, Phys. Letters A. **354**, 167-172 (2006)

[33] Daniel Sigg, *Angular Instabilities in High Power Fabry-Perot Cavities*, LIGO-T030120-00 (2003)

[34] P. Fritschel, G. González, N. Mavalvala, D. Shoemaker, D. Sigg, and M. Zucker, *Alignment of an interferometric gravitational wave detector*, Appl. Opt. **37**, 6734-6747 (1998)

[35] Yaron Hefetz, Nergis Mavalvala, Daniel Sigg, *Principles of calculating alignment signals in complex resonant optical interferometers*, **14**, pp.1597-1605, J. Opt. Soc. Am. B (1997)

[36] Daniel Sigg, Nargis Mavalvala, *Principles of calculating the dynamical response of misaligned complex resonant optical interferometers*, **17**, pp.1642-1649, J. Opt. Soc. Am. A (2000)

[37] Peter Fritschel, Rolf Bork, Gabriela González, Nergis Mavalvala, Dale Ouimette, Haisheng Rong, Daniel Sigg, Michael Zucker, *Readout and control of a power-recycled interferometric gravitational-wave antenna*, Appl. Opt. **40**, 4988-4998 (2001)

[38] Daniel Sigg, *Modal Model Update 1*, LIGO-T960113-00-D (1996)

[39] Daniel Sigg, *Modal Model Update 2*, LIGO-T960114-B-D (1996)

[40] Daniel Sigg, *Modal Model Update 3*, LIGO-T960115-A-D (1996)

[41] Daniel Sigg, *Modal Model Update 10*, LIGO-T980001-00-D (1998)

[42] ISC group, Daniel Sigg, ed, *Frequency Response of the LIGO Interferometer*, LIGO-T970084-00-D (1998)

[43] Doug Cook, *electric log at LHO on Feb 5, 2003* (2003)

[44] *script sense*

[45] *script conASC.m*

[46] *script calASC.m*

[47] Thomas Corbitt, David Ottaway, Edith Innerhofer, Jason Pelc, Nergis Maval-vala, *Measurement of radiation-pressure-induced optomechanical dynamics in a suspended Fabry-Perot cavity*, Physica Review A, **74**, 021802(R) (2006)

[48] Seiji Kawamura, Michael E. Zucker, *Mirror-orientation noise in a Fabry-Perot interferometer gravitational wave detector*, Applied Optics, **33**, No. 18 (1994)

[49] Nergis Mavalvala, *LIGO ASC Subsystem: Wavefront Sensing Telescope*, LIGO-T990130-02-D (1999)

[50] E. Hirose, K. Kawabe, *A study of radiation pressure effect on ASC in H1 and H2*, LIGO-G070118-00-Z (2007)

[51] A. Dietz, J. Garofoli, G. González, M. Landry, B. O'Reilly, M. Sung, *Calibration of the LIGO detectors for S4*, LIGO-T050262-01-D

[52] LSC-Virgo Collaboration, *Calibration of the LIGO Interferometers for the Fifth Science Run*, To be published
http://touro.ligola.caltech.edu/ irish/Work/Calibration/S5V3Review/S5V3Review.html

[53] Joseph Betzwieser, Philip Charlton, Chad Hanna, Eiichi Hirose, Brennan Hughey, Keita Kawabe, Vuk Mandic, Matt Pitkin, Xavier Siemens, Amber Stu-ver, Myungkee Sung, Sam Waldman, *S5 V3 h(t) review and validation*, LIGO-T080242-00-R (2008)

[54] Xavier Siemens, Bruce Allen, Julien Creighton, Martin Hewitson, Michael Landry, *Making h(t) for LIGO*, arXiv:gr-qc/0405070 (2004)

[55] Xavier Siemens, *Time domain calibration update: S5 and beyond*, LIGO-G080471-00-Z (2008)

[56] Eiichi Hirose, Xavier Siemens, *Validation of time-domain calibration*, LIGO-T070275-00-Z (2006)

[57] Personal communication with Dr. Xavier Siemens

[58] Richard G. Lynons, *Understanding Digital Signal Processing*, Prentice Hall (2004)

[59] Alan V. Oppenheim, Ronald W. Schafer, *Discrete-Time Signal Processing*, Prentice Hall (1999)

[60] MathWorks™, *Matlab®* and *Simulink®*

[61] Carlo Rovelli, *A note for DSR*, arXiv:0808.3505v1 (2008)

[62] T. Futamase, Bernard F. Schutz, *Gravitational radiation and the validity of the far-zone quadrupole formula in the Newtonian limit of general relativity*, Physical Review D, **32**, pp2557-2565 (1985)

[63] R. A. Hulse, Joseph H. Taylor, ApJ, **195**, L51, (1975)

[64] Joel M. Weisberg, Joseph H. Taylor, *Relativistic Binary Pulsar B1913+16: Thirty Years of Observations and Analysis*, arXiv:astro-ph/0407149v1, (2004)

[65] L. Barsotti, M. Evans *Modeling of Alignment Sensing and Control for Enhanced LIGO*, LIGO-T080186-01-I (2008)

[66] Eric Black *Notes on the Pound-Drever-Hall technique*, LIGO-T980045-00-D (1998)

VITA

NAME OF AUTHOR: Eiichi Hirose

PLACE OF BIRTH: Fukushima, Japan

DATE OF BIRTH: May 2, 1969

GRADUATE AND UNDERGRADUATE SCHOOLS ATTENDED:

Waseda University, Shinjuku, Tokyo, Japan

Texas A&M University, College Station, Texas, USA

DEGREES AWARDED:

Master of Science in Physics, 2005, Texas A&M University

Master of Engineering in Mechanical Engineering, 1995, Waseda University

Bachelor of Engineering in Mechanical Engineering, 1993, Waseda University

PROFESSIONAL EXPERIENCE:

Honda R&D Co. Ltd., 1995-2000, Engineer